

AN ABSTRACT OF THE THESIS OF

Justin Richard Finn for the degree of Master of Science in
Mechanical Engineering presented on June 19, 2009.

Title: A Multiscale Modeling Approach for Bubble-vortex
Interactions in Hydro-propulsion Systems

Abstract approved: _____

Sourabh V. Apte

Multiphase flow dynamics are important in many naval and turbomachinery applications, where bubble interaction with low pressure, vortical structures can lead to undesirable cavitation and acoustic effects. To better understand the underlying phenomena, a multiscale numerical framework is developed to simulate bubble laden flow in dynamic hydro-propulsion systems. Several subproblems in the pre-cavitation regime are identified and simulated, with a particular emphasis on bubble-vortex interactions. Two simulation techniques are used throughout. First, a Hybrid Lagrangian Eulerian (HLE) method, based on fictitious domain techniques is applied to both *forced* and *free* motion of arbitrarily shaped rigid bodies (i.e. propellers, hydrofoils & bubbles). This technique uses cartesian, body non-conformal grids to capture rigid body motion interactions with the fluid phase without grid regeneration. Next, a Discrete

Element Model (DEM) is applied to flows where the bubbly phase is not resolved by the grid (sub-grid scale). In this lower order model, DNS and Lagrangian bubble tracking are used. Various closures account for bubble forces, momentum transfer (2-way coupling), and bubble size effects (volumetric coupling). Several validation cases are presented to show the accuracy and flexibility of the methods. Two studies of bubble vortex interaction are presented in detail to show the applicability of both methods to bubble laden, propulsion generated turbulence. First, bubble interactions with a traveling vortex tube are studied using the DEM approach. Use of the volumetric coupling model results in distorted vortexes that are qualitatively similar to the distorted vortex rings observed by Sridhar & Katz [*JFM*, 1999], and good agreement is obtained with the experimental data for bubble settling location in the vortex core. Second, both models are compared in simulations of bubble entrainment in and subsequent distortion of a Gaussian vortex. The HLE approach, which fully resolves the bubble surface, is able to capture the transient distortion process, and gives insight into the mechanisms leading to this phenomena.

©Copyright by Justin Richard Finn
June 19, 2009
All Rights Reserved

A Multiscale Modeling Approach for Bubble-vortex Interactions in
Hydro-propulsion Systems

by

Justin Richard Finn

A THESIS

submitted to

Oregon State University

in partial fulfillment of
the requirements for the
degree of

Master of Science

Presented June 19, 2009
Commencement June 2010

Master of Science thesis of Justin Richard Finn presented on June 19, 2009.

APPROVED:

Major Professor, representing Mechanical Engineering

Head of the School of Mechanical, Industrial and Manufacturing Engineering

Dean of the Graduate School

I understand that my thesis will become part of the permanent collection of Oregon State University libraries. My signature below authorizes release of my thesis to any reader upon request.

Justin Richard Finn, Author

ACKNOWLEDGEMENTS

The author wishes to thank all those who have contributed to this work. Funding for this project was provided in part by the Office of Naval Research (ONR). The faculty and graduate students in the Thermal Fluid Sciences group at OSU have been great people to work with the last two years. My advisor, Dr. Sourabh Apte, has been a fantastic mentor, and I thank him for many patient hours helping me to complete this. Past and present members of the Computational Flow Physics Group; Ehsan Shams, Mathieu Martin, Stephen Snider, and more recently Andrew Cihonski and Daniel Peterson have provided many useful discussions and insights. Ehsan and Mathieu in particular have contributed significantly to my understanding of this study, to which I am very grateful. My family has always been very supportive of my endeavors, academic and otherwise, despite being 3,000 miles away. My girlfriend, Lillian, deserves great thanks for putting up with me (or a lack thereof) during the final phases of completion and for always keeping me level. Finally, to all my friends who I've shared mountain bike rides, pints, and laughs with, your contribution cannot be underestimated.

TABLE OF CONTENTS

	Page
1 Introduction	2
2 Literature review	7
2.1 Multiphase Flow Models	8
2.2 Bubble-Vortex Interactions	10
3 Mathematical Formulation	16
3.1 Discrete Element Model with Finite Size Effects	18
3.1.1 Variable Density Fluid Formulation	18
3.1.2 Bubble Dynamics	21
3.2 Fully Resolved HLE Scheme for Rigid Body Motion	25
4 Numerical Implementation	32
4.1 Variable Density Discrete Element Model	33
4.1.1 Gaussian Interpolation Kernel	34
4.1.2 Variable Storage and Discretization	35
4.2 Hybrid Eulerian Lagrangian (HLE) Method	36
4.2.1 Immersed Object Representation	36
4.2.2 Variable Storage & Discretization	38
5 Validation	40
5.1 Flow Past a Cylinder at a Range of Reynolds Numbers	43
5.1.1 Recirculation Length	43
5.1.2 Lift & Drag Coefficients	44
5.1.3 Strouhal Number of Lift Oscillations	47
5.1.4 Wake Statistics	48
5.2 Flow Over a Stationary NACA 0008 Hydrofoil at $Re_c = 2,000$. . .	52
5.3 Inline Oscillation of a Circular Cylinder	56
5.4 The Falling Sphere Problem	60
5.5 Rise of a Buoyant Sphere	63
5.5.1 Low Density Ratio	65
5.5.2 High density ratio	68

TABLE OF CONTENTS (Continued)

	<u>Page</u>
5.6 Three-Dimensional Falling "Blob"	74
6 Bubble-Vortex Interactions	83
6.1 Bubble Interactions With a Traveling Vortex Tube	85
6.1.1 Vortex Tube Generation	85
6.1.2 Bubble Injection	92
6.1.3 Results	93
6.2 Bubble Entrainment by a Gaussian Vortex	105
6.2.1 Problem Setup	105
6.2.2 Effects of DEM Lift Coefficient	108
6.2.3 Comparison of DEM and HLE Trajectories	109
6.2.4 Vortex Distortion	111
7 Conclusions and Outlook	118
Appendices	121
A Grids Used for Flow Over a Cylinder	122
B DEM Numerical Algorithm	125
C HLE Numerical Algorithm	130
D Interphase Interpolations	136
E Updating the Particle Position	139
Bibliography	141

LIST OF FIGURES

Figure	Page
1.1 Schematic of the traveling bubble/rigid body interaction problem. . .	4
2.1 A schematic of forces acting on bubbles entrained in a traveling vortex tube	14
3.1 Illustration of the fluid domain, Γ containing a subgrid scale dispersed phase.	19
3.2 Illustration of the fluid domain, Γ_F containing a resolved particle, Γ_P , with boundary \mathcal{B}	27
4.1 Schematic of DEM variable storage in time.	35
4.2 Schematic of material volumes for a circular object.	37
4.3 Schematic of the HLE variable storage in time and space	39
5.1 Streamlines of flow over a cylinder	44
5.2 Time evolution of computed lift and drag coefficients for flow over a cylinder	46
5.3 Vortex shedding behind the stationary cylinder	49
5.4 Vertical velocity profiles behind the cylinder at 5 positions downstream	51
5.5 Grid used for the hydrofoil case	53
5.6 Contours of vorticity around the hydrofoil	54
5.7 Evolution of lift and drag coefficients for the hydrofoil	55
5.8 Computational grid used for the oscillating cylinder case	58
5.9 Vorticity contours around the oscillating cylinder	59
5.10 Velocity profiles in the wake of the oscillating cylinder	59
5.11 Fall velocity & height for the falling sphere problem	61
5.12 Grids used for the low density ratio buoyant sphere simulations . .	65
5.13 Reynolds number evolution of the low density ratio buoyant sphere	67

LIST OF FIGURES (Continued)

Figure	Page
5.14 Fluid velocity induced by the rising sphere	68
5.15 Wake velocity profiles behind the rising, buoyant sphere	69
5.16 High density ratio model results comparison for the buoyant sphere problem	72
5.17 Cross section of the sphere shape generated using the LDR and HDR grid resolutions in the FRS approach.	73
5.18 Comparison of falling blob speed as predicted by all models	78
5.19 Instantaneous falling blob cross sections	80
5.20 Evolution of the bag vortex ring generated by the falling blob	81
5.21 Comparison of the present results with the experimental results of Mitts et al. [1] for the bag vortex ring sub-regime of the multi-mode breakup category.	82
6.1 Evolution of the traveling vortex tube	87
6.2 Inlet velocity profile used to generate the traveling vortex tube	87
6.3 Vortex core trajectory. Tracked by following center of vorticity	90
6.4 Cylindrical coordinate mapping of the vortex core	91
6.5 Evolution of the instantaneous radial vorticity distribution in the core of the traveling vortex tube	92
6.6 Release points and trajectories of the eight bubbles in the moving, cylindrical reference frame.	93
6.7 Effects of bubble size on entrainment in the traveling vortex tube . . .	96
6.8 Bubble trajectory shown in the moving, cylindrical reference frame . . .	97
6.9 Comparison of the non-dimensional bubble settling location to the experimental data of Sridhar & Katz	99
6.10 Vortex tube distortion due to the presence of the bubbles: Vorticity countours	102

LIST OF FIGURES (Continued)

Figure	Page
6.11 Vortex tube distortion due to the presence of the bubbles: Radial vorticity distribution	103
6.12 Vortex tube distortion due to the presence of the bubbles: Angular vorticity distribution	104
6.13 Comparison of vorticity in the traveling vortex tube and the stationary Gaussian vortex	107
6.14 Comparison of radial vorticity distribution in the traveling vortex tube and the stationary Gaussian vortex	107
6.15 Effect of lift coefficient on entrainment trajectory in the Gaussian vortex	109
6.16 Comparison of the DEM and HLE bubble entrainment trajectories in the Gaussian vortex	112
6.17 Entrainment of a single bubble into the Gaussian vortex and the effects on the fluid phase	114
6.18 Isosurfaces of vorticity magnitude around a single 1200 micron bubble being entrained. Magnitude of isosurface is approximately twice the initial value of ω_{max}	115
6.19 Vortex core after 2.5 seconds with a single 1,200 μm bubble at its final settling location. Contours of enstrophy range from 10 to 130 .	116
6.20 Periodic shedding of vorticity into the wake of the settled bubble . .	117

LIST OF TABLES

<u>Table</u>	<u>Page</u>
5.1 Comparison of C_d with previous studies	47
5.2 Comparison of computed Strouhal number with previous studies . .	48
5.3 Computational parameters used in the hydrofoil case	53
5.4 Comparison of steady state drag and lift coefficients with other 2D computational results	55
5.5 Computational parameters used in the oscillating cylinder case . . .	57
5.6 Parameters for the sedimenting sphere test problem.	60
5.7 Computational parameters used in the buoyant sphere case	64
5.8 Computational grids for the buoyant sphere case	64
5.9 Drag model restrictions	71
5.10 Parameters used for the setup of the three dimensional falling "blob"	77
5.11 Comparison of the 3 present DEM models and the model used by Walther & Koumoutsakos in the falling blob case	78
6.1 Values of constants used for the inlet velocity profile	86
6.2 Computational parameters used in the vortex tube case	88
6.3 Computed settling location and observed vortex distortion for each case (volumetric coupling results)	94
6.4 Computational parameters used in the setup of the Gaussian vortex case	106
6.5 Computational domain and grids used for the Gaussian vortex case	106
6.6 Comparison of DEM and HLE settling time and location in the Gaussian vortex	110

LIST OF APPENDIX FIGURES

<u>Figure</u>	<u>Page</u>
A.1 Body fitted grid used for all simulations $Re_d = 40, 100, 300, 1,000$. The inset shows the region near the cylinder surface.	123
A.2 Medium grid used in the HLE simulations. Close up of cylinder surface	124

DEDICATION

Dont ever jump the shark

A Multiscale Modeling Approach for Bubble-vortex
Interactions in Hydro-propulsion Systems

Chapter 1 – Introduction

Multiphase interactions with moving propulsion systems are encountered frequently in naval and industrial applications among others. Modeling approaches for these types of flows, must be diverse in nature, and capable of handling multiple length, and time scales. Consider the following motivating problem illustrated schematically in figure 1.1: A bubble nuclei (red) travels through water upstream of a lifting surface (i.e. naval propeller, turbomachinery, or water-craft), illustrated by a hydrofoil in the schematic, undergoing forced rigid body translation (U) and rotation (Ω). The main scales of motion upstream are large, and can be accurately simulated on relatively coarse grids with mean spacing larger than the bubble size. As the bubble passes over the suction side of the body, it encounters a low pressure region, and a dynamic leading edge vortex. For even modest Reynolds numbers, wide separation of turbulent length scales dictates much finer grid resolution near the body in motion. The local turbulent flow structures may be altered by the presence of the bubble, and depending on conditions, the nuclei may begin to cavitate. This travelling bubble cavitation may eventually lead to attached sheet or periodic cloud cavitation, a generally undesirable operating effect because of resulting equipment damage, acoustic effects, and loss of hydrodynamic efficiency. Once passing into the wake, the bubble encounters more low pressure regions and becomes entrained into the vortex cores, where it may again alter the flow structure significantly. The nature of bubble-vortex interactions leading to vortex distortion, and the subsequent effects on cavitation inception are not well understood at the moment.

It is hard to identify one single crux associated with modeling the illustrated

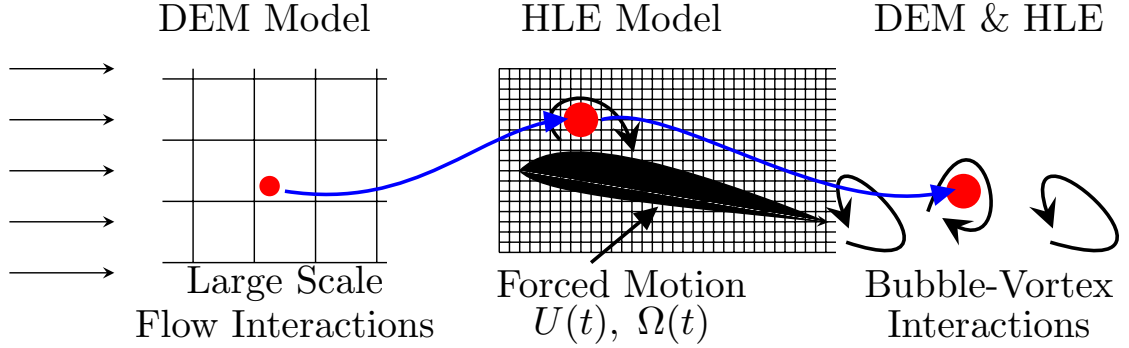


Figure 1.1: Schematic of the traveling bubble/rigid body interaction problem.

problem . Current computational restrictions limit the use of *complete* models, and various levels of approximation must be introduced. In regions where the scales of fluid motion are large (upstream), coarse grids are sufficient to solve the problem numerically. To model bubble laden flow in these regions, Discrete Element Methods (DEM) may be used where the bubbles are subgrid in size. Their surface shape is not explicitly represented, and the no-slip condition is not directly enforced. Motion of individual bubbles is governed by Newton's second law, and expressions for various forces acting on the bubbles are used to advance their position in time. Interaction with the flow field occurs through an interphase force term in the momentum equations. In addition, in many multiphase regimes, it is important to account for the finite size of the dispersed phase [2] [3] [4] [5]. This can be accomplished by introducing variable density forms of the governing equations for the fluid phase. The effects of this *volumetric coupling* effect are examined in detail using the DEM approach in this thesis.

To model the motion of the moving body, one approach is to use adaptive, body fitted grids which are regenerated at each time step. This becomes computa-

tionally expensive for larger domains on the scales of engineering interest. Another approach is to use Immersed Boundary Methods (IBM) [6] or Fictitious Domain Techniques [7], where body non-conformal, cartesian grids are employed, and the surface of the moving body is imposed on the fluid domain by placing appropriate constraints on the governing equations. The fictitious domain method used in this thesis uses a Hybrid Lagrangian-Eulerian (HLE) approach, where Lagrangian marker particles are used to resolve the forced motion of the submerged body [8].

One advantage of the Fictitious Domain, HLE technique is that the extension to freely moving rigid bodies is possible with little added computational cost. Thus, the technique can be used to model the dispersed, bubbly phase in locations where grid resolution permits and deformation is small. In this way, the effects of the bubbles on the flow are computed directly without mathematical approximation. This becomes very useful in regions near the moving objects and in turbulent wakes, where the presence of a bubbly phase can significantly alter the flow structure. This work focuses on modeling the bubble-flow interactions before the point of significant bubble growth or deformation. For freely moving bubbles, the rigid, spherical assumption is valid for small Weber numbers where surface tension dominates. Treatment of resolved, deforming bubbles requires expensive front tracking methods [9], not yet practical for large geometries. In a DEM type model, the Rayleigh-Plesset equation for bubble growth may be solved and coupled to the bubble equation of motion to account for cavitation [10]. Bubble deformation can be treated implicitly through proper drag correlations [11].

Both the DEM and HLE approaches are useful in studying the highly dynamic

bubble-vortex interactions caused by hydro propulsion. As mentioned, the two methods are quite different in their treatment of the bubbly phase. When combined with experimental data, the HLE approach can offer excellent insight into the two phase interactions. When used in tandem with the DEM approach, the HLE method can be used as a tool to develop new, lower order models for use in the DEM type formulation.

The goal of this thesis is to develop a numerical framework capable of simulating all aspects of this multiscale problem, with an eye towards eventual integration and full simulation. The work is organized in the following manner. First, in chapter 2, a review of present modeling strategies and experimental work relating to this problem will be presented. Next, in chapter 3, the mathematical formulation of the DEM and HLE approaches will be developed, and the details of the numerical implementation will be given in chapter 4. In chapter 5, several validation studies will be presented to show the accuracy of the present methods, and their applicability to the problem of interest. Finally, in chapter 6, two studies of bubble-vortex interaction will be presented. In the first study, results of bubble interaction with a traveling vortex tube will be compared, with good agreement, to the experimental results of Sridhar & Katz [12]. Second, the results of the HLE and DEM models will be compared directly in the study of bubble entrainment by a Gaussian vortex, similar to the experiments and computations of Oweis et al. [13], and the mechanisms of bubble induced vortex distortion will be examined.

Chapter 2 – Literature review

This section presents an overview of present models used for multiphase flow as well as recent work in the area of coupled, two phase flow. An emphasis is placed on experimental and numerical studies of bubble-vortex interactions. For a broad picture of current modeling strategies in this area, the reader is referred to the reviews by Van der Hoef et al. [14] and Crowe [15].

2.1 Multiphase Flow Models

Current multiphase flow simulation techniques can be broadly classified based on the treatment of the dispersed phase. The simplest approach is a single fluid, or mixture model. Here, a single fluid phase is assumed, and the equations of fluid motion are solved along with a transport equation for dispersed phase volume fraction, α_g . The local fluid density is then modified through the mixture equation [16]:

$$\rho = \Theta_p \rho_p + (1 - \Theta_p) \rho_f \quad (2.1)$$

Where Θ_p is the volume fraction of the dispersed bubbly or particulate phase. Because the same set of equations are solved for both phases, momentum exchange occurs as a result. Single fluid, transport equation models are often used in cavitation modeling, where equations for vapor volume fraction are solved [17].

In an Eulerian-Eulerian or two-fluid model, both phases are treated as a continuum with unique fluid properties. The motion of each phase is governed by a unique set of Navier Stokes equations. Because the idea of individual particles is not supported, closure models must be used for interphase momentum trans-

fer. Successful simulations have been realized with these types of models in areas such as bubbly flows, cavitating flow over bluff bodies, and mixing to name a few [18] [19] [4]. Although Eulerian-Eulerian models do not capture bubble-bubble interactions or individual bubble effects on the fluid directly, their ability to predict large scale flow features at relatively low computational cost is promising for engineering and industrial scale applications.

The shortcomings associated with the Eulerian-Eulerian model are tackled most often using a Eulerian-Lagrangian framework, wherein the dispersed phase is treated as Lagrangian particles and each member is tracked individually. The dispersed phase may be modeled either as point particles or as resolved bodies. Discrete Element Models (DEM) and Discrete Bubble Models use the point particle approach, where the dispersed phase is typically assumed to be spherical and subgrid in size [11] [20] [2]. A Lagrangian equation of motion based on Newton's second law and various forces is solved for each bubble or particle. This equation of motion was derived by Maxey & Riley [21] for a rigid sphere and modifications may be made depending on the multiphase characteristics. Interphase momentum transfer (2-way coupling) is typically accounted for by a source term in the fluid momentum equation. In addition, it is frequently important to account for the finite size of the particles (volumetric coupling) [2] [5] [3] [4]. This can be done by introducing the variable density forms of the fluid phase continuity and momentum equations, as is done in the DEM formulation used in this work.

Although, the flow is affected by the presence of point particles, the no-slip condition at the dispersed phase surface is not directly enforced in a DEM or DBM

type model. To resolve the arbitrary shape of larger or deformable bubbles, it is necessary to use fully resolved simulations (FRS) and solve for the flow around each individual body. In contrast to the point particle approach where the bodies must be subgrid in size, fully resolved techniques require significant grid refinement in the region of surface motion. Most recently, immersed boundary methods [6], and fictitious domain techniques [7] [8] have received considerable attention for their ability to resolve the dispersed phase surface on uniform cartesian grids without grid regeneration. These resolved models can be extended to handle forced rigid body motion with no additional complexity. This feature is taken advantage of in the Fictitious Domain, HLE approach used in this work. Recently, many groups have extended these methods to study flows around complex moving bodies which would have previously required adaptive grid regeneration. Mittal et al. [22] used Immersed Boundary Methods to study various aspects of biological propulsion, while Cristallo and Verzicco [23] simulated flow through a mechanical heart valve and an internal combustion engine piston.

2.2 Bubble-Vortex Interactions

Bubble entrainment and interaction with vortical structures is an excellent problem to study for the development of models dealing with bubble motion, cavitation, and interphase dynamics. Vortical entrainment of bubbles has been studied by several groups [13] [24] [4] [12]. Experimental techniques, can be used to arrive at empirical relationships and closure models for the forces acting on bubbles in non-

uniform flow. This was done by Sridhar & Katz [12] and Van Nierop et al. [24], with particular emphasis placed on the determination of the bubble lift coefficient. Fully resolved techniques can also be useful for developing lower order (DBM & DEM) models. Oweis et al. [13] used front tracking methods developed by Tryggvason et al. [9] to solve the flow field around deforming and cavitating bubbles during entrainment by a Gaussian vortex. They compared bubble capture time predicted by a passive point particle method with the fully resolved DNS results as well as experimental data under similar conditions. They found their point particle method was able to accurately capture the trajectory of bubble entrainment, up to the point of cavitation and volume growth in the vortex core.

Bubble interactions with vortex rings were investigated by Sridhar and Katz (S&K) [12] and [25]. In [25], they used PIV data to measure the forces acting on microbubbles, $500\mu m$ to $800\mu m$ in diameter, which were entrained in a traveling vortex ring. In [12], they observed the effects of similarly sized bubbles on the structure of the vortex rings. An electronically controlled circular piston is used to pulse a jet into an initially stationary tank of water. A single vortex ring is created, and advected downstream with some initial circulation, Γ_o , where a bubble generator injects rising bubbles into its path. The bubbles are entrained into the vortex core, and eventually reach a settling location, where the forces acting on them are in equilibrium. High speed imaging and PIV data were used to obtain both the bubble trajectories and the fluid velocity field, from which lift and drag forces were measured indirectly.

Their experimental results show that for a small number of entrained bubbles,

less than 1 millimeter in diameter, significant distortion of the ring structure is possible under certain conditions. This distortion, which results from the two-way interactions of the bubbles with the flow, was characterized by the core vorticity distribution. In significantly distorted vortices, the presence of the bubbles resulted in a fragmented core, with multiple regions of higher vorticity. Further, the core was shifted upwards, in the direction of the buoyancy force acting on the entrained bubbles.

They supplied a rigorous analytic explanation of the observed distortion, based on the bubble equation of motion. A short summary of their arguments is included here. In the Lagrangian reference frame, the equation of motion for a rigid sphere in non-uniform flow derived by Maxey and Riley [21] can be rearranged to obtain

$$\frac{\partial \mathbf{U}_b}{\partial t} = -2\mathbf{g} + 3 \left\{ \frac{D\mathbf{U}}{dt} + (\mathbf{U} \cdot \nabla)\mathbf{U} \right\} + \frac{3}{4a}C_d|\mathbf{U}_{rel}|\mathbf{U}_{rel} + \frac{3}{4a}C_l|\mathbf{U}_{rel}|^2\mathbf{U}_{rel} \frac{\mathbf{U}_{rel} \times \boldsymbol{\omega}}{|\mathbf{U}_{rel}||\boldsymbol{\omega}|} \quad (2.2)$$

where, \mathbf{g} is the gravitational acceleration, \mathbf{U}_b is the bubble velocity, \mathbf{U} is the local fluid velocity, \mathbf{U}_{rel} is the bubble slip velocity, $\boldsymbol{\omega}$ is the local vorticity, C_l is the lift coefficient, C_d is the drag coefficient, and the added mass coefficient is assumed to be 0.5. In equation 2.2, the bubble acceleration on the left hand side is balanced by the body force, the added mass force, the pressure force, the drag force and the lift force. Figure 2.1 shows the manner in which these forces act on a bubble settled in the core of a traveling vortex. When the bubble comes to rest relative to the core center (X_c, Y_c) , the bubble acceleration is zero, and it translates rectilinearly with the vortex core. The vortex core travels in the x direction with velocity V_c .

The clockwise circulation, Γ , is the integral of the instantaneous vorticity within the core. The core radius, is denoted as R , and the bubble settling radius is r . At this point, the components of lift, drag, added-mass, pressure, and buoyancy forces are in balance. For a vortex core translating in the positive x direction as shown, the settling location is in the upper right corner of the core where the fluid velocity is turning downward. This was also observed by Mazzitelli & Lohse [26] in a study of developed turbulence and by Climent [27] in Taylor-Couette flow. Assuming that gravitational acceleration acts in the positive Y direction, the body force is always aligned upward. The added-mass force force acts in the direction of negative pressure gradient. Neglecting outside disturbances and assuming a circular core, this is always toward the vortex center center. The drag force acts in the direction of the slip velocity vector which, for a stationary bubble in a uniformly distributed vorticity field, is perpendicular to the settling location vector, r . The lift force acts perpendicular to the vorticity and slip velocity vectors, outward from the center. Mazzitelli & Lohse [26] showed that it is primarily the lift force which is responsible for bubble accumulation in the downward velocity side of vortices. This preferential accumulation has been observed in many studies and is responsible for bubble clustering, and modulation of turbulence [28], [26] , [27].

With proper non-dimensionalization of equation 2.2, Sridhar & Katz arrived at the following form of the bubble motion equation

$$\bar{g} = \frac{3}{8\pi^2} \bar{r} \left\{ \frac{D\bar{\mathbf{U}}}{d\bar{t}} \right\} + \frac{3}{32\pi^2} C_d \frac{\bar{r}^2}{\bar{a}} |\bar{\mathbf{U}}_{rel}| \bar{\mathbf{U}}_{rel} + \frac{3}{32\pi^2} C_l \frac{\bar{r}^2}{\bar{a}} |\bar{\mathbf{U}}_{rel}|^2 \frac{\bar{\mathbf{U}}_{rel} \times \bar{\boldsymbol{\omega}}}{|\bar{\mathbf{U}}_{rel}| |\bar{\boldsymbol{\omega}}|} \quad (2.3)$$

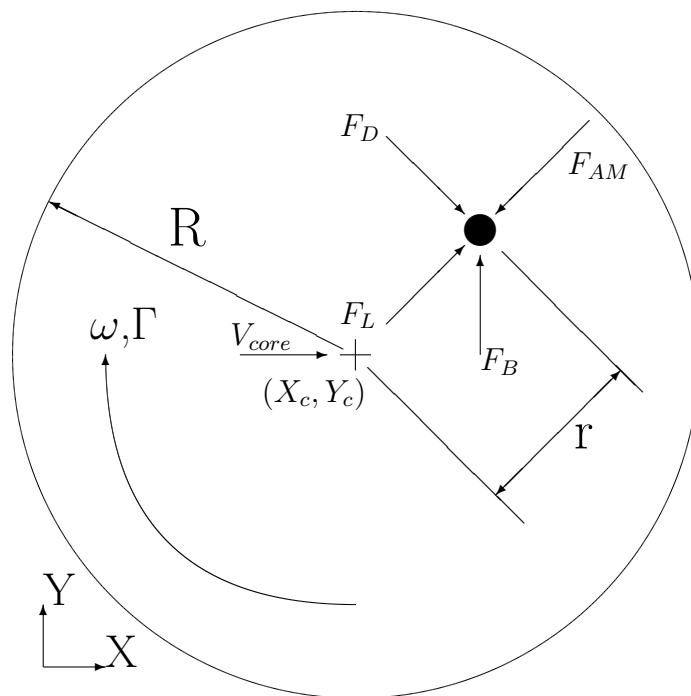


Figure 2.1: A schematic of forces acting on bubbles entrained in a traveling vortex tube

Where,

$$\bar{g} = \frac{gR^3}{\Gamma^2}, \quad \bar{r} = \frac{r}{R}, \quad \bar{\mathbf{U}} = \frac{\mathbf{U}}{\Gamma r/2\pi R^2}, \quad \bar{t} = \frac{2\pi R^2}{\Gamma}, \quad \bar{\omega} = \frac{\omega}{\Gamma/\pi R^2}, \quad \bar{a} = \frac{a}{R}$$

The parameter \bar{r} is the non-dimensional bubble settling location in the vortex core. By combining the parameters \bar{g} and \bar{a} , the non-dimensional variable $\bar{g}\bar{a} = ga^3/\Gamma^2$ can be constructed, which represents a ratio of buoyant forces to hydrodynamic pressure gradient forces experienced by the bubble. For various bubble sizes and vortex strengths, S & K showed that the bubble settling location is dependent mainly on this parameter. Their results will be compared to computations using a DEM approach in section 6.1.

Ferrante & Elghobashi [4] used a two fluid (Eulerian-Eulerian) approach as well as a Lagrangian particle approach similar to the present DEM model to simulate the effects of microbubbles in Taylor-Green vortex flow. They observed that the presence of microbubbles in small volume fraction resulted in a significant decrease in vorticity at the vortex centers. They attributed this vortex distortion to the local, positive divergence of the fluid velocity, $\nabla \cdot \mathbf{U}$, caused by bubble clustering. A similar decrease in core vorticity magnitude due to the bubble clustering is observed in the traveling vortex tube results presented in section 6.1.

Chapter 3 – Mathematical Formulation

The mathematical formulation of the DEM and HLE approaches will now be elaborated. These methods are significantly different in their application, yet the origin of the discretized equations is the same. Conservation of mass and momentum govern the motion of the fluid phase. These are given in vector form as:

$$\frac{\partial \rho \mathbf{u}}{\partial t} + \mathbf{u} \cdot \nabla (\rho \mathbf{u}) = -\nabla p + \nabla \left(\mu_f \left(\nabla \mathbf{u} + (\nabla \mathbf{u})^T \right) \right) + \rho \mathbf{g} + \mathbf{f} \quad (3.1)$$

$$\frac{\partial \rho}{\partial t} + \nabla \cdot (\rho \mathbf{u}) = 0 \quad (3.2)$$

where ρ is the fluid density, \mathbf{u} is the fluid velocity vector, p is the pressure, \mathbf{g} is the acceleration due to gravity, and \mathbf{f} is an arbitrary body force per unit volume. The superscript T denotes the anti-symmetric part of the strain rate, $\nabla \mathbf{u}$, which is zero for an incompressible flow. This Eulerian description of the continuous flow field will be the starting point for both the DEM and HLE approaches. First, the DEM formulation will be described by forming variable density equations that account for the presence of finite size lagrangian particles which are subgrid in scale. A discussion of the HLE formulation will follow, wherein the variable density description of the incompressible flow field is coupled with a rigidity constraint to simulate resolved rigid body motion on cartesian, non body-conformal grids.

3.1 Discrete Element Model with Finite Size Effects

The computations carried out with the Discrete Element Model use Direct Numerical Simulation (DNS) with Lagrangian particle tracking to solve the motion of the spherical, subgrid scale dispersed phase. The particles move freely in the fluid, and their motion is calculated from Newtons laws, using expressions for lift, drag, added mass, gravitational, pressure, and collision forces. When considered as point particles, the dispersed phase can move passively through the fluid (1-way coupling), or can transfer momentum back to the fluid (2-way coupling). Additionally, the finite size of the dispersed phase, can be accounted for (volumetric coupling), and the particles affect the fluid through a variable density formulation of the governing equations. Details of the numeric scheme and model implementation, as well as several validation cases are also provided.

3.1.1 Variable Density Fluid Formulation

Consider a domain Γ which contains a continuous fluid phase, and a dispersed bubbly or particulate phase, denoted by subscript p, as shown in figure 3.1.1. The dispersed phase has a finite, characteristic diameter, ϕ_p , and occupies a volume V_p . The term 'particle' will be used to refer to an individual element of this dispersed phase, but is equally interchangeable with 'bubble' for the modelling of gas-liquid systems. Typical treatment of the dispersed phase as 'point particles' [29] [4] [30] allows the particles to transfer momentum as point sources. In many situations, such as dense, granular flow and particle fluidization, the finite size of the particles

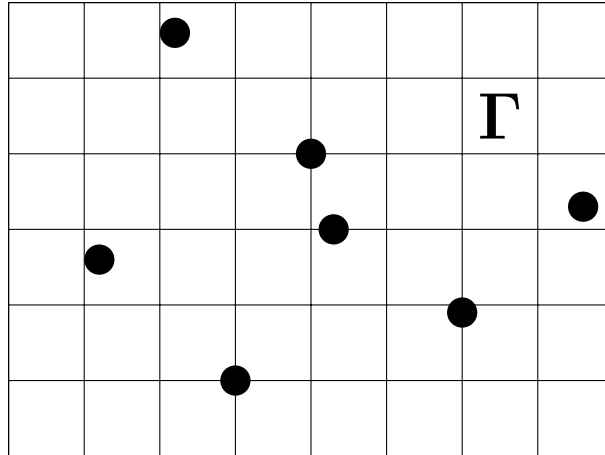


Figure 3.1: Illustration of the fluid domain, Γ containing a subgrid scale dispersed phase.

has an important effect on both the fluid and dispersed phase [2]. The finite size of these particles can be accounted for in the fluid continuity and momentum equations by defining the fluid and dispersed phase volume fractions, Θ_f and Θ_p , where $\Theta_f = 1 - \Theta_p$. The fluid phase continuity equation then becomes [2]:

$$\frac{\partial}{\partial t}(\rho_f \Theta_f) + \nabla \cdot (\rho_f \Theta_f \mathbf{u}_f) = 0 \quad (3.3)$$

Note that in this form, the velocity field is not *divergence free*, even for an incompressible fluid. This can be shown by simple rearrangement of equation 3.3. The particle volume fraction can be described as a property of the fluid, Θ_p , retained at the fluid grid points, if the Lagrangian particle locations can be transferred to the

Eulerian fluid grid points. This is accomplished using the following interpolation:

$$\Theta_p(x_{cv}) = \sum_{p=1}^{N_p} V_p \mathbb{G}_\sigma(x_{cv}, x_p) \quad (3.4)$$

where $\Theta_p(x_{cv})$ is the volume fraction stored at the control volume center. $\Theta_p(x_{cv})$ is affected by all the particles, N_p based on their proximity, $|x_{cv} - x_p|$. The effect that each Lagrangian particle has on a control volume is determined by the interpolation kernel, \mathbb{G}_σ , which is a Gaussian function with origin at the particle centroid, and will be discussed further in section 4.1.1. The momentum equations (3.1) can be altered to account for the variable fluid density resulting in (Zhang & Prosperetti 1997 [31]; Ferrante & Elghobashi 2007 [4])

$$\frac{\partial \rho_f \Theta_f \mathbf{u}}{\partial t} + \nabla \cdot (\rho_f \Theta_f \mathbf{u}_f \mathbf{u}_f) = -\Theta_f \nabla p + \nabla \cdot (\mu_f (\nabla \mathbf{u}_f + \nabla \mathbf{u}_f^T)) + \mathbf{f} \quad (3.5)$$

The body force \mathbf{f} is the force associated with particle to fluid momentum transfer. This Eulerian quantity is gotten from the Lagrangian particles by using an interpolation similar to the fluid volume fraction calculation (equation 3.4). Note that the point particle method may be retained by setting $\Theta_f = 1$ everywhere, thus treating the dispersed phase as point sources of momentum. For passive particles (small Stokes number), one way coupling may be used, whereby \mathbf{f} is assumed to be zero.

3.1.2 Bubble Dynamics

The motions of the dispersed particles are governed by Newton's second law in the Lagrangian reference frame. The equations of motion may be written for each particle as a system of ordinary differential equations:

$$\frac{d}{dt}(\mathbf{x}_p) = \mathbf{u}_p \quad (3.6)$$

$$m_p \frac{d}{dt}(\mathbf{u}_p) = \sum \mathbf{F}_p \quad (3.7)$$

where \mathbf{F}_p is the net force acting on each particle and has the following contributions:

$$\sum \mathbf{F}_p = \mathbf{F}_G + \mathbf{F}_P + \mathbf{F}_D + \mathbf{F}_L + \mathbf{F}_{AM} + \mathbf{F}_{coll} \quad (3.8)$$

The gravitational force, \mathbf{F}_G , due to buoyancy, is the force exerted on a particle of density ρ_p immersed in a fluid of density ρ_f :

$$\mathbf{F}_G = (\rho_p - \rho_f)V_p \mathbf{g} \quad (3.9)$$

where V_p is the particle volume, equal to $\frac{4}{3}\pi R_p^3$ for a sphere. The pressure force, F_P , is the force on the particle due to far field pressure gradients. This is relevant in cases such as bubbles rising in a water column. It is expressed as:

$$\mathbf{F}_P = -V_p \nabla p \quad (3.10)$$

The particle drag force, F_D is a given by:

$$\mathbf{F}_D = -\frac{1}{2}C_D\rho_f\pi R_p^2|\mathbf{u}_p - \mathbf{u}_f|(\mathbf{u}_p - \mathbf{u}_f) \quad (3.11)$$

The particle slip velocity, $(\mathbf{u}_p - \mathbf{u}_f)$ is evaluated using the local velocity field near the particle of interest. Various empirical expressions have been suggested for the drag coefficient, C_D . In this work, the standard drag curve of Schiller and Nauman [32] for sphere drag is used:

$$C_D = \frac{24}{Re_p}(1 + 0.15Re_p^{0.687}) \quad (3.12)$$

Where Re_p is the Reynolds number based on particle slip velocity, $|\mathbf{u}_p - \mathbf{u}_f|$. For large bubbles the drag increase due to bubble deformation can be implicitly accounted for by using a drag coefficient based in part on the Eötvös number (or Bond number) defined as $Eo = (\rho_f - \rho_b)g\phi_b^2/\sigma$, where σ is the interface surface tension. Darmana et al. [33] suggested the following correlation based on experimental data:

$$C_d = \max \left[\min \left[\frac{16}{Re_p}(1 + 0.15Re_p^{0.687}), \frac{48}{Re_p} \right], \frac{8}{3} \frac{Eo}{Eo + 4} \right] \quad (3.13)$$

This correlation has been tested in some of the present cases of interest with good results for larger bubbles. The lift force, F_L , has been the subject of much

discussion in the literature. In general, it can be expressed as:

$$\mathbf{F}_L = -C_L \rho_f \pi R_p^2 (\mathbf{u}_p - \mathbf{u}_f) \times (\nabla \times \mathbf{u}_f) \quad (3.14)$$

Where C_L is the lift coefficient. Ferrante and Elghobashi used $C_L = 1$ in their study of bubble laden Taylor-Green vortex flow. Sridhar & Katz [25] correlated their experimental data of bubbles entrained in vortex rings to the local shear rate, $\alpha = \omega R_p / (\mathbf{u}_p - \mathbf{u}_f)$ where ω is the fluid vorticity, and suggested a lift coefficient of the form:

$$C_L = 0.59 \alpha^{0.25} \quad (3.15)$$

The effect of changing the lift coefficient from unity to equation 3.15 is investigated using bubble entrainment into a Gaussian vortex in section 6.2. All other cases presented assume $C_L = 1$. The added mass force, F_{AM} , is the force which would be exerted on the volume of fluid displaced by the presence of the particle. It is given by

$$\mathbf{F}_{AM} = -\frac{1}{2} \rho_f V_p \left(\frac{D\mathbf{u}_p}{Dt} - \frac{D\mathbf{u}_f}{Dt} \right) \quad (3.16)$$

The collision force, \mathbf{F}_{coll} is a repulsive due force to collision events involving another particle or a wall. It is effective in preventing two coincident particles from occupying the same fluid volume, and assures that the close packed limit of $\Theta_p \approx 0.6$ is respected for spherical particles. The model is the same as used by Joseph & Patankar [34], and based on the distinct element method of Cundal & Strack [35]. The force exerted on spherical particle p due to a collision with spherical particle

j is given by:

$$\mathbf{F}_{pj}^{P-P} = \left(k_c \delta_{pj}^{3/2} - \eta_c (\mathbf{u}_d - \mathbf{u}_f) \cdot \mathbf{n}_{pj} \right) \mathbf{n}_{pj} \quad (3.17)$$

$$\delta_{pj} = (R_{p,p} + R_{p,j} + \rho) - d_{pj} \quad (3.18)$$

where k_c and η_c are stiffness and damping parameters respectively, \mathbf{n}_{pj} is the unit vector from particle j to particle p , and ρ is the repulsive range. The force on particle j is equal and opposite:

$$\mathbf{F}_{jp}^{P-P} = -\mathbf{F}_{pj}^{P-P} \quad (3.19)$$

Estimates of the damping and stiffness parameters were made by Tsuji et al. [36]. In all the present simulations, these parameters take the values of $K_c = 800e - 6$ and $\eta_c = 0.018e - 6$. Particle collisions with solid walls are handled in a similar manner, and the wall collision force on particle p is given by:

$$\mathbf{F}_{pw}^{P-W} = \left(k_c \delta_{pj}^{3/2} - \eta_c \mathbf{u}_d \cdot \mathbf{n}_{pw} \right) \mathbf{n}_{pw} \quad (3.20)$$

$$\delta_{pw} = (R_p + 2\rho) - d_{pw} \quad (3.21)$$

where d_{pw} is the distance from the wall to particle p , and \mathbf{n}_{pw} is the normal vector from the particle to the wall of interest. The *total* collision force on particle p is

the sum of all inter-particle collision forces and all wall collision forces:

$$\mathbf{F}_{coll} = \sum_{j=1}^{N_p} \mathbf{F}_{pj}^{P-P} + \sum_{walls} \mathbf{F}_{pw}^{P-W} \quad (3.22)$$

Additionally, bubble size variations can be accounted for by solving the Rayleigh Plesset equation and including a force due to bubble expansion. This becomes important for cavitation [10] or mass transfer models [11] models based on the discrete bubbles, but is beyond the scope of this work.

The motion of the dispersed phase results in a reaction force which acts on the fluid carrier phase. This is accounted for in the momentum equations by the force \mathbf{f} on the right hand side of equation 3.5, and has contributions from all the surface forces. For clarity, let $\mathbf{f} = \mathbf{f}_{DEM}$, and the two way coupling force is given by:

$$\mathbf{f} = \mathbf{f}_{DEM} = \mathbf{F}_D + \mathbf{F}_L + \mathbf{F}_{AM} + \mathbf{F}_P \quad (3.23)$$

As mentioned, this is distributed onto the Eulerian grid in a similar manner to the particle volume fraction

$$\mathbf{f}(x_{cv}) = \sum_{p=1}^{N_p} \mathbf{f}_{DEM} G_\sigma(x_{cv}, x_p) \quad (3.24)$$

3.2 Fully Resolved HLE Scheme for Rigid Body Motion

The computations carried out with the HLE approach utilize direct numerical simulation (DNS) with fictitious domain representation of arbitrary shaped im-

mersed objects such hydrofoils or freely moving bubbles. The fictitious domain approach Glowinski et al. [7], Patankar [34], Apte et al. [8] allows accurate representation of moving boundaries embedded in a fluid flow. Two types of moving boundaries are considered in this study: (i) specified motion of the immersed object and (ii) freely moving objects. A lifting surface (ie hydrofoil) will have *specified* rigid body motion consisting of translation and rotational velocities. The bubbles or particles simulated are allowed to move *freely*. Their motion is obtained by directly computing the forces acting on them. As the first step, we assume the bubbles are *rigid* objects immersed in a surrounding viscous fluid. Such an assumption is reasonable for low Reynolds numbers and low Weber numbers. For small Weber numbers, the inertial shearing forces acting on the bubble are much smaller than the surface tension forces. Under these conditions bubble deformation is minimal, and the shape of the bubble is preserved. One consequence of this assumption is that modeling the motion of the bubble is much easier; the region occupied by the bubble is forced to undergo rigid body motion consisting of only translation and rotation. The bubble motion is then obtained directly by using a novel algorithm based on fictitious domain method for high-density ratios between the fluid and the immersed object. In this fully resolved simulation approach, models for drag, lift, or added mass forces on the bubble are not required, but such forces are directly computed. Below we describe in detail the computational approach for freely moving rigid objects immersed in a viscous, incompressible fluid. Details of the numerical scheme and several verification and validation test cases are also presented to show good predictive capability of the numerical solver.

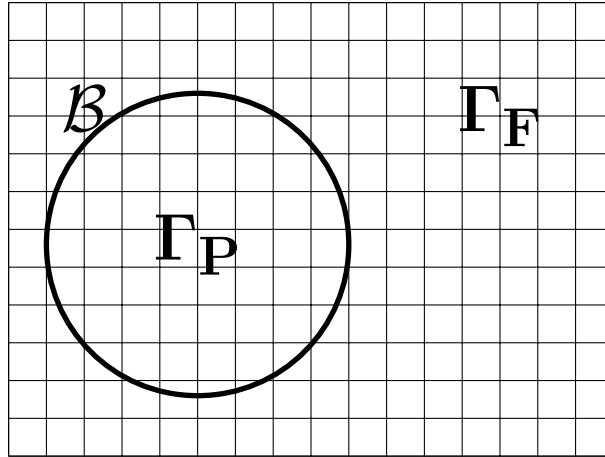


Figure 3.2: Illustration of the fluid domain, Γ_F containing a resolved particle, Γ_P , with boundary \mathcal{B} .

Let Γ be the computational domain which includes both the fluid ($\Gamma_F(t)$) and the particle ($\Gamma_P(t)$) domains shown in figure 3.2. Let the fluid boundary not shared with the particle be denoted by \mathcal{B} and have a Dirichlet condition (generalization of boundary conditions is possible). For simplicity, let there be a single rigid object in the domain and the body force be assumed constant so that there is no net torque acting on the object. The basis of a fictitious-domain approach [7] is to extend the Navier-Stokes equations for fluid motion over the entire domain Γ inclusive of immersed objects. The natural choice is to assume that the immersed object region is filled with a Newtonian *fluid* of density equal to the object density (ρ_P) and some fluid viscosity (μ_F). Both the real and fictitious fluid regions will be assumed as incompressible and thus the incompressibility constraint applies over the entire region. In addition, as the immersed objects are assumed rigid, the motion of the material inside the object is constrained to rigid body motion. Several ways of

obtaining the rigidity constraint have been proposed [7], [37], [34]. We follow the formulation developed by Patankar [34] and described in detail by Apte et al. [8]. A brief description is given here for completeness.

The momentum equation for fluid motion applicable in the entire domain Γ is given by:

$$\rho \left(\frac{\partial \mathbf{u}}{\partial t} + (\mathbf{u} \cdot \nabla) \mathbf{u} \right) = -\nabla p + \nabla \cdot \left(\mu_F \left(\nabla \mathbf{u} + (\nabla \mathbf{u})^T \right) \right) + \rho \mathbf{g} + \mathbf{f}, \quad (3.25)$$

where ρ is the density field, \mathbf{u} the velocity vector, p the pressure, μ_F the fluid viscosity, \mathbf{g} the gravitational acceleration, and \mathbf{f} is an additional body force that enforces rigid body motion within the immersed object region Γ_P . The fluid velocity field is constrained by the conservation of mass which, for an incompressible fluid, simply becomes: $\nabla \cdot \mathbf{u} = 0$.

In order to enforce that the material inside the immersed object moves in a rigid fashion, a rigidity constraint is required that leads to a non-zero forcing function \mathbf{f} . Inside the particle region, the rigid body motion implies vanishing deformation rate tensor:

$$\left. \begin{aligned} \frac{1}{2} \left(\nabla \mathbf{u} + (\nabla \mathbf{u})^T \right) &= \mathbf{D}[\mathbf{u}] = 0, \\ \Rightarrow \mathbf{u} &= \mathbf{u}^{RBM} = \mathbf{U} + \Omega \times \mathbf{r} \end{aligned} \right\} \text{in } \Gamma_P, \quad (3.26)$$

where \mathbf{U} and Ω are the translation and angular velocities of the object and \mathbf{r} is the position vector of a point inside the object from its centroid.

The vanishing deformation rate tensor for rigidity constraint automatically en-

sures the incompressibility constraint inside the particle region. The incompressibility constraint gives rise to the scalar field (the pressure, p) in a fluid. Similarly, the tensor constraint $\mathbf{D}[\mathbf{u}] = 0$ for rigid motion gives rise to a tensor field inside the particle region. A fractional-step algorithm can be devised to solve the moving boundary problem [34, 8]. Knowing the solution at time level t^n the goal is to find \mathbf{u} at time t^{n+1} .

1. In this first step, the rigidity constraint force \mathbf{f} in equation 3.25 is set to zero and the equation together with the incompressibility constraint (equation 3.26) is solved by standard fractional-step schemes over the entire domain. Accordingly, a pressure Poisson equation is derived and used to project the velocity field onto an incompressible solution. The obtained velocity field is denoted as \mathbf{u}^{n+1} inside the fluid domain and $\hat{\mathbf{u}}$ inside the object.
2. The velocity field for a freely moving object is obtained in a second step by projecting the flow field onto a rigid body motion. Inside the object:

$$\rho_P \left(\frac{\mathbf{u}^{n+1} - \hat{\mathbf{u}}}{\Delta t} \right) = \mathbf{f}. \quad (3.27)$$

To solve for \mathbf{u}^{n+1} inside the particle region we require \mathbf{f} . The constraint on the deformation rate tensor given by equation 3.26 can be reformulated to

obtain:

$$\nabla \cdot (\mathbf{D}[\mathbf{u}^{n+1}]) = \nabla \cdot \left(\mathbf{D} \left[\hat{\mathbf{u}} + \frac{\mathbf{f}\Delta t}{\rho} \right] \right) = 0; \quad (3.28)$$

$$\mathbf{D}[\mathbf{u}^{n+1}] \cdot \mathbf{n} = \mathbf{D} \left[\hat{\mathbf{u}} + \frac{\mathbf{f}\Delta t}{\rho} \right] \cdot \mathbf{n} = 0. \quad (3.29)$$

The velocity field in the particle domain involves only translation and angular velocities. Thus $\hat{\mathbf{u}}$ is split into a rigid body motion ($\mathbf{u}^{RBM} = \mathbf{U} + \Omega \times \mathbf{r}$) and residual non-rigid motion (\mathbf{u}'). The translational and rotational components of the rigid body motion are obtained by conserving the linear and angular momenta and are given as:

$$M_P \mathbf{U} = \int_{\Gamma_P} \rho \hat{\mathbf{u}} d\mathbf{x}; \quad (3.30)$$

$$\mathcal{I}_P \Omega = \int_{\Gamma_P} \mathbf{r} \times \rho \hat{\mathbf{u}} d\mathbf{x}, \quad (3.31)$$

where M_P is the mass of the particle and $\mathcal{I}_P = \int_{\Gamma_P} \rho [(\mathbf{r} \cdot \mathbf{r})\mathbf{I} - \mathbf{r} \otimes \mathbf{r}] d\mathbf{x}$ is the moment of inertia tensor. Knowing \mathbf{U} and Ω for each particle, the rigid body motion inside the particle region \mathbf{u}^{RBM} can be calculated.

3. The rigidity constraint force is then simply obtained as $\mathbf{f} = \rho(\mathbf{u}^{RBM} - \hat{\mathbf{u}})/\Delta t$. This sets $\mathbf{u}^{n+1} = \mathbf{u}^{RBM}$ in the particle domain. Note that the rigidity constraint is non-zero only inside the particle domain and zero everywhere else. This constraint is then imposed in a third fractional step.

In practice, the fluid flow near the boundary of the particle (over a length

scale on the order of the grid size) is altered by the above procedure owing to the smearing of the particle boundary. The key advantage of the above formulation is that the projection step only involves straightforward integrations in the particle domain.

The above formulation can be easily generalized to particles with *specified motion* by directly setting \mathbf{u}^{RBM} to the specified velocity. In this case, the integrations (equations 3.30) in the particle domain are not necessary.

Chapter 4 – Numerical Implementation

The DEM and HLE approaches are implemented in a finite volume framework. Several of the same basic techniques (i.e. fractional step and predictor, corrector schemes) are used in both methods, but they will be discussed individually here for clarity. The codes are parallelized using Message Passing Interface (MPI), allowing for larger scale simulations by distributing the required memory over many processors.

4.1 Variable Density Discrete Element Model

The DEM approach is implemented into a solver capable of handling unstructured meshes [29] [38]. This makes application to complex geometries straightforward, and commercial grid generation softwares may be utilized. The solution proceeds using a semi-implicit Fractional Step solver for the fluid phase. The velocity field is first advanced implicitly to an intermediate value, u_i^* . In this step, the convective, and viscous terms are treated implicitly, while the interphase force, \mathbf{f}_{DEM} , is treated explicitly. The old pressure gradient is subtracted, and a pressure Poisson equation is formulated to enforce continuity at t^{n+1} . The velocity field, \mathbf{u}^{n+1} , which satisfies the continuity equation is then gotten from the new pressure gradient. These steps are performed over several inner iterations along with the particle phase advancement from $t^{n+1/2}$ to $t^{n+3/2}$. The particle position and velocity are handled explicitly, and are integrated in time using a smaller sub-timestep. A detailed explanation of the solution algorithm is given in Appendix B.

4.1.1 Gaussian Interpolation Kernel

The main restriction on grid spacing for the variable density formulation is that the particle volume fraction, Θ_p of any given fluid control volume may not exceed unity. The Gaussian interpolation kernel assures that the volume fraction is distributed locally around the particle, however, care must be taken to avoid large regions where the mean grid spacing is less than the mean particle size, ϕ_p . This assures smooth variations in fluid properties and solution convergence. The Gaussian interpolation function is given by

$$\mathbb{G}(\mathbf{x}, \mathbf{x}_p) = \frac{1}{(\sigma\sqrt{2\pi})^3} \left[-\frac{\sum_{k=1}^3 (x_k - x_{p,k})^2}{2\sigma^2} \right] \quad (4.1)$$

where $\sigma = V_{cv}^{1/3}$. In addition, \mathbb{G} is normalized to satisfy:

$$\int_{V_{cv}} \mathbb{G}_\sigma(\mathbf{x}_{cv}, \mathbf{x}_p) dV = 1 \quad (4.2)$$

where the integration is performed over the cv containing the particle and all of its neighbors. In this way, mass and volume conservation are ensured. A single particle affects the volume fraction of all the neighboring nodes of the grid cell containing it, and the distribution of Θ_p is smooth. For a detailed discussion and demonstration of the kernel, the reader is referred to Apte et al. [29] and [2]

4.1.2 Variable Storage and Discretization

Figure 4.1 shows the variable storage locations in time for the continuous fluid phase and the dispersed, particle phase. The fluid phase pressure, p , and face based momentum flux, $\rho \mathbf{u}_i$ are stored at t^n and t^{n+1} . The dispersed phase location, \mathbf{x}_p is forward staggered in time and is advanced explicitly from $t^{n+1/2}$ to $t^{n+3/2}$. The particle volume fraction, Θ_p is computed directly at these staggered time levels by interpolating the Lagrangian quantity \mathbf{x}_p onto the Eulerian grid using equation 3.4, and the Gaussian kernel. The particle velocity, \mathbf{u}_p is stored at t^n and t^{n+1} , to be consistent with the fluid solution. Consequently, no time extrapolation is required to compute the particle motion from equation 3.8 because the fluid pressure and velocity fields are known *a-priori*. The two-way coupling force, \mathbf{f}_{DEM} is also computed at the $n + 1$ time level and is distributed from the particles to the fluid in the same manner as Θ_p

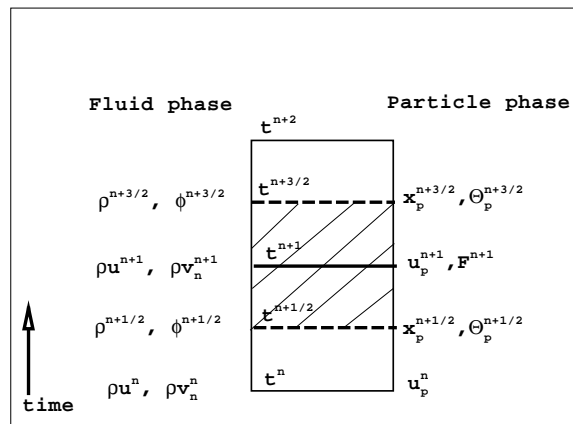


Figure 4.1: Schematic of DEM variable storage in time.

Values of pressure, velocity, and density associated with the fluid phase are

co-located at the cell center. This provides greater flexibility for dealing with non-uniform grids and complex geometries. Interpolation to the faces, when necessary, is accomplished by taking the arithmetic mean of the cell centered quantity at the two nodes sharing the face of interest.

4.2 Hybrid Eulerian Lagrangian (HLE) Method

The mathematical formulation of the HLE method is implemented in a co-located, structured grid, three-dimensional flow solver based on a fractional-step scheme developed by Apte et al. [8]. Modifications to the original scheme for freely moving objects were made in order to handle large density ratios ($\mathcal{O}(1000)$) representative of water-to-air bubbles. Accordingly, in the present work the fluid-particle system is solved by a *three-level fractional step scheme*. First the momentum equations (without the pressure and the rigidity constraint terms) are solved. The incompressibility constraint is then imposed by solving a *variable-coefficient Poisson equation* for pressure. Finally, the rigid body motion is then enforced by constraining the flow inside the immersed object to translational and rotational motion. The main steps of the numerical approach are given in Appendix C

4.2.1 Immersed Object Representation

In the numerical implementation, we create small material volumes of cubic shape that completely occupy the immersed object (see Figure 4.2). Each material vol-

ume is assigned the properties of the immersed object (e.g. density etc.). The shape of the object can be reconstructed from these material volumes by computing an indicator or color function (with value of unity inside the object and zero outside) on a fixed background mesh used for flow solution. In this work, the material volumes are forced to undergo rigid motion, based on the translational and rotational velocities of the object, resulting in no relative motion among them. At each time-step the material volumes are advanced to new locations. In the present

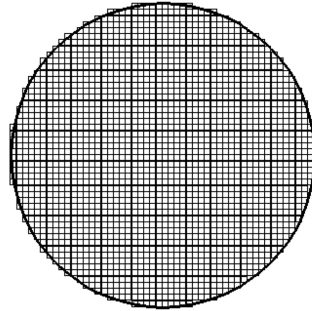


Figure 4.2: Schematic of material volumes for a circular object.

approach, the boundary of the object is represented in a stair-stepped fashion and it is straightforward to create the material volumes using a bounding-box algorithm [8]:

1. Determine the bounding box for the particle based on its surface representation.
2. Generate cubic grid within the bounding box.
3. Use distance searches to determine if the centroid of the control volume lies within the bounding surface of the particle.

4. Eliminate points outside the particle domain.

The total mass of the material volumes generated will be exactly equal to the mass of the particle if the surface of the particle aligns with the grid. The stair-stepped surface representation, however, results in an error in the total mass of the material volumes compared to the original shape. This error reduces with an increase in the total number of material volumes per object. A more complex grid generation process based on Delaunay triangulation can be used to accurately represent the surface of the object by using standard body-fitted grid generation tools. In the present work; however, we use sufficient number of material volumes to represent the object boundary and follow the stair-stepped approach owing to its simplicity.

4.2.2 Variable Storage & Discretization

Figure 4.3 shows the schematic of variable storage in time and space. All variables are stored at the control volume (cv) center with the exception of the face-normal velocity u_N , located at the face centers. The face-normal velocity is used to enforce the continuity equation. Capital letters are used to denote particle fields. The time-staggering is done so that the variables are located most conveniently for the time-advancement scheme. We follow the collocated spatial arrangement for velocity and pressure field [38], [39]. Accordingly, the particle positions (X_i), density (ρ), volume fraction (Θ), viscosity (μ), and the pressure (p) are located at time level $t^{n-1/2}$ and $t^{n+1/2}$ whereas the velocity fields (u_i , u_N , and U_i) and the rigid body constraint force $f_{i,R}$, are located at time level t^n and t^{n+1} . This makes the

discretization symmetric in time, a feature important to obtain good conservation properties.

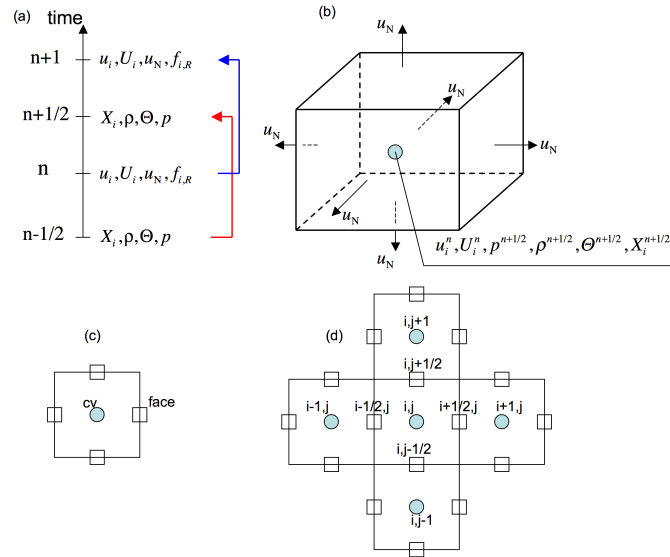


Figure 4.3: Schematic of the variable storage in time and space: (a) time-staggering, (b) three-dimensional variable storage, (c) cv and face notation, (d) index notation for a given k -index in the z direction. The velocity fields (u_i , u_N) are staggered in time with respect to the volume fraction (Θ), density (ρ), and particle position (X_i), the pressure field (p), and the rigid body force ($f_{i,R}$). All variables are collocated in space at the centroid of a control volume except the face-normal velocity u_N which is stored at the centroid of the faces of the control volume.

Chapter 5 – Validation

A complete pre-cavitation model of the bubble laden hydro-propulsion interaction problem described in the introduction must have methods to capture the following:

- Forced translation & rotation of a solid rigid boundary of arbitrary shape
- The motion of fully resolved, freely moving bubbles
- The motion of sub-grid scale bubbles and their effects on the fluid
 - Bubble to fluid momentum transfer: 2 way coupling
 - Finite fluid displacement by the bubble: volumetric coupling
- The effects of bubble-bubble collisions and bubble-boundary collisions
- Various bubble behavioral regimes, ranging from highly disperse to dense clustering

Furthermore, the scales of bubble-flow interaction are important to consider. In larger scale interaction problems, it may be appropriate to model the bubbles as point particles using the DEM model. At other times, smaller scale interactions may require the HLE method to resolve the no slip condition at the bubble surface. It is important to understand the capabilities and limitations of the two models in situations typical of the sub-problems listed above. To this aim, the following cases are presented to provide confidence in the overall methodology.

To first show the accuracy and consistency of the HLE and DEM methods, flow over a circular cylinder at various Reynolds numbers is simulated using a

body fitted grid approach and the DEM scheme, as well as the fictitious domain HLE scheme. Next, to show the HLE method's ability to handle complex geometries, flow over a NACA 0008 hydrofoil is simulated, and results are compared to previous numerical studies. Third, the simulation of an inline oscillating cylinder is conducted to show the accuracy of the HLE scheme to forced rigid body motion. Next, three cases are presented for *freely* moving particles. First, the settling of a sphere in a closed container is considered using the HLE method, and comparisons are made to experimental data. Second, the rise of a buoyant sphere is simulated using both the HLE and DEM approaches at low and high density ratios to compare the two methods. Finally, a three dimensional falling blob is simulated using the DEM approach to show the model's versatility and applicability to dense, dispersed phase induced flow.

5.1 Flow Past a Cylinder at a Range of Reynolds Numbers

Flow past a circular cylinder is simulated at Reynolds numbers of 40, 100, 300, and 1,000. The Reynolds number range is chosen so that both steady and transient wakes are observed. Two different methods are used. First, the solution is computed on a body fitted grid using the DEM flow solver with no dispersed phase. The body fitted mesh is composed of 250,000 hexahedral elements and was generated using the commercial package GAMBIT. The domain is two dimensional with 4 cells and periodic conditions imposed in the spanwise direction. Next, the HLE approach is used with uniform cartesian grids and various levels of refinement in the region near the cylinder. Three successively refined cartesian grids are used so that grid convergence can be studied [8]. The coarse grid employs 350 x 350 points with 35 points inside the cylinder, the medium grid uses 500 x 500 points with 60 points inside the cylinder, and the fine grid uses 600 x 600 grid points with 100 points inside the cylinder. The body fitted grid lies between the coarse grid and the medium grid in terms cylinder surface resolution. A more detailed description of both the body fitted grid and the HLE grids may be found in appendix A.

5.1.1 Recirculation Length

Figure 5.1 shows the flow around the cylinder at $Re_d = 40$. At this Reynolds number, the flow is steady and completely two-dimensional. The recirculation length in the wake is measured as the distance from the rearmost point of the cylinder to the farthest point in the wake with negative streamwise velocity. Shu et al. [40]

cite several values of recirculation length ($2L/D$) obtained both experimentally and computationally which range from 4.26 to 4.69. The HLE simulation results in a recirculation length of $2L/D = 4.58$ and a value of 4.66 is obtained from the body fitted grid simulation. At the higher Reynolds numbers presented, the flow is transient, and a steady recirculation length does not exist.

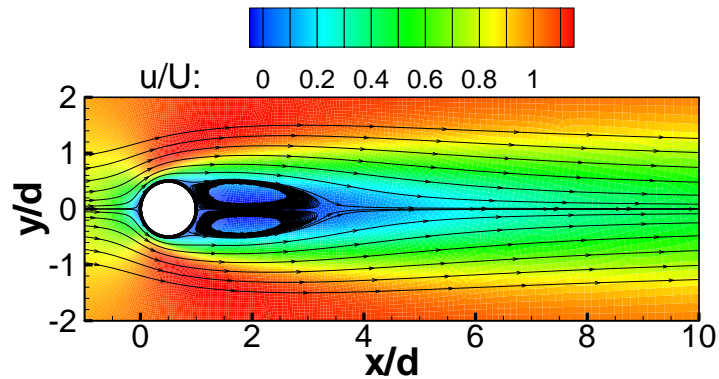


Figure 5.1: Streamlines of flow over the cylinder at $Re_d = 40$. Contours are of streamwise velocity (u) normalized by free stream velocity (U)

5.1.2 Lift & Drag Coefficients

The time evolution of the calculated lift and drag coefficients at each Reynolds number are shown in figures 5.2a - 5.2d. At $Re_d = 40$, the lift coefficient is zero at all times, and the drag coefficient does not change appreciably after a non dimensional time, tU/d , of about 50. The evolution of both quantities is the same for both methods, indicating that they are consistent at this Reynolds number. The drag coefficient reaches a grid dependent value of between 1.53 and 1.55 after

a non-dimensional time of $tU_\infty/d = 200$, which is in agreement with several other studies summarized in table 5.1. Also shown are data for the other values of Re_d considered. Flow over a cylinder at $Re_d = 100$ is well known to be unsteady and two-dimensional. Lift force oscillations begin at $tU/d = 30$ in the body fitted results and at $tU/d = 50$ in the HLE results. The earlier onset of oscillations in the body fitted simulation may be due to the non-uniform grid employed in the wake of the body fitted cylinder. These oscillations reach constant amplitude and continue at a constant frequency for the length of the simulation. The mean value of C_d obtained from the body fitted, DEM simulation is in agreement with other 2D numerical studies and the results show improvement with increased grid refinement in the HLE simulations. At $Re_d = 300$, the cylinder wake is experimentally known to be three dimensional. Lift and drag force oscillations begin earlier than at $Re_d = 100$. Despite the inherent three dimensionality of the flow, the value of C_d computed with the body fitted results agrees well with both 2D and 3D numerical studies, indicating that overall 3D effects may be relatively weak. The HLE results again improve with grid refinement at this Reynolds number. At $Re_d = 1,000$, the lift and drag oscillations begin very quickly, and the amplitude of oscillation does not become steady, even after $tU_\infty/d = 160$. The mean values however, stay steady at 1.44 and 1.50 for the body fitted and HLE simulations respectively, which are comparable with [22] and [41], both 2D simulations.

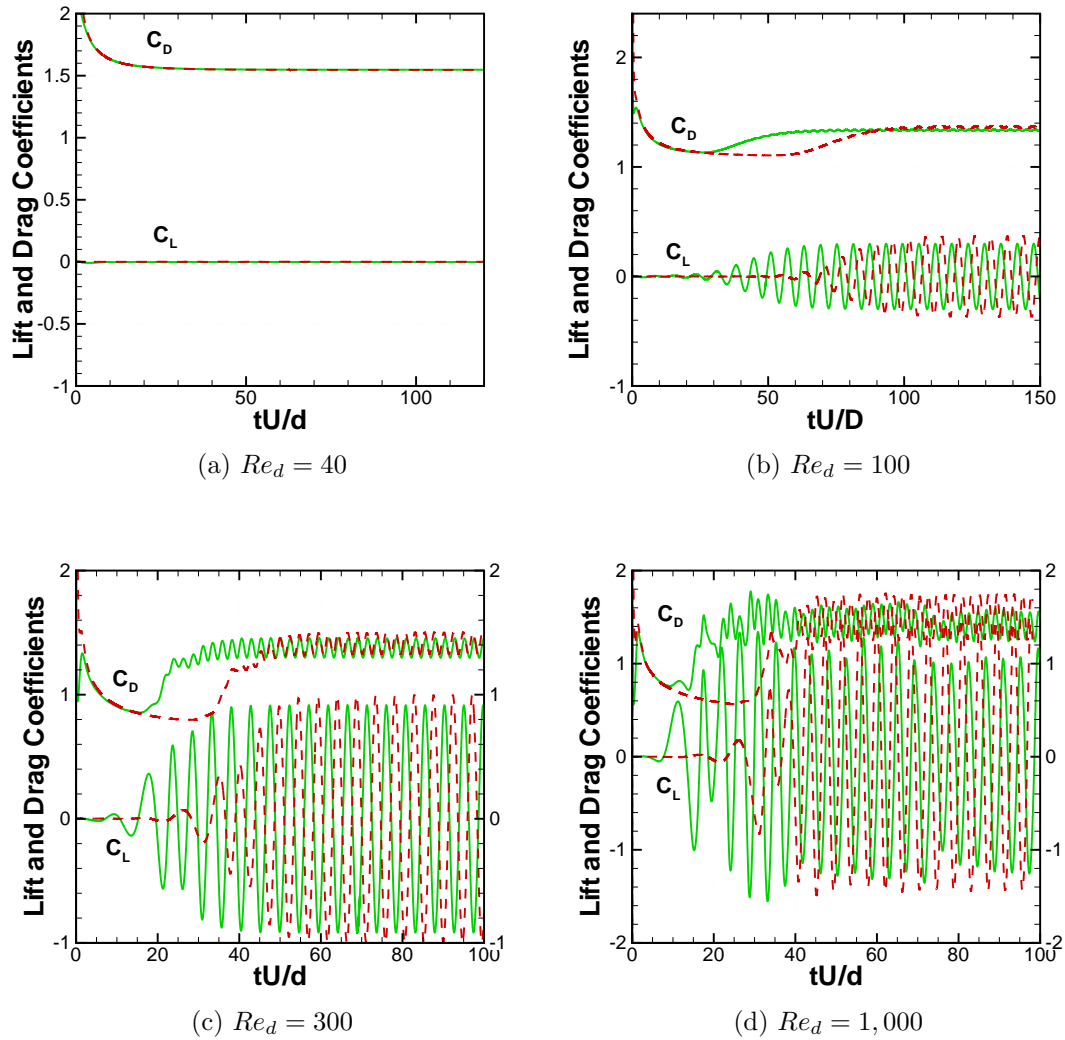


Figure 5.2: Time evolution of computed lift and drag coefficients. (—)Body fitted DEM result (---) HLE fine grid result (a) $Re_d = 40$, (b) $Re_d = 100$, (c) $Re_d = 300$, (d) $Re_d = 1,000$

Table 5.1: Comparison of C_d with previous studies

Re_d	40	100	300	1000
Present body fitted grid	1.55	1.34	1.38	1.44
Present HLE coarse grid	1.54	1.38	1.44	-
Present HLE medium grid	1.53	1.37	1.42	-
Present HLE fine grid	1.54	1.36	1.41	1.50
Mittal et al. (2D) [22]	1.53	1.35	1.36	1.45
Marella et al. (2D) [42]	1.52	1.36	1.28	-
Mittal and Balachandar (3D) [43]	-	-	1.37	-
Henderson (2D) [41]	1.54	1.35	1.37	1.51
Shu et al. (2D) [40]		1.3833		

5.1.3 Strouhal Number of Lift Oscillations

At Reynolds numbers of 100 and higher, the wake behind the cylinder becomes unsteady due to the shedding of alternating vortices. The parameter often associated with periodic vortex shedding is the Strouhal number, defined as:

$$St = \frac{fd}{U} \quad (5.1)$$

where, f is the characteristic frequency of vortex shedding, d is the cylinder diameter, and U is the free stream velocity. This periodic vortex shedding is shown in figure 5.3 for $Re_d = 100$ and 300. The body fitted results and the HLE results show very little difference in vorticity contours at either Reynolds number. The characteristic Karman vortex street is present for both cases, and the spacing of the vortices in the higher Reynolds number case is smaller, suggesting a higher frequency. The frequency of lift oscillations shown in figure 5.2 can be used as the characteristic frequency of vortex shedding. The present results for Strouhal num-

ber calculated in this way are summarized in table 5.2, and comparisons made to several prior studies. At $Re_d = 100$ and 300 , the 3D effects are small, and good agreement is obtained with the other studies for both methods. At $Re_d = 1,000$, the two-dimensional assumption breaks down severely, and the results are not comparable to 3D data [43]

Table 5.2: Comparison of computed Strouhal number with previous studies

Re_d	100	300	1000
Present: body fitted grid	0.165	0.21	0.160
Present: HLE coarse grid	0.166	0.205	-
Present: HLE medium grid	0.165	0.211	-
Present: HLE fine grid	0.165	0.212	0.238
Mittal et al.(2D) [22]	0.166	0.21	0.23
Shu et al.(2D) [40]	0.16	-	-
Kravchenko et al. (3D) [44]	-	0.203	-

5.1.4 Wake Statistics

To further show the accuracy and consistency of both schemes, time averages of mean velocity, turbulent kinetic energy, and Reynolds stress are taken at 5 positions in the wake of the cylinder at $Re_d = 300$. Results from the body fitted grid and the HLE scheme are compared to data extracted from the 3D spectral DNS simulations performed by Mittal and Bachlandar [43]. The flow was allowed to reach consistent values of strouhal number and C_L fluctuation amplitude before statistics were collected ($tU_\infty/d = 70$). Averages were then taken over a period of $tU_\infty/d = 100$. Figure 5.4 shows the present results compared to the 3d data. For

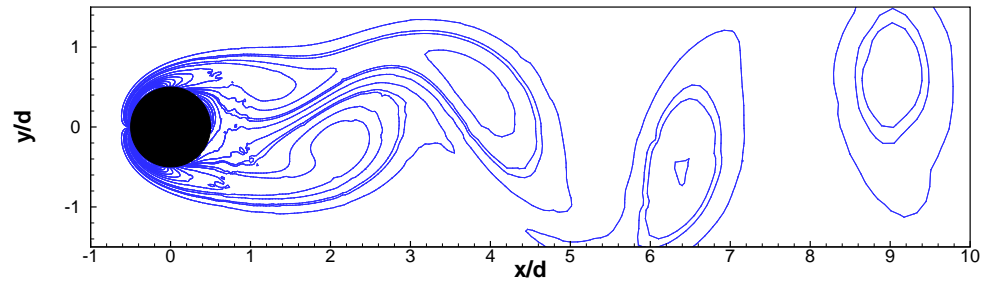
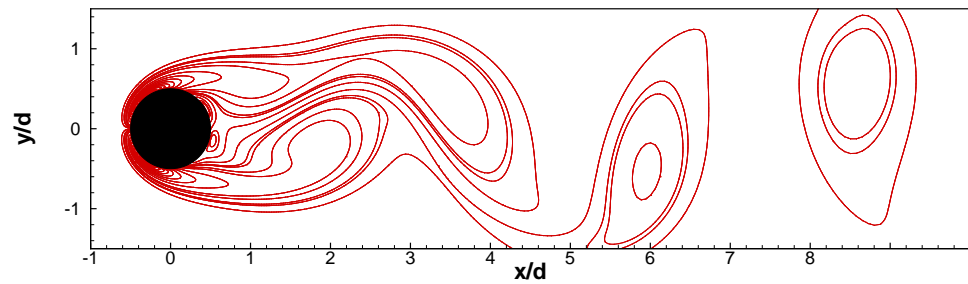
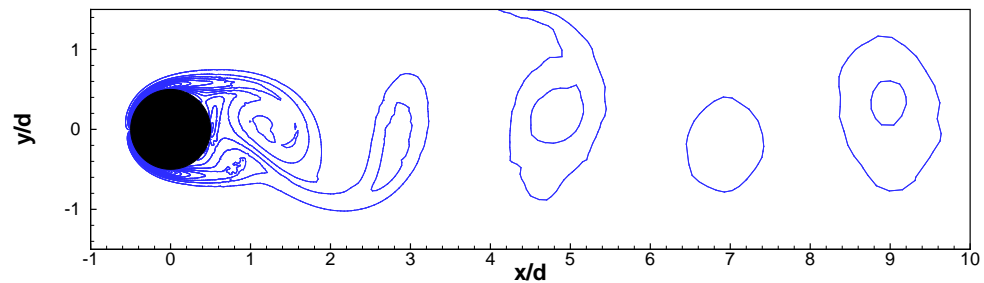
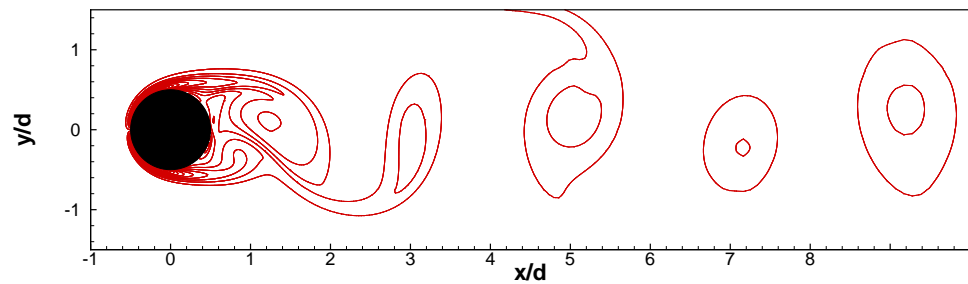
(a) $Re_d = 100$: Body Fitted Grid(b) $Re_d = 100$: HLE(c) $Re_d = 300$: Body Fitted Grid(d) $Re_d = 300$: HLE

Figure 5.3: Comparison of the Karman vortex streets generated behind the cylinder at $Re_d = 100$ & $Re_d = 300$ for both the body fitted grid and the HLE scheme. (a) $Re_d = 100$, body fitted DEM result. (b) $Re_d = 100$, HLE result, (c) $Re_d = 300$, body fitted DEM result. (d) $Re_d = 300$, HLE result

the entire range of results, there is excellent agreement between the body fitted DEM results and the fine grid HLE results, showing the equivalence of the two methods. Qualitatively, the results are quite similar to the three-dimensional data, and the exceptions arise from the two dimensionality of the present simulations. First, the mean flow in the streamwise direction is generally over-predicted by the current methods. From continuity, if the third component of velocity, W , tends toward zero (as in this periodic, 2D simulation) there will be a corresponding amplification of streamwise velocity, U and cross-stream velocity, V . Second, note that both components of kinetic energy and the $u'v'$ Reynolds stress are generally over predicted. If the mechanism of KE transfer to the third direction is suppressed, this is also a logical result. Thus in the absence of 3D results for the present methods, the 2d temporal statistics may be considered sound. It is worth noting that Mahesh et al. [45] were able to accurately reproduce the spectral statistics using Large Eddy Simulation with a surface resolution 4.5 times as fine as the present study, and a fully 3 dimensional geometry.

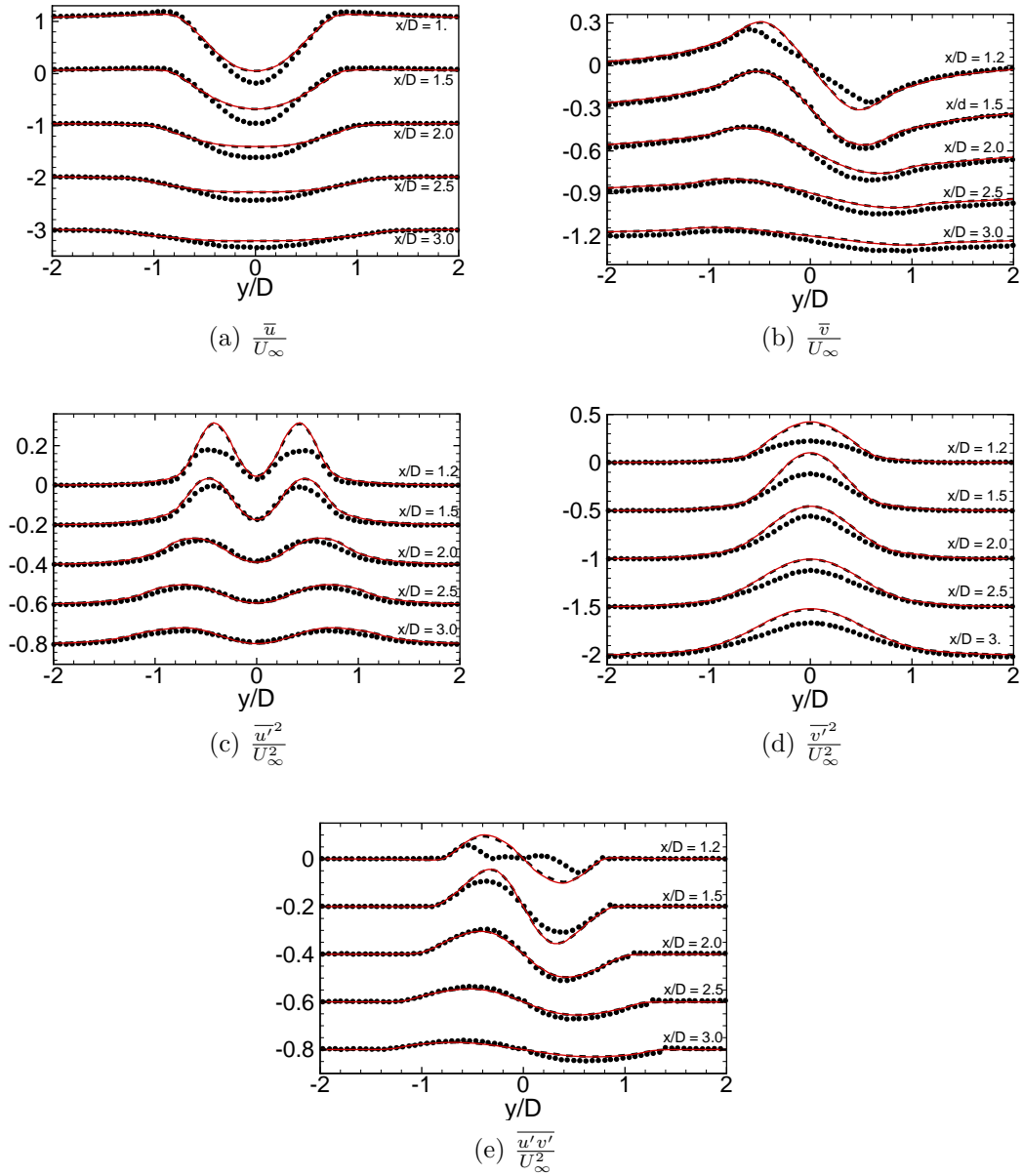


Figure 5.4: Vertical Profiles at 5 positions downstream of the cylinder: (—)HLE solution, (- - -)Body fitted DEM solution (\cdots)3D Spectral simulations by Mittal & Balachandar.

5.2 Flow Over a Stationary NACA 0008 Hydrofoil at $Re_c = 2,000$

The computational solution of flow over a stationary NACA 0008 hydrofoil is presented to show the applicability of the HLE approach to irregular geometries. The thin hydrofoil geometry is challenging for this method because of the small radius at the foil's leading edge and the sharp tip at the trailing edge. These features lead to distinct lift and drag characteristics associated with the geometry, and it is important for any flow solver to properly resolve them. In the HLE approach, these features are not explicitly represented by fitting a grid to the foil surface. Consequently, significant grid refinement is required in the hydrofoil region, so the surface shape is not compromised. The advantages to the HLE approach are that little grid modification is required for geometry change, and forced motion of the hydrofoil may be specified in order to study flapping type locomotion.

A two dimensional flow is assumed, and a block type cartesian grid with periodic boundaries in the spanwise direction is generated using $504 \times 200 \times 4$ grid points in the streamwise, crossstream, and spanwise directions respectively. The domain itself is $13c$ long in the streamwise direction and $8c$ wide in the crossstream direction, where c is the hydrofoil chord length. The grid around the hydrofoil and in the near wake is uniform and cubic with spacing equal to $c/400$. A close up of the grid in the near hydrofoil region is shown in figure 5.5. Also shown is the shape of the leading edge as resolved by the HLE method. By comparison, Mittal et al. [22] used 926×211 grid points in the x and y directions for a cartesian grid

Table 5.3: Computational parameters used in the hydrofoil case

Re_c	α	L_x	L_y	N_x	N_y	N_z	$\frac{c}{\Delta_x}$
2,000	$0^\circ, 4^\circ$	$13c$	$8c$	504	200	4	400

based immersed boundary solution. Kunz & Kroo [46] used a body fitted C-grid and a two dimensional solver with 256×64 grid points in the hydrofoil plane. The chord based Reynolds number, $Re_c = \rho U_\infty c / \mu$, is fixed at 2,000. Two angles of attack $\alpha = 0^\circ$ and $\alpha = 4^\circ$ are used. The simulations are run for 15 non dimensional time units, $\frac{tU_\infty}{c}$. Relevant computational parameters are summarized in table 5.3

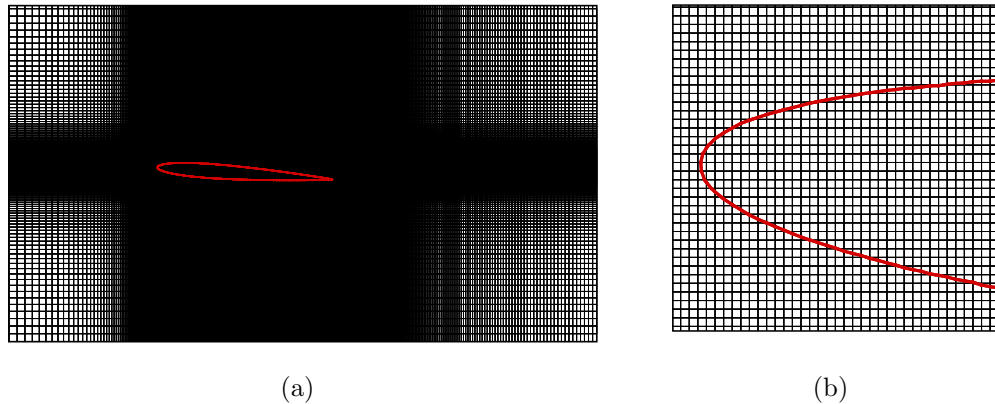


Figure 5.5: (a) The block type cartesian grid used for simulation of flow over the NACA 0008 hydrofoil.(b) Close up of the grid near the hydrofoil leading edge. The hydrofoil surface is shown in red.

At this Reynolds number, the flow is laminar, two-dimensional and steady. Figure 5.6 shows the contours of vorticity for $\alpha = 0^\circ$ and 4° after the flow has reached steady state. At $\alpha = 0$, the flow is symmetric, and the wake is quite

narrow. At $\alpha = 4$, the wake is widened, and separation is indicated on the suction side by detachment of the high vorticity region from the surface.

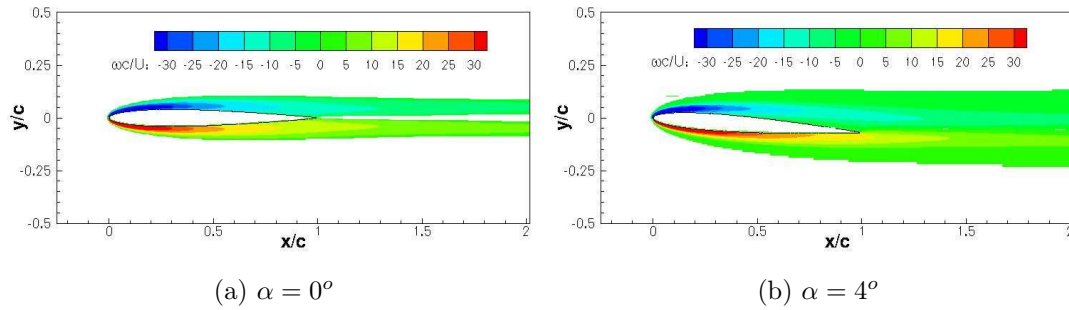


Figure 5.6: Contours of vorticity (out of the page) for flow around a NACA 0008 hydrofoil at $Re = 2,000$

The lift and drag coefficients for the hydrofoil are given as:

$$C_D = \frac{F_D}{\frac{1}{2}\rho U_\infty^2} \quad (5.2)$$

$$C_L = \frac{F_L}{\frac{1}{2}\rho U_\infty^2} \quad (5.3)$$

The temporal evolution of these coefficients is shown in figure 5.7 for both angles of attack. The lift coefficient for $\alpha = 0^\circ$ is not shown because it is zero due to flow symmetry. The steady state values of C_L and C_D are taken after 15 time units and are compared to the results of Mittal et al. and Kunz & Kroo in table 5.4. The present steady state values are in good agreement with the previous computational studies, showing that the HLE method is capable of properly characterizing flow around this irregular geometry.

Table 5.4: Comparison of steady state drag and lift coefficients with other 2D computational results

Study	$\alpha = 0^\circ$		$\alpha = 4^\circ$	
	C_D	C_L	C_D	C_L
Present Results	0.078	-	0.083	0.266
Mittal et al. [22]	0.078	-	0.081	0.273
Kunz & Kroo [46]	0.076	-	0.080	0.272

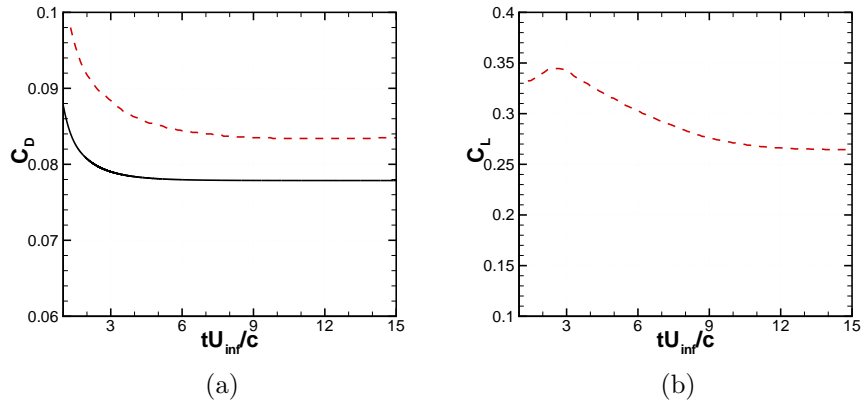


Figure 5.7: Evolution of (a)drag and (b)lift coefficients for flow over a NACA 0008 hydrofoil at $Re = 2,000$. (—) $\alpha = 0^\circ$, (---) $\alpha = 4^\circ$

5.3 Inline Oscillation of a Circular Cylinder

In addition to flow over a fixed objects, the HLE method is used to simulate the flow around a circular cylinder performing linear oscillations. This is intended to validate the approach for flows with forced rigid body motion. The oscillating cylinder problem can be described in terms of the maximum cylinder Reynolds number and the Keulegan-Carpenter number:

$$Re = \frac{U_m d}{\nu} \quad (5.4)$$

$$KC = \frac{U_m}{fd} = \frac{2\pi A}{d} \quad (5.5)$$

where, U_m is the maximum cylinder velocity, ν is the kinematic viscosity of the fluid, f is the frequency of cylinder oscillations, and A is the oscillation amplitude. The cylinder and fluid both start at rest. At $t > 0$, the cylinder position and velocity are described by the sinusoidal functions:

$$x_c(t) = -A_m \sin(2\pi ft) \quad (5.6)$$

$$U_c(t) = -2\pi A f \cos(2\pi ft) \quad (5.7)$$

The relevant computational parameters for this simulation are summarized in table 5.5. The cylinder diameter, viscosity, maximum velocity, and oscillation amplitude are chosen so that $Re = 100$, and $KC = 5$. For these values, we can make direct comparisons to the experimental results of Dütsch [47], and the numerical results of Kim & Choi [48].

Table 5.5: Computational parameters used in the oscillating cylinder case

Re_d	KC	d [m]	ν [m^2/s]	U_m [m/s]	A [m]
100	5	0.01	1e-5	0.1/s	7.96e-3

The computational domain is shown in figure 5.8a. Similar to the hydrofoil case, a block-type cartesian grid is used, with a uniform patch in the region of cylinder motion, and periodicity assumed in the spanwise direction. The domain size is $50d \times 50d$ in the x and y directions, where d is the cylinder diameter. Near the cylinder, a uniform grid spacing of $\Delta_{grid} = d/30$ is used to resolve the cylinder surface. In total, $300 \times 200 \times 2$ grid points are used in the $x, y,$ and z directions. The HLE representation of this surface and the corresponding distribution of Lagrangian material points are shown in figure 5.8b. The method of distributing the material points differs slightly from the approach used for the hydrofoil. Rather than distribute the material points everywhere in the cylinder, they are distributed in a band which is 4 grid points thick around the cylinder surface. As the cylinder moves, this band of material points moves with it, and the rigidity constraint is enforced in the banded region. This offers a significant reduction in the number of material points required, and a corresponding reduction in memory requirements when compared to the non-banded formulation. Apte et al. [8] have run the same case using a non-banded approach, and this case serves as a validation for the new formulation.

The flow is allowed to develop for 11 complete oscillations before collecting data. Figure 5.9 shows the vorticity contours at four different phase angles of

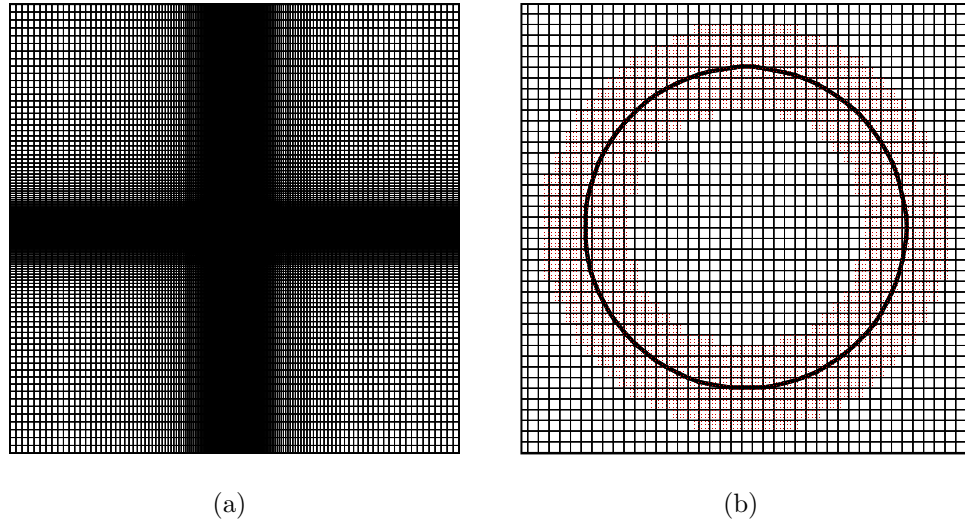


Figure 5.8: (a) Computational domain showing the block type cartesian grid. (b) The cylinder surface shape resolved on the cartesian grid by the HLE method. The red points are the Lagrangian material points used to enforce rigid body motion.

oscillation. At this Reynolds number and KC number, the flow is characterized by a pair of counter rotating vortices being shed from the top and bottom of the cylinder every half cycle. Upon reversing direction at $\phi = 0^\circ$ and 90° , the cylinder destroys the previously formed pair while creating a new pair in its wake. The vertical profiles of oscillating direction velocity are shown in figure 5.10 for three different phase angles. The present results are compared with the experimental data, as well as the computations by Apte et al. using the non-banded formulation. Both results show very good agreement with both the experimental data, and the computational results of Kim & Choi. There is very little difference between the current results, and the non-banded results for any of the wake profiles, suggesting that the decrease in computational expense comes with no loss of accuracy.

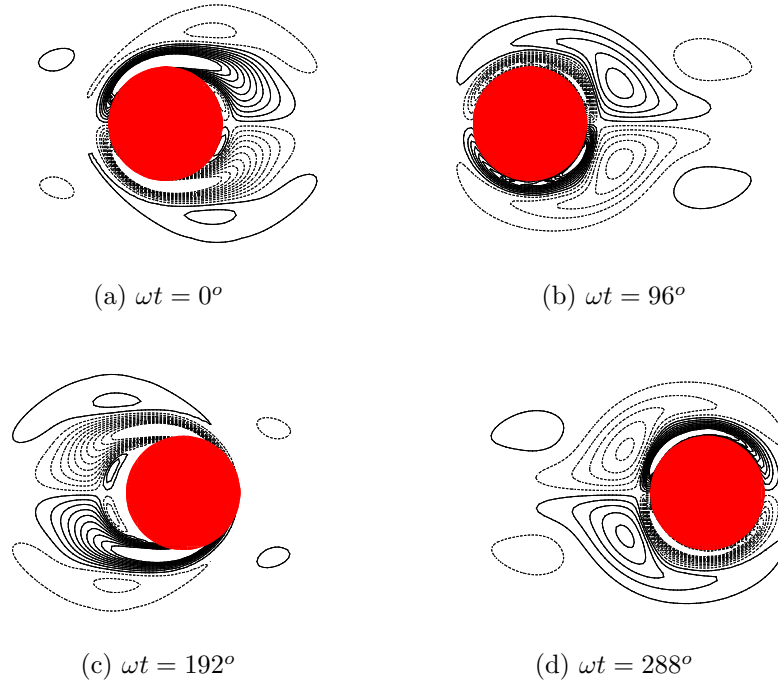


Figure 5.9: Contours of normalized vorticity in the wake of the oscillating cylinder. Contours range from $\omega d/U_m = -8.5$ to $+8.5$ in increments of -0.85 . Dashed contours denote a negative value.

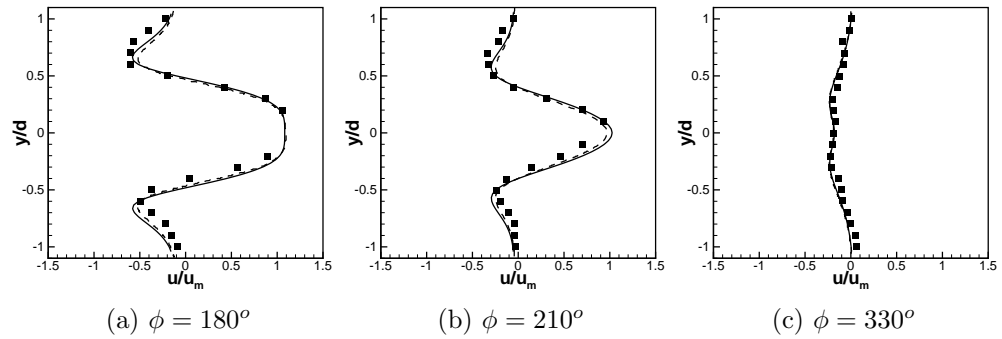


Figure 5.10: Comparison of wake velocity in the oscillating direction for three different cylinder phase angles. —, Present result with banded material point formulation; ---, Computational result from Apte et al. [8] using non banded rigid body approach. ■, experimental result of Dütsch et al. [47]

5.4 The Falling Sphere Problem

Simulations of a single sphere falling under gravity in a closed container are conducted using the HLE approach in order to validate the method for *freely* moving rigid bodies. The particle density is ($\rho_p = 1120 \text{ kg/m}^3$) and the diameter is ($d_p = 15 \text{ mm}$). The sphere is settling in a box of dimensions $10 \times 10 \times 16 \text{ cm}^3$. The particle is released at a height $H = 12 \text{ cm}$ from the bottom of the box. The boundaries of the box are treated as no-slip walls. The fluid properties are varied to obtain different Reynolds numbers based on the terminal velocity of the particle. The simulation conditions correspond to the experimental study by ten Cate *et al.* [49]. Table 5.6 provides detailed information about the parameters used in this test problem.

Table 5.6: Parameters for the sedimenting sphere test problem.

Case Name	$\rho_F \text{ (kg/m}^3\text{)}$	$\mu_F \text{ (10}^{-3}\text{Ns/m}^2\text{)}$	$u_\infty \text{ (m/s)}$	$Re_p = \frac{\rho_F u_\infty d_p}{\mu_F}$
C1	970	373	0.038	1.5
C2	965	212	0.06	4.1
C3	962	113	0.091	11.6
C4	960	58	0.128	31.9

A fine uniform grid of $100 \times 100 \times 160$ points is used with a grid resolution of $\Delta = 1 \text{ mm}$. This provides around 15 grid points inside the particle domain. The material volumes are cubical with $\frac{\Delta}{\Delta_M} = 5$, where Δ_M is the size of the material volume. Accordingly, there are around 75 material volumes along the diameter of the spherical particle in each direction. A uniform time-step ($\Delta t = 0.5 \text{ ms}$)

is used for all cases. This time step is in the same range as the one used in Lattice Boltzmann simulations by ten Cate *et al.* [49] and simulations by Feng & Michaelides [50] based on Proteus. For this time step the $CFL \leq 0.1$ at all times. Later we conduct convergence study of this case with varying grid sizes and time-steps to show their effects on the solution.

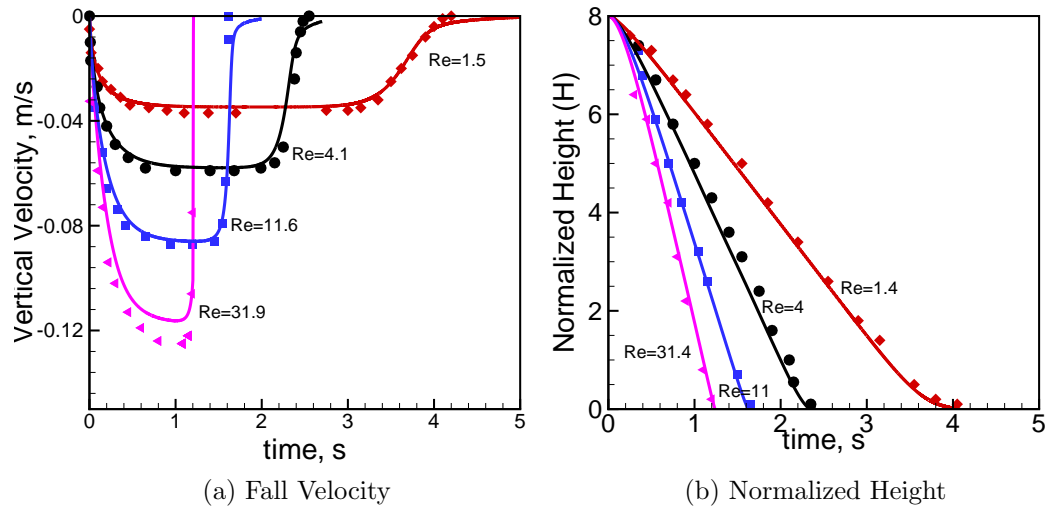


Figure 5.11: Comparison with the experimental data of the sphere fall velocity and the normalized height from the bottom wall for different Reynolds numbers: (Symbols: experiment [49], lines: present simulation) $\diamond Re = 1.5$, $\circ Re = 4.1$, $\square Re = 11.6$, and $\triangleleft Re = 31.9$. Here $H = \frac{h-0.5D_P}{D_P}$ where h is the height of the sphere center from the bottom wall and D_P is the particle diameter.

Figures 5.11a-b show a comparison of the time evolution of particle settling velocity and position obtained from the numerical simulations with the experimental data [49]. The simulation predictions for both the particle velocity and the particle position show good agreement with the experimental data. The slowing of the particles towards the end of the simulation are to due to the presence of the

bottom wall. Variations in the predicted and experimental data towards the last stages of particle settling are strongly affected by the collision model used.

It should be noted that the Lattice Boltzmann simulations conducted by ten Cate *et al* [49] used a calibration procedure which computes an effective sphere radius from an analytic expression for the drag force at low Reynolds numbers at a given volumetrically averaged fluid velocity. Without this procedure, the velocity of the particle can be up to 20% different from the experimental values [49]. In the present simulations, such calibration or parameter fitting is not attempted. Use of large number of material volumes within the sphere (larger ratio between the background grid and the material volume grid) provides an accurate description of the sphere size and surface.

5.5 Rise of a Buoyant Sphere

The buoyancy induced motion of a particle in an initially quiescent liquid has been the subject of many previous experimental [51], [52] and numerical [53], [54] studies. The problem is often motivated by the need to predict the rise of low density gas bubbles in high density liquid. Predictive models for hydro propulsion systems, gas/solid fluidized beds, and bubbling chemical reactors [14] [20] [11] must be able to accurately predict bubble trajectories, as well as interphase bubble effects on the carrier fluid. Additionally complexity in such systems is added by considering the effects of multiple bubbles, where collision, deformation and coalescence can change the results significantly.

In this case, the rise of a rigid sphere in a viscous liquid is considered. The sphere is released from rest at x_0, y_0, z_0 in an initially stagnant fluid, and rises due to buoyancy forces which are proportional to the difference in density; $\Delta\rho = \rho_f - \rho_p$. The sphere velocity increases to a terminal velocity, V_t , where the buoyancy, pressure, and viscous drag forces are in equilibrium. Two cases are considered: A low density ratio (LDR) case where $\frac{\rho_f}{\rho_p} = 1.25$ and a high density ratio (HDR) case where $\frac{\rho_f}{\rho_p} = 832$. Both the FRS approach and DEM models are used. Relevant simulation parameters for both cases are summarized in table 5.7.

Both the LDR case and HDR cases are important validations for this work. In the LDR case, the momentum imparted to the fluid by the sphere is high, and so two-way coupling is important. By performing the HLE simulation, a dataset may be obtained which can then be used to validate the particle to fluid coupling models

Table 5.7: Computational parameters used in the buoyant sphere case

Case	LDR	HDR
Sphere Diameter [mm]	1.0	0.66 - 1.0
Sphere Density [kg/m^3]	800	1.2
Fluid Density [kg/m^3]	1,000	998
Fluid Viscosity [Pa-s]	0.00033	0.001
Gravity [m/s^2]	9.81	9.81
Δt [s]	5e-4	1.5e-4
x_0, y_0, z_0	0, 0.003, 0	0, 0.003, 0

in the DEM approach. The HDR case is intended to validate both approaches with existing experimental data. Duineveld [52] measured the rise velocity of bubbles in hyper-clean water, over a broad range of his experimental conditions. In his study, for $0.66 < \varnothing_p < 1.0mm$, the bubbles were nearly spherical (small Weber #), and behaved nearly as a rigid bodies. Therefore, his data provides a good reference for validation of both models at high density ratio. While this is routine for a DEM model, a result for rigid body motion using an HLE type model at high density ratios (1,000) has not yet been reported in the literature.

Table 5.8: Computational grids for the buoyant sphere case

Case	LDR-HLE	LDR-DEM	HDR-HLE	HDR-DEM
L_x, L_y, L_z [\varnothing_p]	10, 40, 10	25, 50, 25	10, 50, 10	25, 50, 25
N_x, N_y, N_z	50, 500, 50	25, 50, 25	50, 250, 50	25, 50, 25
$\frac{\varnothing}{\Delta}$ near sphere	20	1	5	0.8
Δ/Δ_m	2	-	4	-

5.5.1 Low Density Ratio

It is important to compare the grids used for the two methods in simulating the low density ratio case. Table 5.8 summarizes the grids used by each method for both the LDR and HDR cases. In figure 5.12a, the low density ratio sphere is resolved by 20 control volumes across its diameter for the HLE approach. The colored region is the area constrained to rigid body motion, and at the colored boundary the no slip condition is enforced. In figure 5.12b, the grid spacing is equal to one sphere diameter ($\Delta_{grid} = \varnothing_{sphere}$) for the sub-grid DEM approach. For this simple case, the HLE approach uses 20^3 or 80,000 times as many grid points for the same sphere size. A future grid refinement study should be conducted to determine at what resolution the HLE approach solution becomes grid independent. For now, a grid with $\Delta_{grid} = \varnothing_{sphere}/20$ is used to assure accuracy.

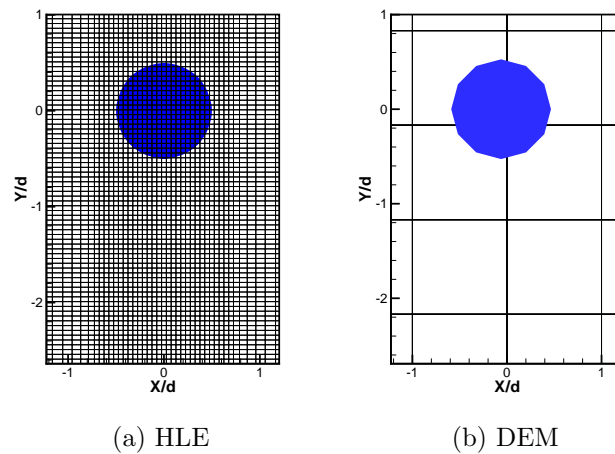


Figure 5.12: Close up of grid surrounding the low density ratio sphere. (a) HLE grid (b) DEM grid

At the low density ratio, the particle time scale, τ_p is used to determine an appropriate simulation time. This can be calculated as follows:

$$\tau_p = \frac{d_p^2}{36\nu} = \frac{0.001^2}{36 \cdot 0.00033} = 0.08 \text{seconds} \quad (5.8)$$

The simulation is allowed to run for $5\tau_p = 0.4$ seconds. The HLE simulation reaches a terminal Reynolds number of 165. Following Clift et al. [55], we can calculate two dimensionless parameters N_U and N_d for the buoyant sphere.

$$N_U = Re/C_d = \frac{165}{1.08} = 153; N_U^{1/3} = 5.35 \quad (5.9)$$

$$N_D = Re^2 \cdot C_d = 165^2 \cdot 1.08 = 29,403; N_D^{1/3} = 30.8 \quad (5.10)$$

The values of $N_U^{1/3}$ and $N_D^{1/3}$ agree well with those shown by Clift et al. [55].

In the DEM model, the standard drag curve [32] is used:

$$C_d = \frac{24}{Re} (1 + 0.15Re_p^{0.687}) \quad (5.11)$$

A comparison of the HLE and DEM results for Reynolds number evolution to terminal velocity is shown in figure 5.13. The HLE model shows a larger initial acceleration than the DEM models, but the two methods are in good agreement for terminal velocity. The deviation of predicted terminal velocity for all simulations is less than 5%, indicating that the drag model is accurate for both passive and non-passive bubbles and particles.

To validate the DEM approaches effect on the fluid, the wake produced with

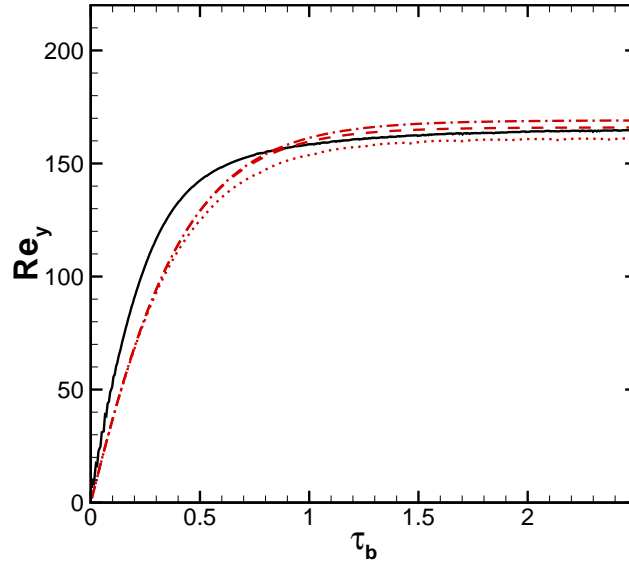


Figure 5.13: Evolution of LDR sphere Reynolds number. HLE (—), DEM: 1-way coupling (- - -), DEM: 2-way coupling (- · -), DEM: volumetric coupling (· · ·)

2-way and volumetric coupling using the DEM approach is compared to the wake produced in the HLE simulation. Recall that in the DEM model, the no slip condition is not explicitly enforced at the sphere surface, as it is in the HLE model. Because of this, the maximum normalized fluid velocity, V/V_p , is much less than 1 for the DEM model, and it does not make sense to compare the maximum wake velocity for the two models. A more appropriate comparison is made in Figure 5.14 which shows the contour lines of $V/V_p = 0.1, 0.2,$ and 0.3 . At these lower velocities, the selected contour lines show that the wake is wider for the DEM approach. This is a result of the interpolation kernel which distributes the Lagrangian particle effects to the Eulerian grid in a smooth manner [29]. Figure 5.15 compares the velocity profiles at different downstream distances in the wake of the rising sphere

for both models. Although the DEM model cannot capture a no-slip interface as in the HLE model, it has a good ability to couple the momentum of the sphere to the surrounding fluid. At a down stream distance of $Y/D > 2$, the streamwise momentum integrated over the width of the wake is quite similar for both models, suggesting that a similar amount of momentum is transferred.

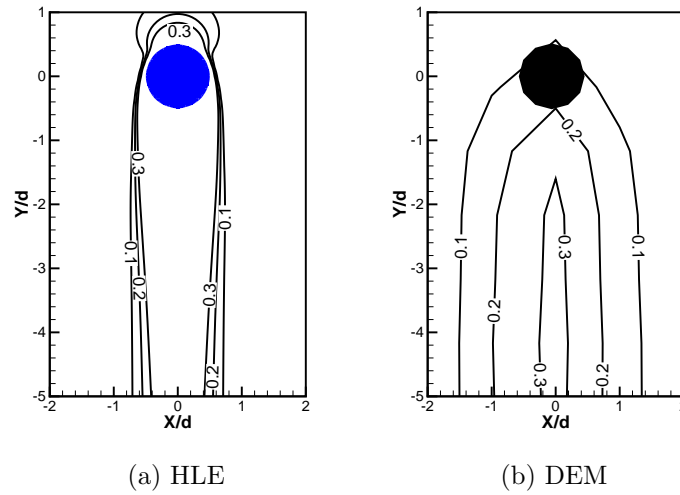


Figure 5.14: Selected isolines of fluid Y velocity normalized by particle Y velocity for (a) HLE result (b) DEM volumetric coupling result

5.5.2 High density ratio

A sphere rising due to buoyancy at a density ratio of 832 was simulated for diameters ranging between 0.66 and 1.0 millimeters. In the HLE approach, a uniform grid was scaled to each sphere size such that there each sphere diameter is resolved by exactly 5 grid points. This results in a grid spacing of between 1.32 and .2

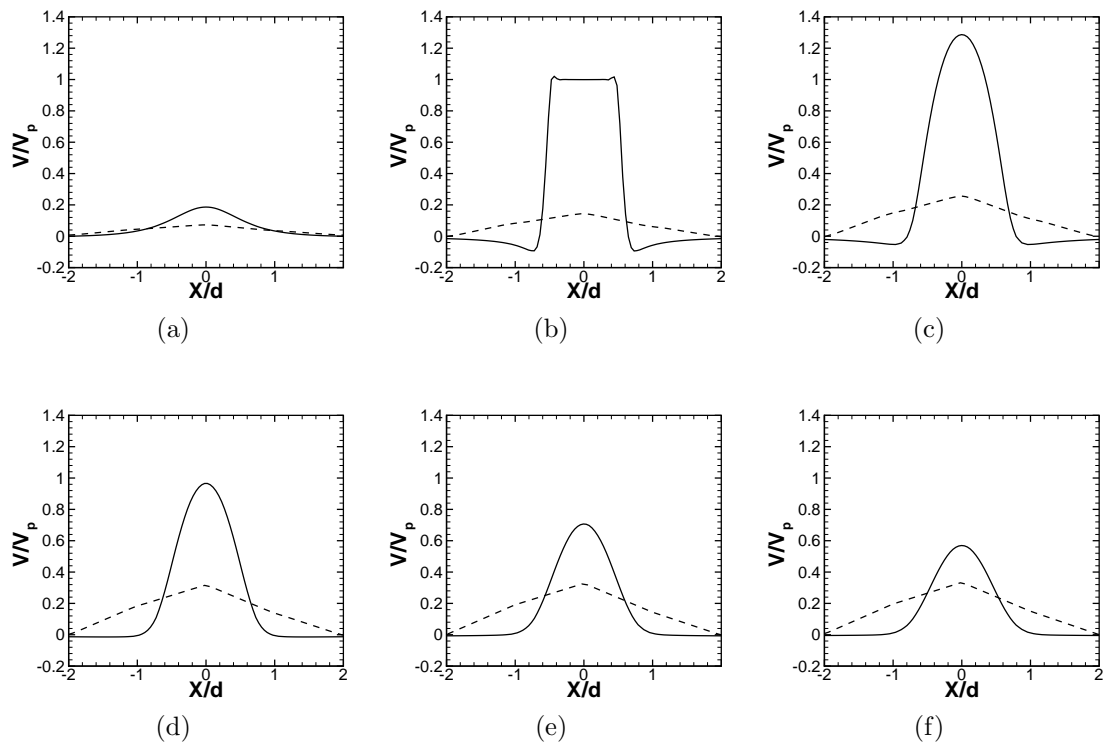


Figure 5.15: Wake velocity profiles at selected upstream and downstream distances from the LDR sphere center. FRS(—) DEM volumetric coupling (- - -) (a) $Y/d = +1$ (b) $Y/d = 0$ (c) $Y/d = -1$ (d) $Y/d = 2$ (e) $Y/d = -3$ (f) $Y/d = -4$

millimeters. As mentioned previously, a more detailed grid refinement study is needed to determine if this is enough to properly resolve the surface shape. However, the goal of this validation case is to show that the HLE approach can be used at density ratios on the order of 1,000 and with a modest grid resolution. In section 6.2, slightly finer grids will be used to simulate complex bubble-vortex interactions at a density ratio of 1,000.

A grid with uniform spacing of 1mm is used for all the DEM simulations, resulting in a resolution of between 1 and 1.5 grid points per sphere diameter. The drag coefficient for air bubbles rising in water has been investigated by many, and in a recent study, Darmana et al. [33] suggest the use of the following correlation based on experimental data:

$$C_d = \max \left[\min \left[\frac{16}{Re} (1 + 0.15 Re^{0.687}), \frac{48}{Re} \right], \frac{8}{3} \frac{Eo}{Eo + 4} \right] \quad (5.12)$$

Here, Eo is the Eötvös number (or Bond number) defined as $Eo = (\rho_f - \rho_p)gd_b^2/\sigma$. This relationship is valid when the restrictions summarized in Table 5.9 are respected. The advantage to this model is that it implicitly accounts for some bubble deformation through the Eotvos number term. For this case, and the vortex cases in sections 6.1 and 6.2, this drag model is a valid alternative to a strictly Reynolds number based model.

Both the HLE and DEM simulations were allowed to run until the rise velocity was stationary (up to 0.5 seconds depending on bubble size). At this point the terminal velocity was taken and compared to the values measured by Duin-

Table 5.9: Drag model restrictions

Restriction	Range	Current Case	Vortex Cases
$Eo = \frac{(\rho_f - \rho_p)gd_b^2}{\sigma}$	$10^{-2} < Eo < 10^3$	0.303	$10^{-2} < Eo < 10^{-1}$
$Mo = \frac{g\mu_i^A(\rho_l - \rho_p)}{\rho_1^2\sigma^3}$	$10^{-14} < Mo < 10^7$	$6 \cdot 10^{-14}$	$10^{-12} < Mo < 2 \cdot 10^{-11}$
$Re_p = \frac{\rho_l(U_p - U_l)d_p}{\mu_l}$	$10^{-3} < Re_p < 10^5$	200	1,000

evel [52]. Figure 5.16 shows the comparison of the DEM and HLE results to the experimental data. The one-way and two-way coupling models result in identical values for terminal rise velocity. This is expected because the overall momentum imparted to the fluid by a single bubble at this density ratio is quite small, and the overall volume fraction is low. In Duineveld’s experiments, great care was taken to assure the water was free of surfactants, and so surface tension effects were small. At the time of publication, the experimental terminal velocities were the highest recorded. It quite is possible that the drag law in equation 5.12 is correlated to ‘dirtier’ bubbles than in the experimental condition which would explain the slower rise velocities. As bubble size is increased, a greater volumetric effect is present, which can explain the departure of the two-way coupling only results above the experimental data. With volumetric coupling, the rate of increase of rise velocity with bubble size is consistent with the experimental data.

The HLE approach also under-predicts the terminal velocity compared to the experimental data, but for different reasons. Because the HLE approach is interpolating a smooth surface onto a finite number of grid points, the method will approach a perfect representation of the surface with increasing grid resolution. Figure 5.17 shows a cross section of the no-slip surface of the sphere generated

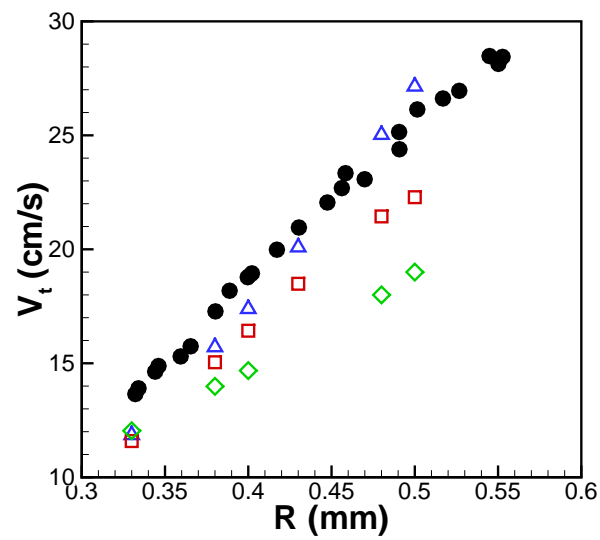


Figure 5.16: Comparison of the HDR results with experimental data: (●) experimental data [52], (△) DEM 2-way coupling, (□) DEM volumetric coupling, (◇) HLE

on grids corresponding to the high resolution LDR case and the low resolution HDR cases. Two issues are noted. First, there is a noticeable difference in surface smoothness. This will result in a significant increase in form drag on a coarser grid. Second, because of the corners in the surface shape, the sphere volume is actually less for the lower grid resolution. Both of these factors will contribute to a lower terminal velocity because of corresponding increase in drag and a decrease in buoyancy force. There is better agreement with the experimental data for smaller Reynolds numbers, where drag due to surface shape has less of an effect.

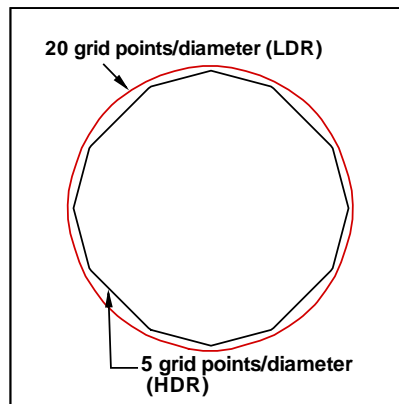


Figure 5.17: Cross section of the sphere shape generated using the LDR and HDR grid resolutions in the FRS approach.

5.6 Three-Dimensional Falling "Blob"

This test case is included to show the applicability of the DEM approach to a flow driven entirely by particle motion. Consider a three dimensional sphere composed of several thousand tightly packed rigid particles. The fluid region containing this particle 'blob' has a uniform initial particle volume fraction, ϕ_0 . Both the local density, ρ_f , and viscosity, μ_f , vary according to this volume fraction. In the high particle number, N_p , limit, the behavior of this particle/fluid system is analogous to a viscous, droplet dissolving in a fluid with which it is miscible. For two such fluids, the surface tension force at the droplet interface vanishes, and the droplet dynamics are governed by viscous and inertial forces. The problem may be described in terms of the density ratio, viscosity ratio, and the blob Reynolds number:

$$\begin{aligned} DR &= \rho_b \rho_f \\ VR &= \mu_b / \mu_f \\ Re_b &= \frac{\rho_f U_d D_b}{\mu_f} \end{aligned}$$

Throughout this section the subscript 'b' will be used to denote a value associated with the blob or droplet, while the subscript 'f' will denote a value associated with the carrier fluid. Mitts et al. [1] used the miscible fluid analogy to study the dynamics of deformation and breakup of droplets in the supercritical regime. Supercritical conditions are present in many rocket engines, where high tempera-

tures and pressures are required, and many questions remain about the behavior of the fuel-air mixture. They were able to classify the miscible droplet behavior into several sub-regimes based on the viscosity ratio and droplet Reynolds number for density ratios near unity. In a computational study, Walther & Koumoutsakos (W&K) [30] used adaptive vortex methods and Lagrangian particle tracking to model several of these sub-regimes, including the multi-mode bag vortex ring sub-regime, which will be the focus of this validation case. In their work, they characterized the speed of a falling blob of particles using the Hadamard and Rybczyński (H-R) formula for the speed of a viscous, spherical drop descending under the force of gravity :

$$U = U_{HR} = \frac{(\rho_d - \rho)gD^2}{12\mu} \frac{\mu + \mu_d}{\mu + \frac{3}{2}\mu_d} \quad (5.13)$$

We consider a similar modeling approach here, and arrange 97,233 solid particles into a spherical shape in an initially quiescent fluid. The particles are heavier than the liquid, and fall under the influence of gravity. The local viscosity of the fluid is varied at the grid faces:

$$\mu = \mu_f + \Theta_p(\mu_p - \mu_f) \quad (5.14)$$

where Θ_p is the particle volume fraction of the associated control volumes. When volumetric coupling is considered, recall that the local density is given by:

$$\rho = \rho_f(1 - \Theta_p) \quad (5.15)$$

The initial volume fraction is obtained from the following expression derived by Lundgren [56] for high volume fractions:

$$\frac{\mu_b}{\mu_f} \approx \frac{1}{1 - \frac{5}{2}\Theta_{p0}} \quad (5.16)$$

The computational parameters were selected so that comparisons could be made with both experimental and numerical studies of the bag vortex ring sub-regime. The characteristic velocity, U , is defined using the H-R formula (equation 5.13). In doing so, the problem can be specified completely by assigning the density ratio, viscosity ratio, Reynolds number, and Froude number. For clarity, all parameters used in the setup of this case are summarized in table 5.10. Note that the particle density is greater than the blob density due to the initial volume fraction which is less than unity (see eqn 5.15).

Three different DEM models are considered and are summarized in table 5.11. Model 1 is intended to be similar to the one used by W&K. Here, the particle motion is affected only by gravity, and drag forces, and the particle to fluid momentum coupling is a result of the drag force only. The fluid density is constant everywhere. In model 2, the added mass force, lift force, and pressure force are also considered in the particle equation of motion, and the momentum coupling to the fluid includes these additional terms. In model 3, the variable density, volumetric coupling model is used, and the fluid density, ρ_f , varies according to equation 5.15. In order to be able to isolate the isolate the variable density effects, model 3 is otherwise identical to model 2. In all models, the inter-particle collision force is

Table 5.10: Parameters used for the setup of the three dimensional falling "blob"

Parameter	Value
ϕ_b	100 mm
ϕ_p	1.572 mm
N_p	97,233
g	9.81 m/s^2
ϕ_0	0.388
μ_b/μ_f	35.0
μ_f	0.001 pa-s
ρ_b/ρ_f	1.6
ρ_f	1.0 kg/m^3
ρ_p	2.544 kg/m^3
Re	330
Fr	3.332
Domain Size	$10D_b \times 10D_b \times 10D_b$
Grid Size	64 x 64 x 64

neglected.

The speed of the center of gravity of the descending blob is shown in figure 5.18. In the present case, the peak blob Reynolds number based on blob velocity and initial diameter is 40 for models 1 & 2 and 46 for model 3. For the present viscosity ratio of 35, this puts the results within the bag vortex sub-regime observed by Mitts et al. and simulated by W&K. The blob speed over the time simulated is nearly the same for models 1 and 2, showing that the net effect of lift, added mass and pressure forces is negligible for this case. Further, this shows that the increase in blob velocity shown by model 3 is due entirely to variable density effects. The blob accelerates to a peak non-dimensional velocity of $0.12U_{HR}$ for models 1 & 2 and $0.14U_{HR}$ for model 3 at a non-dimensional time of about 27. Figure 5.19 compares

Table 5.11: Comparison of the 3 present DEM models and the model used by Walther & Koumoutsakos in the falling blob case

Model	F_G	F_D	F_L	F_{AM}	F_P	Variable Density	Particle Collision
W&K[30]	Yes	Yes	No	No	No	No	No
Model 1	Yes	Yes	No	No	No	No	No
Model 2	Yes	Yes	Yes	Yes	Yes	No	No
Model 3	Yes	Yes	Yes	Yes	Yes	Yes	No

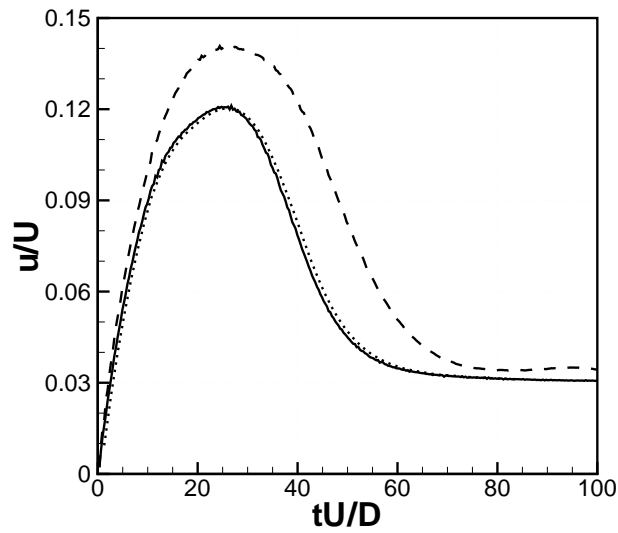


Figure 5.18: Blob speed non-dimensionalized by the H-R velocity as a function of non dimensional time (—)Model 1, (\cdots)Model 2, (- - -)Model 3.

cross sections of the blob at different non-dimensional times throughout this period of initial acceleration for each DEM model. Also shown are the results of W&K at lower Reynolds and Froude numbers. During this time, the blob deforms into a spherical cap shape as the particles in the center of the blob descend faster than the ones on the edge. This is due to viscous action at the edge of the blob which causes the roll-up of a vortex ring around the blob. The ring travels with the blob and causes continued spreading in plane normal to the falling direction.

The differences in blob shape during the acceleration to peak velocity can be explained by the variable density effects of model 3. With volumetric coupling considered, the fluid density in the blob region is lowered in proportion to the particle volume fraction. This results in a low pressure region which follows the blob centroid and helps to accelerate the fluid *with* the blob. The blob deforms to a spherical cap shape rapidly in models 1 & 2 because the particles on the bottom of the blob do the work of pushing the initially quiescent fluid out of the way, while the particles on the top accelerate. The variable density in model 3 delays this effect by creating a pressure source of momentum in the regions of high particle volume fraction. This causes the fluid around the blob to accelerate in a more uniform fashion, and delays the onset of the spherical cap shape which eventually slows the blob.

At later times, the blob spreads and forms a bag vortex ring which travels with the blob. The circulation of this ring is shown with streamlines in a cross section of the domain in figure 5.20. Once the ring is spread sufficiently wide ($tU/D > 60$), the net variable density effects are decreased, and the blob velocity for model 3

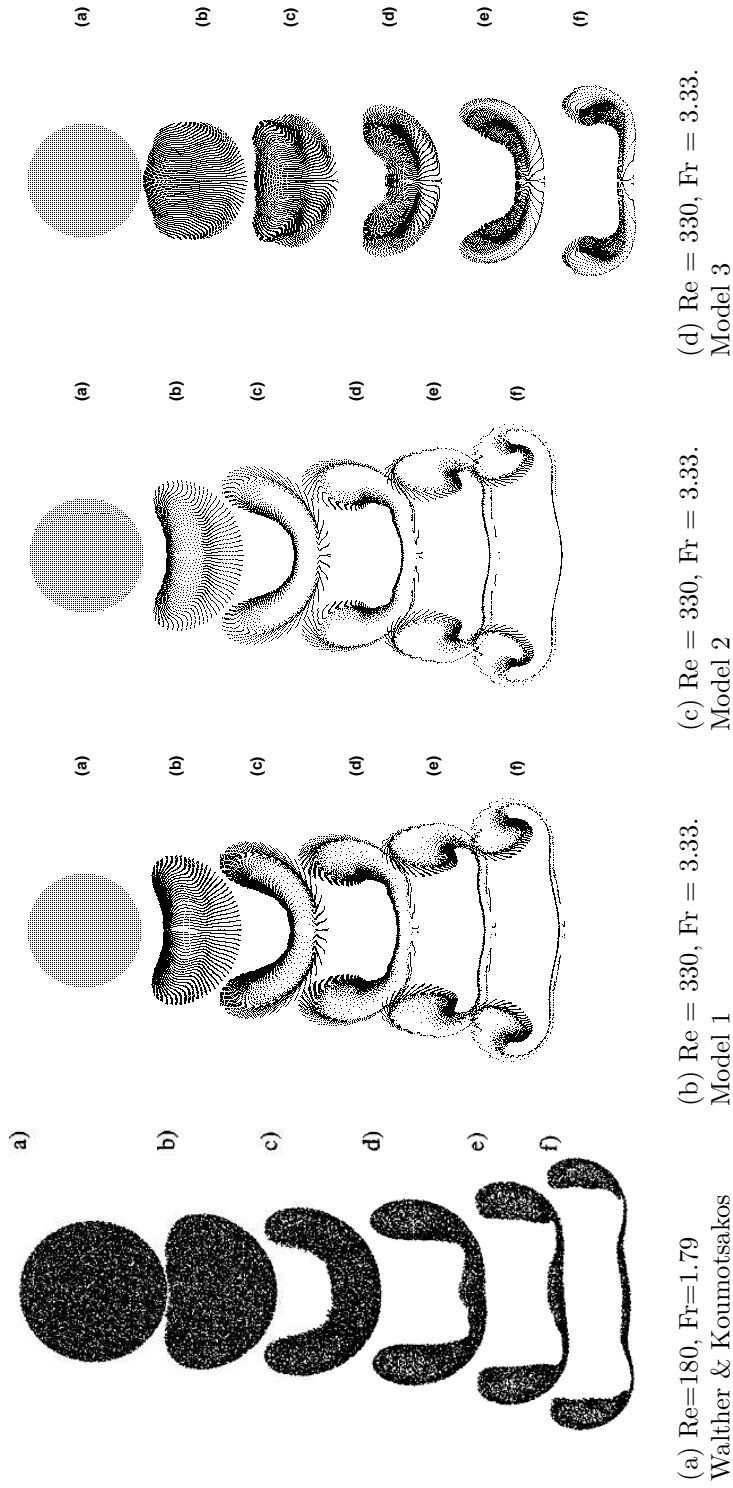


Figure 5.19: Cross section of falling blobs with $\rho_b/\rho = 1.6$ and $\mu_b/\mu = 35$ at different non dimensional times (tU/D) = (a) 0.00, (b) 7.18, (c) 10.77, (d) 14.36, (e) 17.94, (f) 21.53. [Left] Vortex method simulation of Walther & Koumoutsakos [30] at $Re = 180$ & $Fr = 1.79$. [Center & Right] Present results of model 1,2,& 3 at $Re = 330, Fr = 3.33$.

approaches that of models 1 & 2.

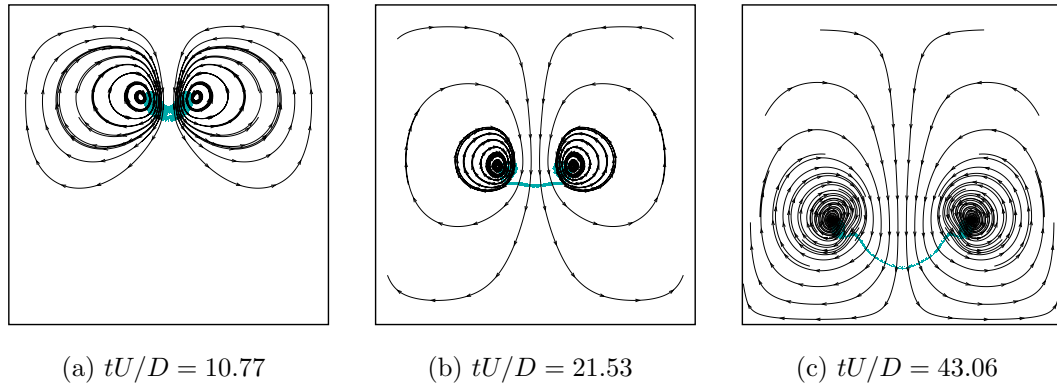
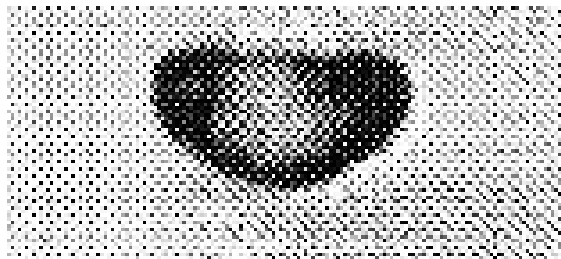
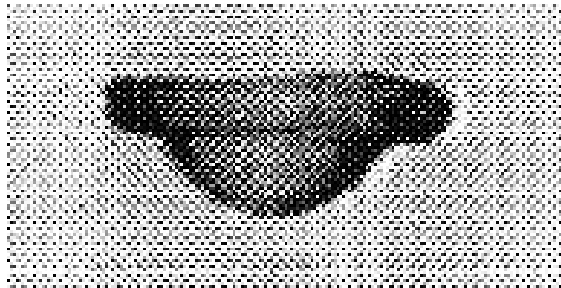
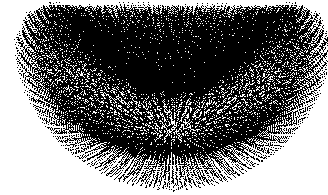


Figure 5.20: Evolution of the bag vortex ring generated by the falling blob. Stream traces are shown at the same domain cross section as in figure 5.19

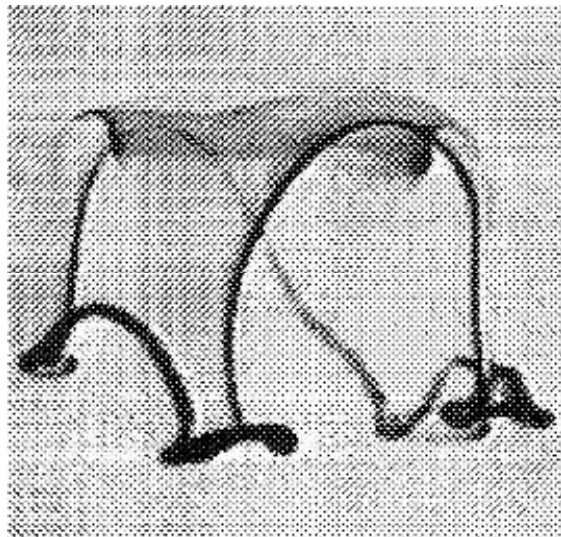
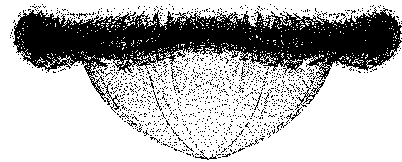
The current results are compared to the experimental results of Mitts et al. in figure 5.21. The current models are clearly able to capture various stages of the droplet deformation and breakup. After the peak velocity is reached, the blob continues to expand into an unstable ring like shape. The particles collect in the high-shear regions on the downward velocity side of the vortex ring, and drive the circulation of the ring (figure 5.21b & figure 5.20). At still later times, the ring becomes unstable, and the particles cluster into four regions of high volume fraction (figure 5.21c). These clusters accelerate as the original blob did, and form four new vortex rings. The initial deformation, the bag vortex ring roll up, instability, and subsequent droplet splitting are all predicted and show good levels of similarity with the experimental images. The development of this instability is similar for both model 3 (volumetric coupling) and model 2 (2 way coupling). The difference is that the onset is delayed in model 3 due to the variable density effects.



(a) Initial Deformation



(b) Bag Vortex Ring Roll-Up



(c) Droplet Splitting

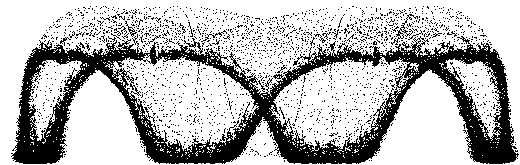


Figure 5.21: Comparison of the present results with the experimental results of Mitts et al. [1] for the bag vortex ring sub-regime of the multi-mode breakup category.

Chapter 6 – Bubble-Vortex Interactions

In this chapter, two cases of bubble-vortex interaction are considered. First, the DEM model is used to simulate the entrainment of eight small bubbles into a two dimensional, traveling vortex tube. Once entrained, the subsequent bubble-vortex interactions are of primary interest. The study of these interactions is motivated in a broad sense by the need to understand the behavior of microbubbles in the wake of moving bodies for the design and operation of marine propellers and turbomachinery components. The entrainment of bubbles in vortex rings has been studied experimentally by Sridhar and Katz (S&K) [25] [12], and this study is arranged so that a comparison may be made to their work.

Next, the Gaussian vortex model (also known as the Lamb-Oseen vortex) is considered as an alternative to the jet-generated vortex tube. This vortex is frequently used as a model of for wingtip vortices, and was used previously by Oweis et al. [13] in a computational study of cavitating bubble capture. This case is attractive because it is readily adapted to both the DEM and HLE grid requirements. The vortex can be stationary or, with proper enforcement of boundary conditions, can be made to translate at constant velocity. Direct comparisons of the the two methods are made, and the underlying mechanisms of vortex distortion are examined

6.1 Bubble Interactions With a Traveling Vortex Tube

6.1.1 Vortex Tube Generation

The domain considered is shown in Figure 6.1. There is an inflow boundary at the left wall, an outflow condition at the right boundary, and walls on the top and bottom. The total domain size is $X/h_{jet} = 10$ by $Y/h_{jet} = 3$ and is centered at $Y/h_{jet} = 0$. The inlet is modeled as an orifice rather than the piston/nozzle assembly used in the experiment. It was shown by James & Madina [57] in a study of vortex ring formation that the difference between the two inlet types for laminar vortex rings is small. At the inlet boundary, a jet is pulsed for 0.27 seconds into the initially quiescent domain, which causes the roll up of two symmetric vortex tubes. The inflow velocity is a function of time, and is described by a polynomial of the form:

$$U(t) = a \cdot t^6 + b \cdot t^5 + c \cdot t^4 + d \cdot t^3 + e \cdot t^2 + f \cdot t + g \quad (6.1)$$

where the 7 constants (a:g) have values summarized in table 6.1. The initial circulation of the vortex tube can be calculated from the inlet velocity profile as

$$\Gamma_0 = \int_0^T \frac{U_0^2(t)}{2} dt = 159 cm^2/s. \quad (6.2)$$

Table 6.1: Values of constants used for the inlet velocity profile

Constant	Value
a	62,278
b	-47,082
c	13,686
d	-2,062
e	159.5
f	-1.289
g	0.006

The vortex Reynolds number based on the cylindrical slug model of Glezer [58] is

$$Re_{vx} = \frac{1}{2\nu} \int_0^T U_0^2(t) dt = 15,879 \quad (6.3)$$

The present inlet velocity pulse is compared to the profile used by (S&K) in figure 6.2. The shape of experimental pulse is well represented by the polynomial function, and the vortex tube generated is comparable in size and strength to the experimental vortex rings. The strength of the vortex is $\Gamma_0/\nu = 15,880$. Glezer [58] characterized the transition from laminar to turbulent vortex rings based on the ring strength and generator piston aspect ratio (L_p/D_p). The the 3D vortex ring corresponding to the present vortex tube exceeds the turbulent transition line for the piston stroke aspect ratio used by S&K. Indeed, the present 2D vortex tube shows some turbulent characteristics during the roll-up and stabilization phases, but in two dimensions it remains stable and laminar as it travels downstream.

To reduce computational expense, a plane of symmetry is assumed at $Y = 0$,

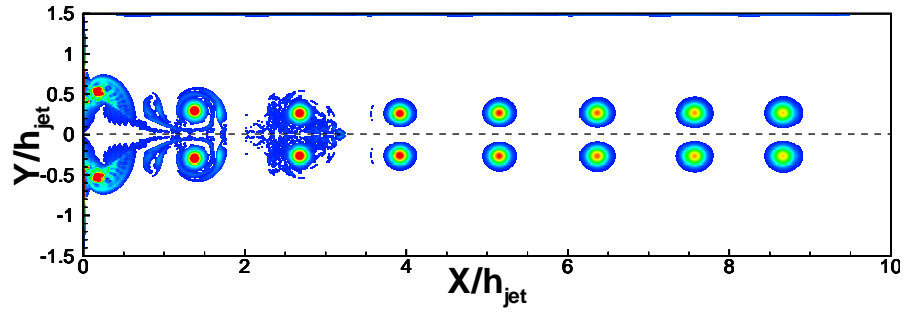


Figure 6.1: The two-dimensional computational domain. Two, symmetric vortex tubes are created by an inlet jet pulsed at $X=0$. Contours show vorticity out of the plane during vortex roll-up and advection downstream. All Subsequent results presented assume a plane of symmetry at $Y=0$, indicated by - - -.

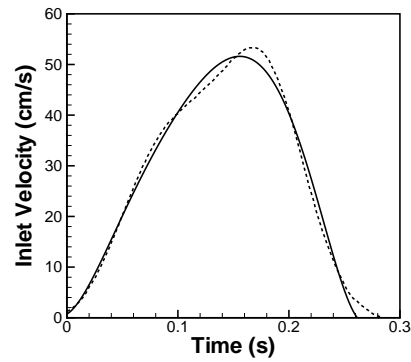


Figure 6.2: Prescribed inlet velocity (—), based on (S&K) [12] (---)

where a free slip condition is imposed ($\frac{\partial u}{\partial n} = 0$), and only the bottom vortex tube shown in figure 6.1 is considered. A uniform cartesian grid is used throughout the area below the line of symmetry with a total of 800 x 121 elements in the X and Y directions. The two-dimensional domain is periodic and uses 4 grid points in the Z direction. This results in a grid spacing of $\frac{h_{jet}}{\Delta} = 80$. Once stable, the vortex core diameter is resolved by approximately 20 grid points. Computational parameters relevant to the domain and vortex generation are summarized in table 6.2

Table 6.2: Computational parameters used in the vortex tube case

Parameter	Value
ρ_f	1,000 kg/m^3
ν_f	1e-6 m^2/s
Domain Size	1m x 0.15 m x 0.005m (below line of symmetry)
Grid Size	800 x 121 x 4
Jet height (h_{jet})	0.1 m
Inflow time	0.27 s
Inflow Velocity	equation 6.1

After the half jet is pulsed, it rolls up into a single vortex tube and travels downstream. After roll up and stabilization of the shear layer, the vortex core moves with a convective velocity of 7 cm/s, which is approximately 14% of the maximum inlet velocity. The contours in figure 6.1 show the diffusion of the high vorticity in the core as the vortex tube travels downstream. Downstream measurements of circulation are made by first determining the center and radius of the vortex core. At each timestep, the core center is located by determining the

centroid of vorticity, defined as (following S&K):

$$X_c = \frac{\sum_i X_i \omega_i^2}{\sum_i \omega_i^2} \quad Y_c = \frac{\sum_i Y_i \omega_i^2}{\sum_i \omega_i^2} \quad (6.4)$$

where ω_i is the local vorticity at the coordinates (X_i, Y_i) . The evolution of the computed centroid is shown in figure 6.3. Oscillations in the Y direction stabilize after $X/h_{jet} = 2$, once the vortex has rolled up completely. The core remains almost circular in shape, and the center travels along the line $Y/h_{jet} = -0.27$. In [25] and [12], S&K have assumed a constant core radius. A variable radius is used in this study, to account for bubble-vortex interactions which may change the core size. The instantaneous core radius is taken to be the average radius at which the value of vorticity is between 10% and 20% of the maximum core vorticity. As the vortex travels downstream, the high vorticity in the center diffuses, and the measured core radius increases slightly. At a downstream distance of $X/h_{jet} = 5$, the radius of the vortex is measured as 1.42 cm. The instantaneous circulation is found by integrating the vorticity over the core area.

$$\Gamma = \int_{core} \omega da \quad (6.5)$$

As the magnitude of vorticity dissipates, the core radius grows and the calculated circulation stays nearly constant. Using the variable radius calculation, the circulation is measured to be $\Gamma = 222\text{cm/s}$ at a downstream location of $x/h_{jet} = 5$, which is 39.6% higher than Γ_0 . Three experimental studies of vortex rings [12], [58], and [59] observed the circulation to be approximately 35% higher than the

initial circulation at the same downstream distance. The two dimensionality of the present simulation makes a direct comparison to the three dimensional vortex ring impossible. However, the similar evolution of vortex strength indicates that the two dimensional vortex tube is a reasonable approximation to a cross section of the three dimensional vortex ring.

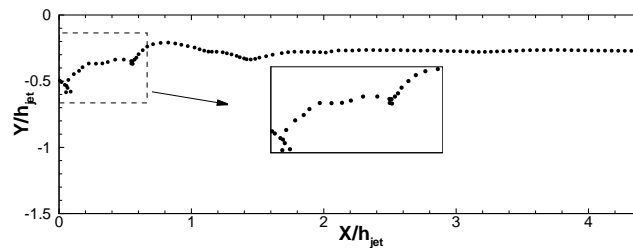
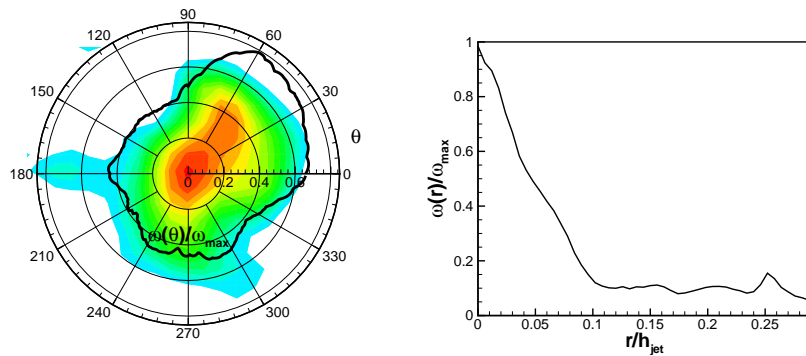


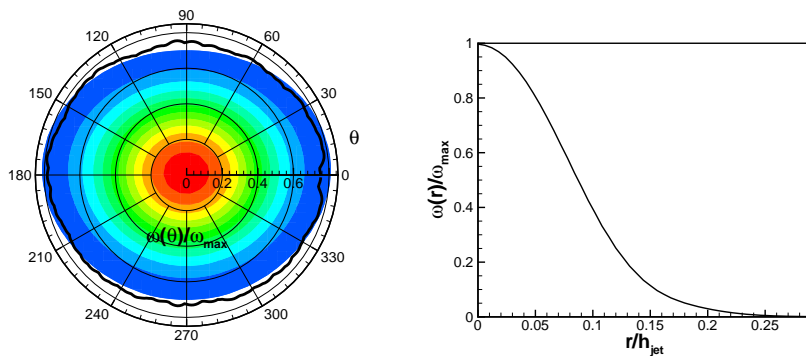
Figure 6.3: Vortex core trajectory. Tracked by following center of vorticity

The instantaneous shape of the vortex core may be determined by creating a map of the vorticity distribution around the vortex center. This will later be used to quantify the vortex distortion caused by the entrained bubbles in section 6.1.3. At each timestep the vorticity distribution in the vortex core is mapped onto an inertial, cylindrical coordinate system which moves with the vortex center (X_c, Y_c) . This is done by discrete averaging over each grid point within the core radius. Figure 6.4 shows the results of this mapping applied to the initial stage of vortex formation at $X/h_{jet} = 0.04$, and the fully developed stage $X/h_{jet} = 0.5$. In the initial stage, the angular vorticity mapping (a) does a good job of capturing the irregular shape of the core. The radial vorticity distribution (b) shows that there is a high gradient of vorticity in the radial direction, that has yet to diffuse. At much later times, the vortex core is stable and the core is quite close to an oval

in shape (c). Again, the angular mapping scheme captures this accurately. The radial distribution (d) shows that the core has approached a Gaussian distribution of vorticity. As the vortex travels downstream. This Gaussian distribution is shown for three X locations in figure 6.5. The vorticity diffuses from the core center as time increases, but the normalized curve $\omega(r)/\omega_{max}(r)$ stays nearly constant.



(a) Initially non uniform core during vortex roll-up



(b) Fully developed, Gaussian core at $X/h_{jet} = 5$

Figure 6.4: Discrete mapping of the vortex core shape into a cylindrical reference frame which moves with the core. Left hand figures (a & c) are contours of vorticity overlaid with the angular vorticity distribution. Right hand figures (b & d) are the radial vorticity distributions.

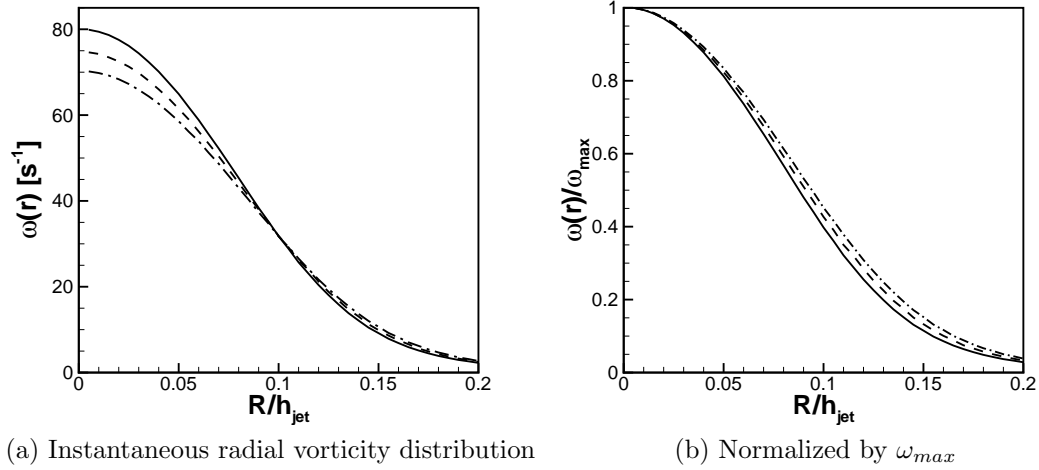


Figure 6.5: Evolution of the instantaneous radial vorticity distribution within the core. (—) $X/h_{jet} = 0.5$, (---) $X/h_{jet} = 0.6$, (- · -) $X/h_{jet} = 0.7$

6.1.2 Bubble Injection

At a value of $X/h_{jet} = 5.0$, eight bubbles are injected below and in front of the vortex core. One bubble at a time is injected, with a time of $\Delta t_{inj} = 10ms$ between each bubble. Due to buoyancy, the bubbles rise and are entrained into the vortex core. The injection point is varied so that the vortex tube encounters a rising line of bubbles as in [12]. This is illustrated in figure 6.6. Despite unique release points and times, the bubbles all reach the same settling radius after circling the vortex core. A parametric study is performed to determine the effects of bubble buoyancy force on bubble settling location and vortex tube distortion. The bubble diameter ($2 \cdot R_b$) and gravitational acceleration (g) are varied over a broad range in 17 individual cases, so that comparisons may be made to the experimental results

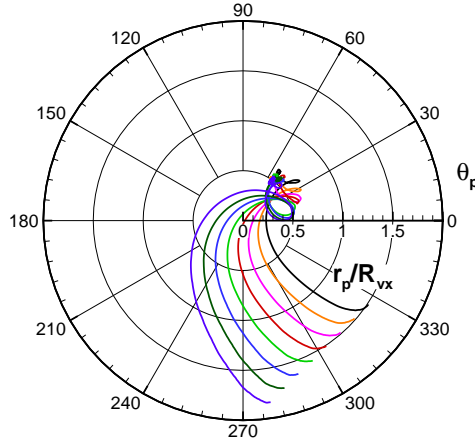


Figure 6.6: Release points and trajectories of the eight bubbles in the moving, cylindrical reference frame.

of S&K. The non-dimensional parameter ga^3/Γ_0^2 ranges from $1.3\text{e-}7$ to $5.4\text{e-}6$. The bubble stokes number, defined as $St_b = \frac{\omega d_b^2}{36\nu}$, where $\omega = \Gamma_0/2\pi r$ has values between 0.014 and 0.264. The initial vortex tube strength and the bubble injection locations remain constant for all cases.

6.1.3 Results

Table 6.3 summarizes the key parameters of each case, and some important results. Each case is simulated using the DEM model with one-way, two-way and volumetric coupling. For brevity, only the bubble settling radius from the volumetric coupling results is tabulated. This distance is normalized by both the average vortex radius, R_{vx} as well as the inlet jet height, h_{jet} . Also, the relative vortex distortion caused by the presence of the bubbles is indicated for each case. The instantaneous distortion

is measured as the percent difference from the mapping (radial & angular) of vorticity in an undistorted vortex core. The distortion is time averaged over a period of 1 second after the bubbles are entrained. Vortex cores with both the average radial and angular distortion less than 8% are considered *undistorted*. Vortex cores with average radial or angular distortion above 20% are considered *significantly distorted*. All cores falling in between these two criteria are considered *marginally distorted*. The overall trends in the results will now be discussed by examining some particular cases in detail.

Table 6.3: Computed settling location and observed vortex distortion for each case (volumetric coupling results)

Case	(\varnothing_b)	g	$St_b = \frac{\omega \varnothing_b^2}{36\nu}$	$\frac{gR_b^3}{\Gamma_0^2}$	r/R_{vx}	r/h_{jet}	Distortion
#1	300 μm	9.81 m/s^2	0.014	1.31e-7	0.12	0.019	none
#2	500 μm	9.81 m/s^2	0.039	6.08e-7	0.26	0.038	none
#3	600 μm	3.0 m/s^2	0.056	3.21e-7	0.16	0.023	none
#4	600 μm	4.0 m/s^2	0.056	4.28e-7	0.18	0.027	none
#5	600 μm	9.81 m/s^2	0.056	1.05e-6	0.40	0.058	none
#6	700 μm	9.81 m/s^2	0.076	1.67e-6	0.54	0.078	none
#7	900 μm	3.0 m/s^2	0.126	1.08e-6	0.25	0.037	none
#8	1,000 μm	4.0 m/s^2	0.156	1.98e-6	0.36	0.052	none
#9	1,000 μm	6.0 m/s^2	0.156	2.97e-6	0.51	0.073	marginal
#10	1,100 μm	0.5 m/s^2	0.189	3.30e-7	0.08	0.011	none
#11	1,100 μm	4.0 m/s^2	0.189	2.63e-6	0.17	0.025	none
#12	1,200 μm	2.0 m/s^2	0.225	1.71e-6	0.24	0.034	marginal
#13	1,200 μm	5.0 m/s^2	0.225	4.28e-6	0.51	0.068	significant
#14	1,300 μm	0.14 m/s^2	0.264	1.52e-7	0.09	0.013	marginal
#15	1,300 μm	1.2 m/s^2	0.264	1.3e-6	0.13	0.019	marginal
#16	1,300 μm	3.0 m/s^2	0.264	3.27e-6	0.35	0.047	significant
#17	1,300 μm	5.0 m/s^2	0.264	5.4e-6	0.54	0.070	significant

Bubble Trajectory and Settling location In all cases, each of the eight bubbles are entrained by the passing vortex tube. They rise from their release point around the rear of the vortex and are swept into the downward velocity region on the forward side of the core. depending on the Stokes number and buoyancy force acting, the bubbles may circle the core multiple times before ultimately reaching their final settling location, where their average motion in the inertial reference frame is zero. Figure 6.7 shows the effect of bubble size on the entrainment trajectory of bubbles in cases 1, 2, and 5. Gravity is constant at $9.81m/s^2$ for each of these cases. In case #1, the bubble Stokes number is very small, and the bubble follows the fluid streamlines closely as it spirals towards the core. In cases #2 and #5, the Stokes number is increased, and a corresponding increase in buoyancy force results in a more direct path to the settling location. The settling radius increases with increasing bubble size which is consistent with the S&K observations. Several authors [26] [27] [24] have shown both experimentally and numerically the preferential settling of bubbles in the downward velocity regions of rotating flow. Mazzitelli et al. [26] argued that this is primarily a consequence of the lift force which pushes the rising bubble to this region. Further examination of the lift force and effects of lift coefficient are needed to properly quantify its effect in this particular case.

Figure 6.8 shows the effects of bubble-fluid coupling on the entrainment trajectories of bubbles for cases #8, #12, and #17. These three cases are cases in which use of the volumetric coupling model results in very slight distortion, marginal distortion, and significant distortion respectively. In all three cases, there is very

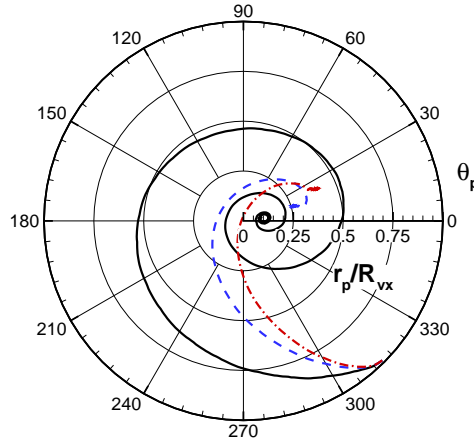


Figure 6.7: Entrainment and settling trajectory for three different bubble sizes with $g = 9.81m/s^2$. (—) $\varnothing_b = 300\mu m$, (---) $\varnothing_b = 500\mu m$, (- · -) $\varnothing_b = 600\mu m$

little variation between the 1-way and 2-way coupling trajectories. This indicates that the overall momentum imparted to the fluid because of the bubble surface forces is small for the bubble sizes studied. The paths of the bubbles with volumetric coupling initially follow a larger radius than the 1-way and 2-way bubbles, but tend to accelerate towards the core faster once the local fluid velocity shifts direction. This difference is a result of the low pressure region which follows the bubble in the variable density, volumetric coupling formulation. When the associated pressure gradient aligns with the mean pressure gradient of the vortex, the result is a faster acceleration towards the center. This bubble induced pressure gradient is also responsible for creating flow unsteadiness in the core, and is the main cause of the significant vortex distortion observed in case #17.

Once the bubbles are entrained, they reach an equilibrium position in the core referred to as the settling location. They do not remain perfectly stationary

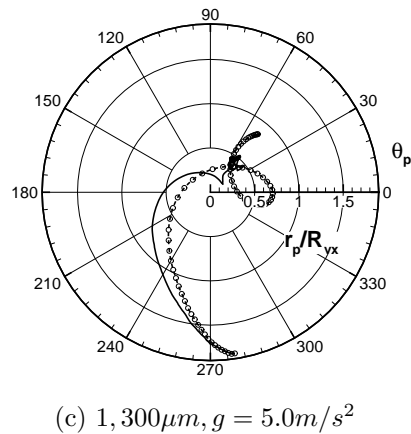
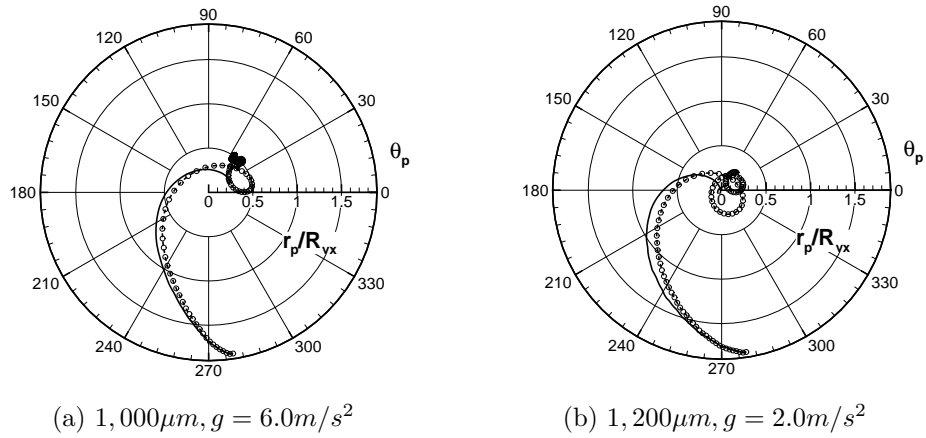


Figure 6.8: Bubble trajectory shown in the moving reference frame for three cases. (a) No vortex distortion, (b) Marginal vortex distortion, and (c) Significant vortex distortion. (—) Volumetric coupling, (---) 2-way coupling, (ooo) 1-way coupling

because of local variations in pressure and bubble collision forces. In the mean, however, their position is steady. The non-dimensional location, r/R_{vx} is averaged over all particles and spatially, over a distance of $5.2X/h_{jet} < X_{vx} < 5.9X/h_{jet}$. This corresponds to an averaging time of almost 1 second, which is similar to the amount of time that S&K used to collect their data. Following S&K, the settling location is plotted Vs. the non-dimensional parameter gR_b^3/Γ_0^2 in figure 6.9 for each coupling model alongside the experimental data. There is some spread in the data, but overall, the trends are consistent with the experiment. Some of this spread may be attributed to the following factors: First, although the 2D vortex tube has been shown to be a valid approximation to a cross section of the vortex ring in terms of vortex strength, there are most certainly three dimensional characteristics which are not captured in this work. An interesting future study would consider the three dimensional effects. Next, the normalization of settling location takes into account the measured radius of the vortex, rather than a constant radius as was assumed by S&K. The [resent settling locations are also tabulated using constant normalization by h_{jet} for future comparison. Finally, an additional independent variable, g , has been introduced to facillitate the simulation of a broader range of bubble sizes with the same initial condition. S&K sampled their parameter space by varying the strength (Γ) of their vortex rings while gravitational acceleration was a constant.

There is not much variation in settling location because of coupling model. As indicated in the entrainment trajectories, there is no difference between one-way coupling and two-way coupling in terms of settling location. With volumetric

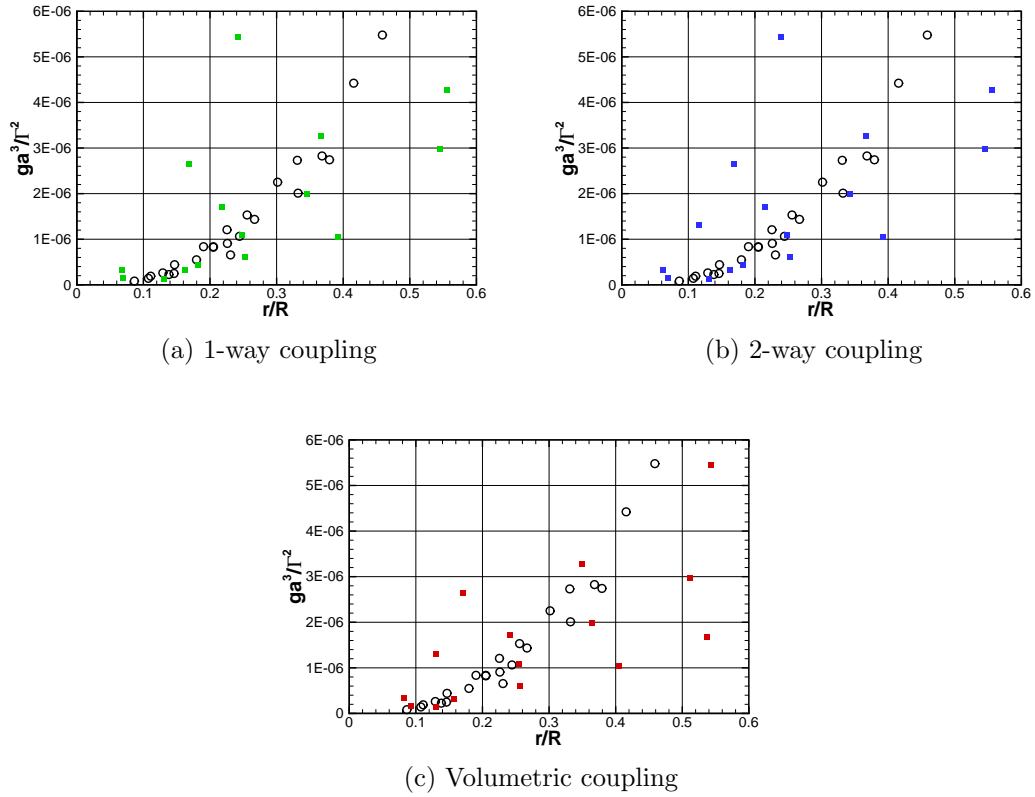


Figure 6.9: Comparison of the non-dimensional settling location with the experimental results of Sridhar & Katz. The parameter ga^3/Γ^2 is the non-dimensional ratio of the buoyancy force and the hydrodynamic pressure gradient experienced by the bubble. (\circ) Experimental data, (\blacksquare) present results.

coupling, a slight increase in settling radius is observed for most bubbles, but this cannot be considered a rule. A typical increase is on the order of 5%.

Vortex Distortion The vortex cores of case #8, #12, and #17 are visualized in figures 6.10, 6.11, and 6.12, at the same instant in time, 200 ms after bubble injection. Figure 6.10 shows the contours of vorticity compared to an undisturbed vortex at the same time instant with no bubbles entrained (figure 6.10a). Figure 6.11 shows the radial distribution of vorticity in each core compared to the vortex core with no bubbles entrained (figure 6.11a). Finally, figure 6.12 shows the angular distribution of vorticity for each case compared to the case with no bubbles entrained (figure 6.12a). In the undistorted core, the contours of vorticity are symmetric about the $\theta = 0^\circ$ and $\theta = 90^\circ$ planes. The radial distribution of vorticity is similar to a Gaussian curve, and the angular vorticity distribution shows the slight elongation in the flow direction. The vortex core from case #8 with very slight bubble induced distortion is shown in figures 6.10b, 6.11b, and 6.12b. The bubbles are grouped tightly together (6.10b), and have caused a slight decrease in vorticity at the vortex center (6.11b). This is a result of decreased vorticity in the region near the bubbles at $\theta = 45^\circ$ (6.12b). Further disturbance is observed in case #12 and shown in figures 6.10c, 6.11c, and 6.12c. The bubbles have caused a 'C' shaped region to develop in the inner core (6.10c), and the radius of maximum vorticity is shifted away from the center (6.11c). Qualitatively, this is very similar to the effects observed by Ferrante & Elghobashi in microbubble laden Taylor-Green vortex flow. The original shape of the outer region is mostly retained, though there

is a noticeable drop in vorticity at all angles (6.12c). A significantly distorted vortex from case #17 is shown in figures 6.10d, 6.11d, and 6.12d. The bubbles have created three distinct higher regions of high vorticity in inner core (6.10d). The disturbances propagate to the outer core, where they interact with regions of low vorticity. The Gaussian profile of radial vorticity is no longer present (6.11d), and a peak in vorticity is observed near the bubble settling radius. The mechanism of this high vorticity band will be investigated further in section 6.2. The average shape of the vortex is quite irregular (6.12d), due to the fragmenting of the inner core.

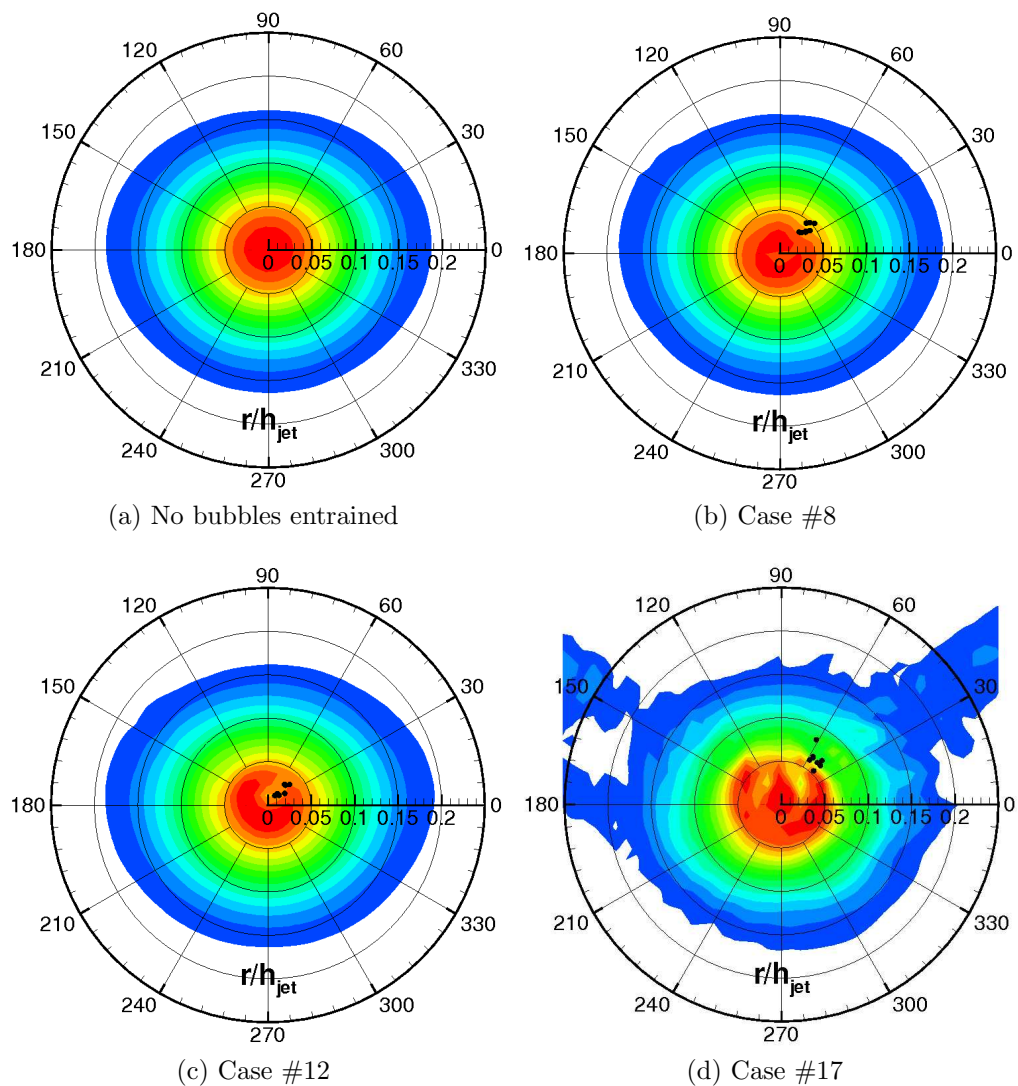


Figure 6.10: Vortex distortion by the presence of bubbles shown by core vorticity contours. (a) A vortex with no bubbles entrained, (b) an undistorted vortex, (c) a marginally distorted vortex, and (d) a significantly distorted vortex. Volumetric and 2-way coupling are considered in all cases. Contours range from 5 to 75 s^{-1}

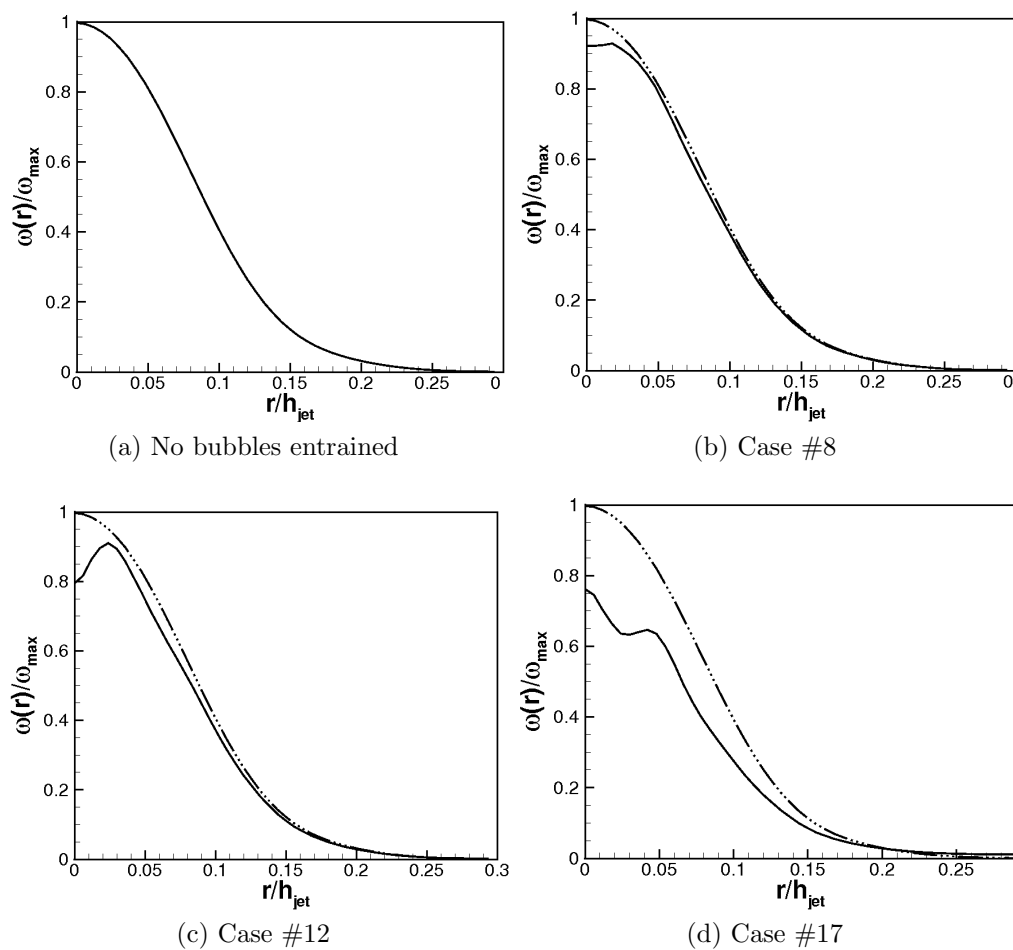


Figure 6.11: Vortex distortion by the presence of bubbles shown by radial vorticity distributions. (a) A vortex with no bubbles entrained, (b) an undistorted vortex, (c) a marginally distorted vortex, and (d) a significantly distorted vortex. (—) Volumetric coupling result, (---) 2-way coupling result (\cdots) 1-way coupling result. Instantaneous vorticity is normalized by maximum core vorticity, ω_{max}

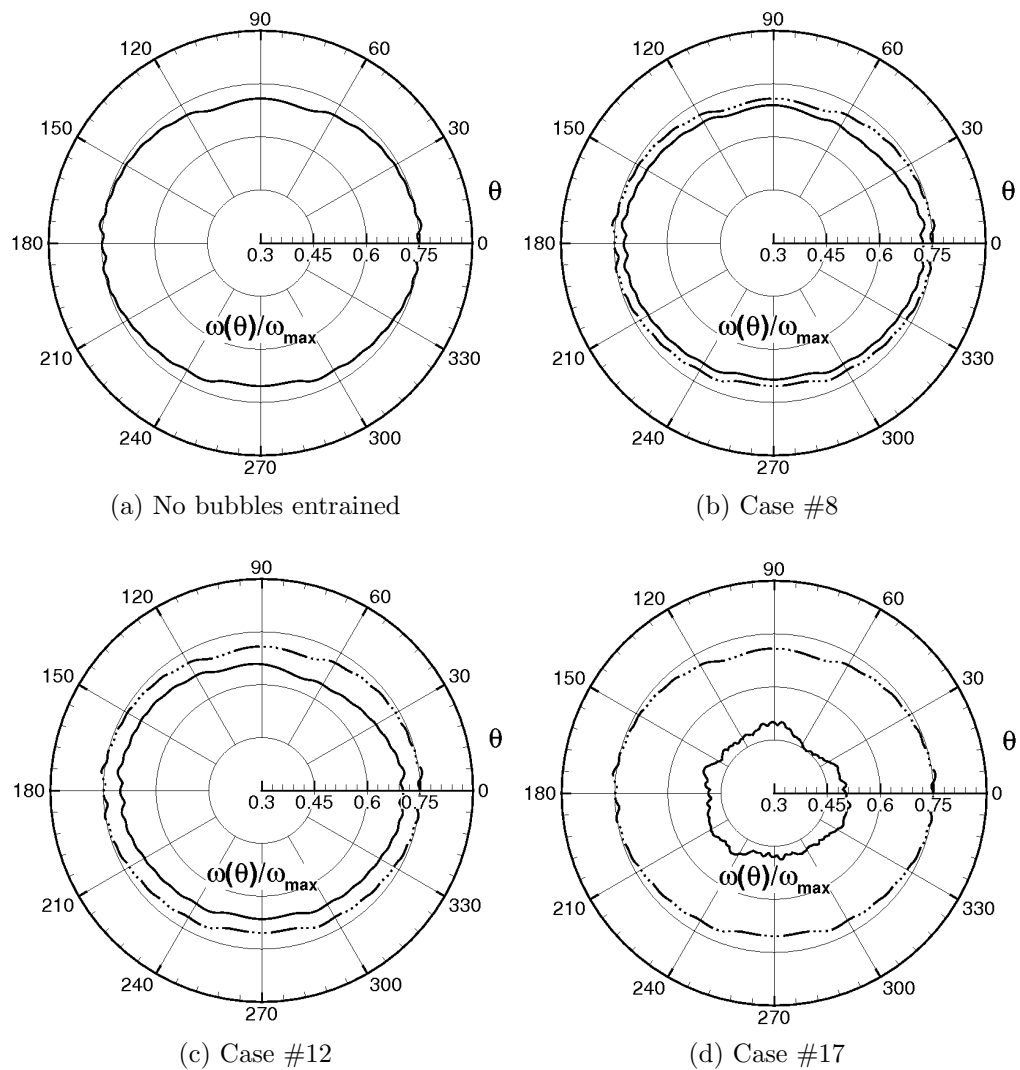


Figure 6.12: Vortex distortion by the presence of bubbles shown by angular vorticity distributions. (a) A vortex with no bubbles entrained, (b) an undistorted vortex, (c) a marginally distorted vortex, and (d) a significantly distorted vortex. (—) Volumetric coupling result, (---) 2-way coupling result (···) 1-way coupling result. Instantaneous vorticity is normalized by maximum core vorticity, ω_{max}

6.2 Bubble Entrainment by a Gaussian Vortex

6.2.1 Problem Setup

Consider a two dimensional vortex with initial circulation Γ_0 and core radius r_c whose vorticity distribution is a Gaussian function of radius. There is no radial velocity component, and the the tangential velocity can be written as follows:

$$u_\theta(r) = \frac{\Gamma_0}{2\pi r} \left(1 - e^{-\eta_1(r/r_c)^2}\right) \quad (6.6)$$

The maximum tangential velocity occurs at $r = r_c$ and is given by

$$u_c = \eta_2 \frac{\Gamma_0}{2\pi r_c} \quad (6.7)$$

where η_1 and η_2 are constants. The domain size is approximately $7 r_c \times 7 r_c \times 0.4 r_c$. Between $r = r_c$ and $r = 1.75r_c$, a correction function is used to obtain a better match with the traveling vortex tube. This correction velocity is of the form $U_c = \sum_{n=0}^4 a_n \tilde{r}^n$, where $\tilde{r} = (r - r_c)$. The no-slip condition is imposed at boundaries in the X and Y directions, and the domain is periodic in the Z direction. All necessary parameters used for the setup of the initial velocity field are summarized in Table 6.4

The Vortex is generated on two different grids to facilitate the use of both the DEM and HLE approaches. The same domain size is used, but significantly finer grid spacing is used for the HLE approach. The DEM grid is uniform throughout

Table 6.4: Computational parameters used in the setup of the Gaussian vortex case

Parameter	Value
r_c	0.01145 m
η_1	1.27
η_2	0.715
Tangential Velocity	$U(r) = \text{Equation 6.6} - U_c = \sum_{n=0}^4 a_n \tilde{r}^n$
Correction Coefficients	$a_0 = -3.835e(-4), a_1 = 0.6221, a_2 = 41.367, a_3 = -1,317, a_4 = 10,741$

Table 6.5: Computational domain and grids used for the Gaussian vortex case

Parameter	Value
Domain Size	0.08 m x 0.08 m x 0.005 m
Grid Size (HLE)	312 x 312 x 60
Grid Size (DEM)	64 x 64 x 4

and uses a spacing of $\Delta = 1mm$. The HLE grid is uniform in the region of bubble motion, and is stretched slightly towards the domain boundaries in the X and Y directions. In the region of bubble motion, the spacing is $\Delta = 0.2mm$. These two grids are summarized in Table 6.5

A comparison of the core shape of the stationary Gaussian vortex and the traveling vortex tube is made in figure 6.13. The contours of vorticity in the core of the travelling vortex tube are stretched in the axis of vortex motion, while the Gaussian vortex is perfectly symmetric. Figure 6.14 compares the radial vorticity distribution of the two vortices. The differences are slight enough that comparisons may be made between the two cases.

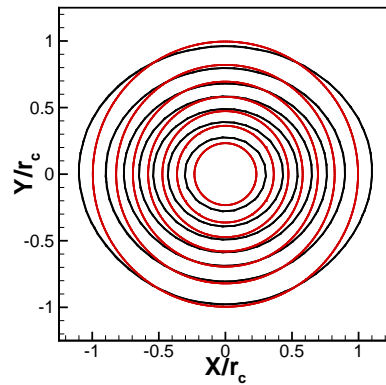


Figure 6.13: Comparison of the out of plane core vorticity in the traveling vortex tube (—) and the stationary Gaussian vortex (—). Contour lines are in steps of $\omega = 10s^{-1}$.

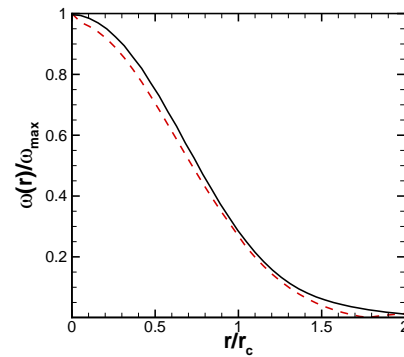


Figure 6.14: Comparison of radial distribution of vorticity in the traveling vortex tube (—) and the stationary Gaussian vortex (---)

6.2.2 Effects of DEM Lift Coefficient

The lift force on a rigid sphere in rotating flow has received much attention lately. Many expressions for the lift force have been suggested based on analytic work and empirical correlations from experimental data. One expression used frequently is the estimate of Auton [60] which equates the lift force to the cross product of the bubble relative velocity and the local vorticity:

$$F_{L(i)} = [(U - V) \times \omega]_i \quad (6.8)$$

This expression was derived for a sphere in an inviscid flow undergoing rigid body rotation. Neither the Gaussian vortex or the traveling vortex tube completely satisfy these assumptions due to viscous effects. In their vortex ring experiments, Sridhar & Katz [25] measured the lift force and suggested the following empirical correlation for a lift coefficient based on shear rate, $\alpha = \omega R_b / (U - V)$:

$$C_L = 0.59\alpha^{0.25} \quad (6.9)$$

$$F_{L(i)} = m_b \left(\frac{1}{2} \rho \pi R_b^2 (U - V)^2 C_L \right) [(U - V) \times \omega]_i \quad (6.10)$$

Figure 6.15 compares the entrainment trajectory of a single bubble released 1.8 core radii away from the vortex center using the two expressions for lift given in equation 6.8 and equation 6.10. The ultimate settling location differs only slightly, but the lift coefficient of equation 6.10 results in a slightly wider spiral, and a longer settling time. The S&K correlation has been adopted for the rest of the

DEM simulations in this section.

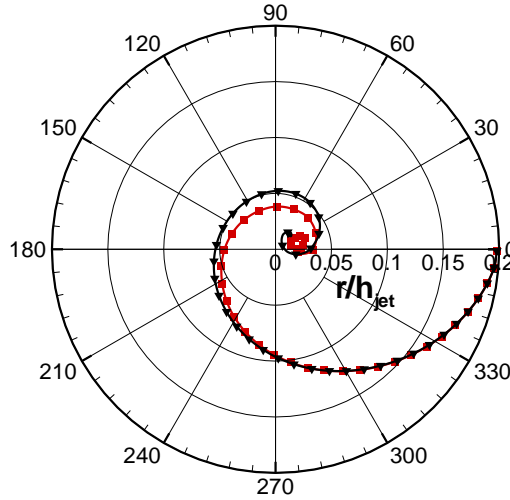


Figure 6.15: Effect of lift coefficient on entrainment trajectory. \blacktriangle S&K lift coefficient \blacksquare no lift coefficient

6.2.3 Comparison of DEM and HLE Trajectories

The entrainment of a bubble is simulated using both the HLE and DEM approaches. An air/water system is considered, with $\rho_f = 1,000 \text{ kg/m}^3$, $\rho_b = 1 \text{ kg/m}^3$, and $\mu_f = 0.001 \text{ Pa}\cdot\text{s}$. The bubble diameter is $1,200 \mu\text{m}$ for both cases. This results in a grid spacing of $\varnothing_b/\Delta = 0.96$ in the DEM simulations and $\varnothing_b/\Delta = 6$ in the HLE simulations. The gravitational acceleration, g , is varied so that different trajectories and settling locations are observed. The bubble is released from $\theta = 0$, $r/r_c = 1.8$, and spirals freely towards the core. The settling time is defined as the time after which there is no average bubble motion except for small periodic

Table 6.6: Comparison of DEM and HLE settling time and location in the Gaussian vortex

	Case #1	Case #2
\varnothing_b	$1,200\mu m$	$1,200\mu m$
g	$3m/s^2$	$5m/s^2$
r/r_c DEM	0.12	0.17
r/r_c HLE	0.43	0.60
r/h_{jet} DEM	0.014	0.019
r/h_{jet} HLE	0.050	0.068
t_s DEM	360 ms	390 ms
t_s HLE	420 ms	480 ms

oscillations around the settling location, r/r_c . Note that there certainly *is* bubble motion observed after the settling time, particularly in the HLE simulations, and it will be examined in the next section.

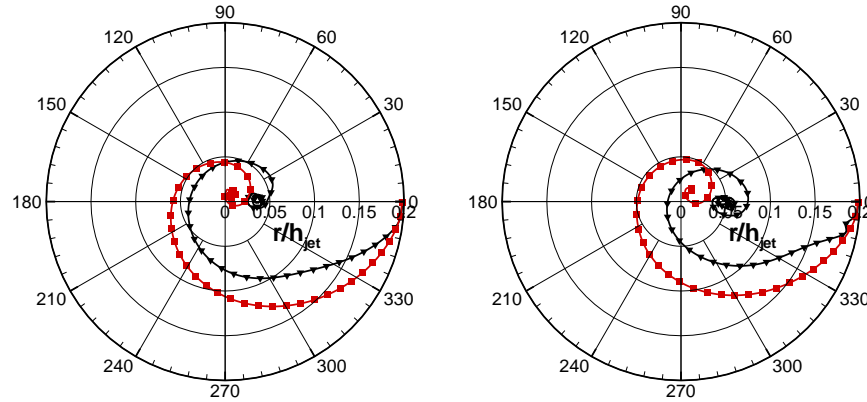
Figure 6.16 shows the trajectories of the bubbles from case 1 and 2. The trajectories of the bubbles predicted by the HLE and DEM approaches are similar, though the HLE bubble takes a more direct route to the vortex center in both cases. This was also observed by Oweis et al. [13] in their comparison of resolved bubbles and point particles. The results of the two cases are summarized in table 6.6. The final settling location, r/r_c , is greater for the HLE model in both cases, while the settling time is more consistent between the two models.

The present results for the settling radius of case #2 can be compared to the results from the traveling vortex tube case (Table 6.3). Surprisingly, the present HLE results agree better with the traveling vortex tube results. The single bubble entrained in the Gaussian vortex settles at a significantly lower radius than in

the vortex tube using the DEM approach. With the HLE approach, the values agree fairly well. There are a few factors which may contribute to this. First, the linear motion of the traveling vortex core has an obvious effect on the bubbles, because they settle at a different angular location than in the present, stationary case. In all of the traveling vortex tube cases, this was somewhere between 30 and 60 degrees from the horizontal plane. Here, the bubbles accumulate very near the horizontal plane, in the region of highest downward velocity. Additional studies would have to be conducted to determine if there is a corresponding settling radius change. Second, the DEM model used in the vortex tube cases considered a repulsive collision force acting on the bubbles, and its effects on the settling location are unknown at this point. Finally, the volumetric effects present for the single entrained bubble in this case are much less than for the 8 bubbles in the traveling vortex tube, which results in less distortion.

6.2.4 Vortex Distortion

Figure 6.17 shows the evolution of the vortex core as the bubble of case #2 is entrained. In the corresponding traveling vortex tube case (#13), with 8 bubbles entrained, only moderate core distortion was observed using the DEM approach. Even though the single bubble is quite large, the local volume fraction is still relatively low. As is expected, the one bubble modeled using the DEM approach causes very little distortion. Some slight core shape change is observed in the vicinity of the bubble, and at later times, higher vorticity has diffused radially



(a) Case # 1: $1,200\mu\text{m}$, $g = 3\text{m/s}^2$ (b) Case # 1: $1,200\mu\text{m}$, $g = 5\text{m/s}^2$

Figure 6.16: Comparison of DEM and HLE entrainment trajectories.
 ▲ HLE, ■ DEM

outward (h).

The flow interactions with the bubble modelled using the HLE approach are quite different. A three dimensional isometric view of the enstrophy isosurfaces at each stage is shown in figure 6.18. The bubble is released from rest in the downward velocity region on the right hand side of the vortex (a). Immediately, a wake is generated in the direction of bubble motion, as the bubble begins to move clockwise around the vortex center (b). The high buoyancy of the relatively large bubble retards the downward motion, and the initial velocity is small. Eventually, the bubble is entrained in fluid moving with high velocity towards the left, and the bubble switches direction (c). Due to this trajectory change, the wake is shed into into the outer region of the core. The bubble continues to accelerate in the clockwise direction, and a connected horseshoe vortex is formed (d). As the bubble

continues to the left, the fluid velocity aligns with the bubble buoyancy force, and the bubble accelerates upward *through* the fluid (e). In the process, the horseshoe vortex is shed into the outer core region, where it augments the local vorticity. The bubble begins to decelerate as it moves through the core, quite close to the vortex centerline (f), where it is immediately directed to the right by the velocity field (g). The surface forces begin to balance the buoyancy force, and the bubble approaches the original release angle, $\theta = 0$ (h). At this point, the wake is again shed due to the rapid deceleration. The bubble reaches its settling location, and the wake turns downward and follows the vortex curvature (i, not shown in 2D).

Once the bubble reaches its settling location, there is very little motion observed in the DEM results. Both models show a slow migration of the bubble radially outward, as the core strength is decreased, but this occurs in a steady fashion. Figure 6.19 shows the contours of vorticity 2.5 seconds after bubble release. At this time, the outer region of the core looks similar for both models, and there is actually more distortion observed in the DEM results for $r/r_c > 1$. In the HLE results, there is a band of very high vorticity at the settling radius, due to the wake of the bubble being advected along the vortex streamlines. This band is non-uniform and appears to be periodic in nature. Closer examination of the time evolution of the core shows that the bubble has an unsteady wake at its settling location. The Reynolds number for the settled bubble in this case is approximately 100, a value known to result in unsteady wakes for flow over a stationary sphere. Figure 6.20 shows the three dimensional isosurfaces of vorticity being shed from the settled bubble using the HLE approach. Over a single period of oscillation,

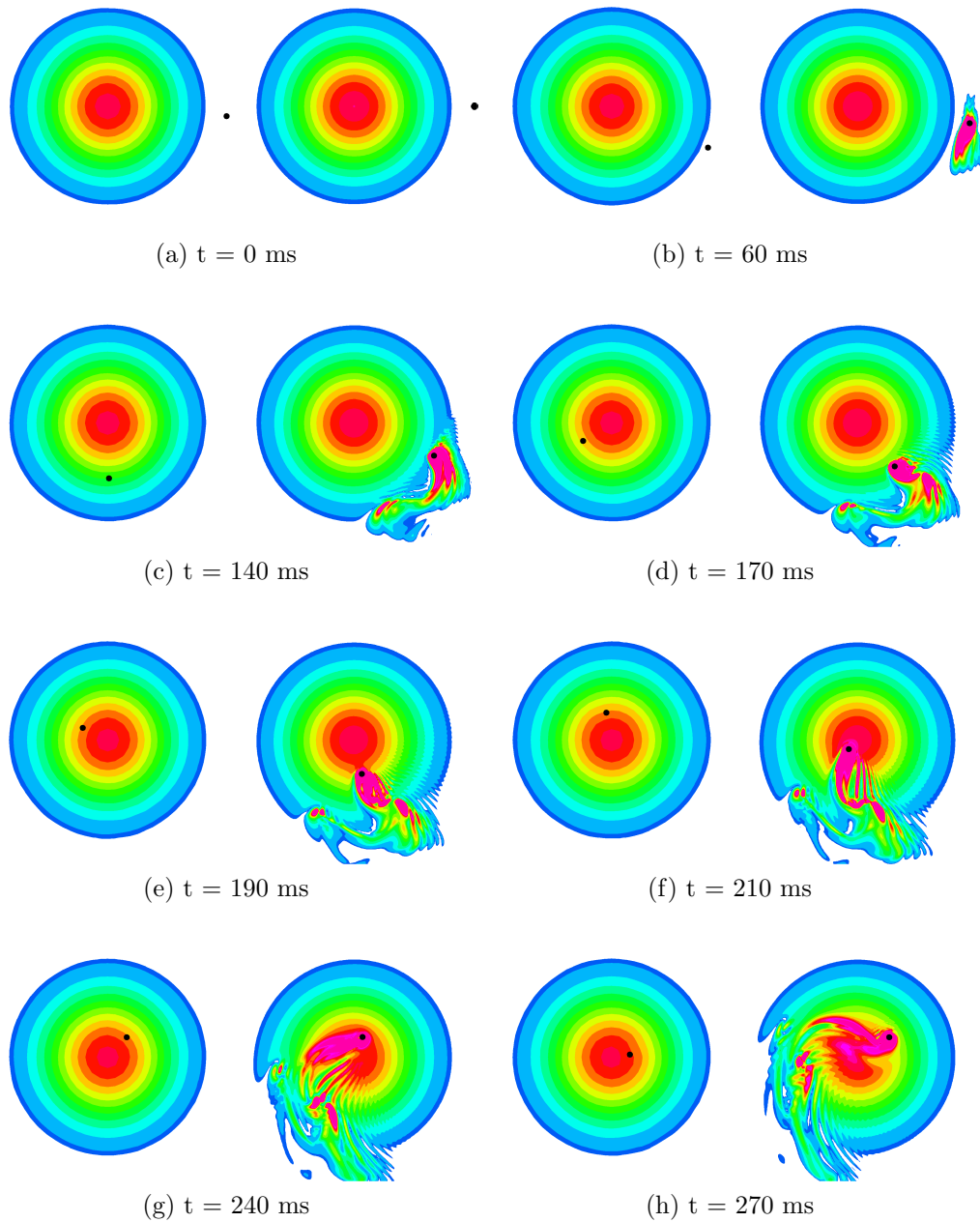


Figure 6.17: Entrainment of a single $1,200\mu m$ bubble (case #2). Left hand columns: DEM results, right hand columns: HLE results. Contours are of entropy, and range from 0(blue) to 100(magenta).

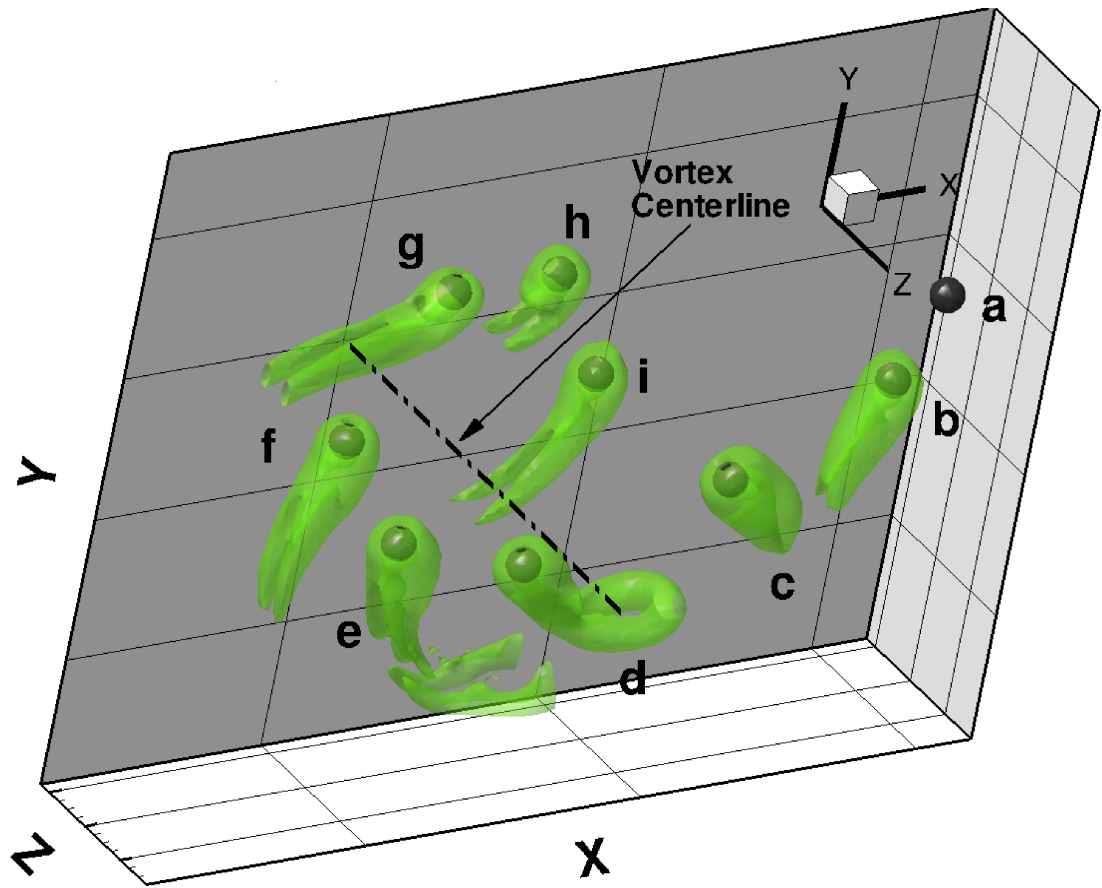


Figure 6.18: Isosurfaces of vorticity magnitude around a single 1200 micron bubble being entrained. Magnitude of isosurface is approximately twice the initial value of ω_{max}

the wake is elongated, and a detached structure forms (b&c). The structure pulls the already stretched tail of the wake (d), and the detached structure is advected downstream (e&f).

These results are qualitatively consistent with the observations of S&K. For bubbles with low settling radius, the Reynolds number is reduced, and the wake may become steady. At a large settling radius, the unsteadiness is advected into the outer region, and the net effect on the inner core is small. For some intermediate range, the Reynolds number is high enough for significant unsteadiness, and a periodic band of high vorticity significantly distorts the inner core region.

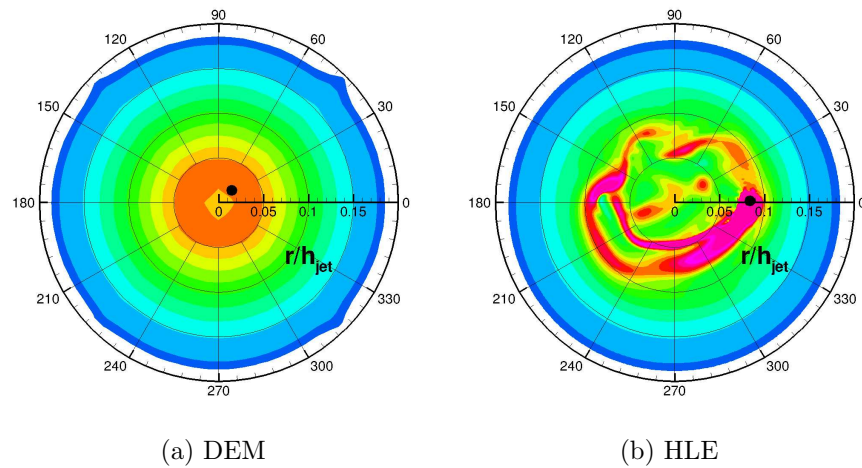


Figure 6.19: Vortex core after 2.5 seconds with a single $1, 200\mu\text{m}$ bubble at its final settling location. Contours of enstrophy range from 10 to 130

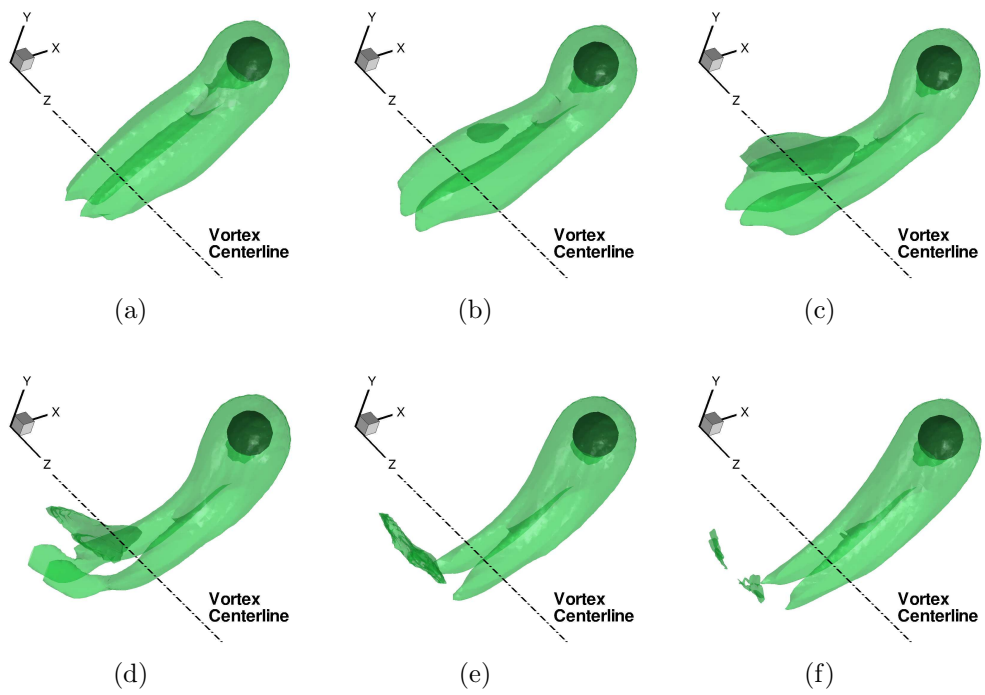


Figure 6.20: Periodic shedding of vorticity into the wake of the settled bubble

Chapter 7 – Conclusions and Outlook

A multiscale computational framework has been developed for simulation of bubble laden flow in hydro-propulsion systems. Two distinct modeling approaches have been developed and validated for simulation of both subgrid scale and fully resolved bubbles, and the accuracy of the HLE approach has been shown for simulation of resolved rigid body motion. Two detailed studies of bubble-vortex interactions have demonstrated the capabilities of both methods for simulation of complex, multiphase interaction problems. In these cases the two methods were used in tandem and along with experimental data, and offered excellent insight into the two phase bubble-vortex dynamics.

A complete simulation model for these types of problems could be a highly valuable tool for the design and operation of many types of systems. The HLE and DEM approaches, if integrated, would be capable of simulating large, dynamic systems with high accuracy at reasonable computational cost. Integration of the two models poses its own challenges, but the groundwork has been laid by validating the methods in a broad range of important subproblems.

There is some important future work outside of an integration effort possible for both the DEM and HLE methods. The lift and drag laws used in the DEM model could be tuned to work better in a broader range of bubbly flows, and show better agreement with experimental data. A three dimensional bubble-vortex interaction study could also prove valuable in understanding the present two dimensional results. In the HLE approach, a better understanding is needed of the grid convergence for freely moving particles at high density ratios ($\mathcal{O} 1,000$). As mentioned, a result of this type has not yet been reported in the literature.

Also, bubble deformation in the fully resolved, HLE regime needs to be accounted for if larger, cavitating bubbles are to be considered. Extension of the present methods to modelling of deformable interfaces is not trivial, but would certainly be a valuable research tool when combined with the rigid body HLE, and subgrid scale DEM models.

APPENDICES

Appendix A – Grids Used for Flow Over a Cylinder

The body fitted mesh used for the stationary cylinder case is shown in figure A.1. The C-type domain allows for a radially mapped region upstream of the cylinder. Downstream, an unstructured, paved meshing scheme is used. At the outlet, the grid transitions back to a uniform, cartesian region. Elements are clustered near the cylinder wall, where a resolution of 100 grid points per cylinder diameter is used. At a radius of 1.5 cylinder diameters away from the wall this resolution is decreased to 25 points per diameter. A high resolution is maintained in the wake region, while larger elements with local resolution as small as 2 points per cylinder diameter are used near the domain boundaries. A uniform inlet velocity is specified, and free-stream slip boundaries are used far from the cylinder wall.

The medium refinement cartesian grid used for the HLE simulations is shown in figure A.2. It is block structured with a uniform, refined patch around the cylinder and near wake. Uniform regions are used in all HLE simulations in regions of rigid body motion.

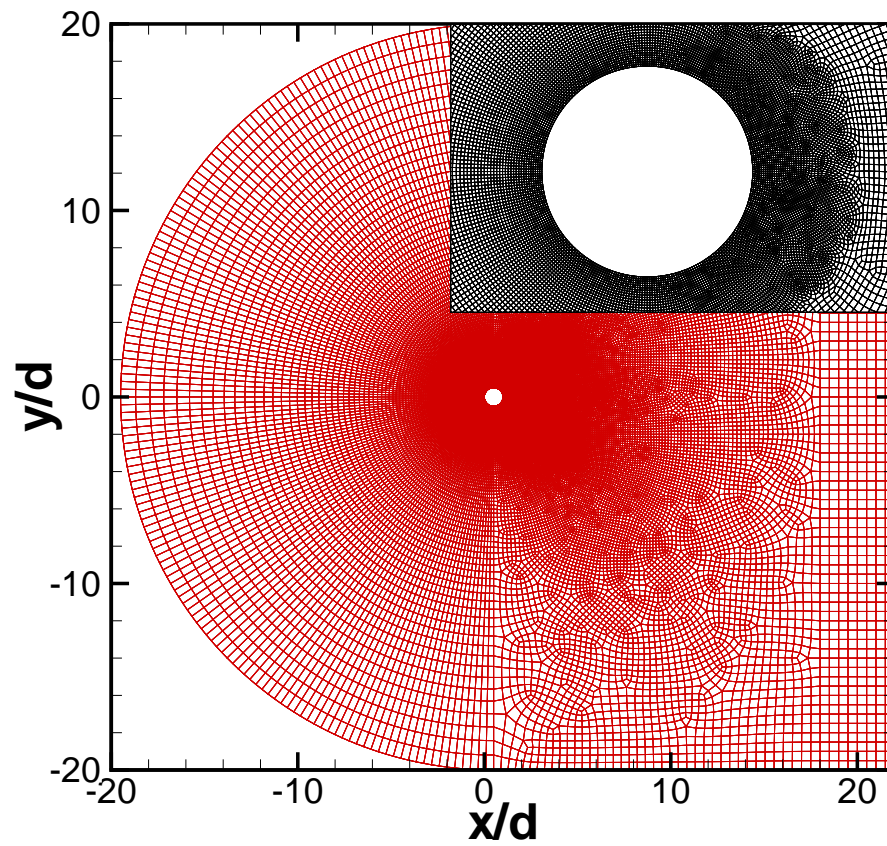


Figure A.1: Body fitted grid used for all simulations $Re_d = 40, 100, 300, 1,000$. The inset shows the region near the cylinder surface.

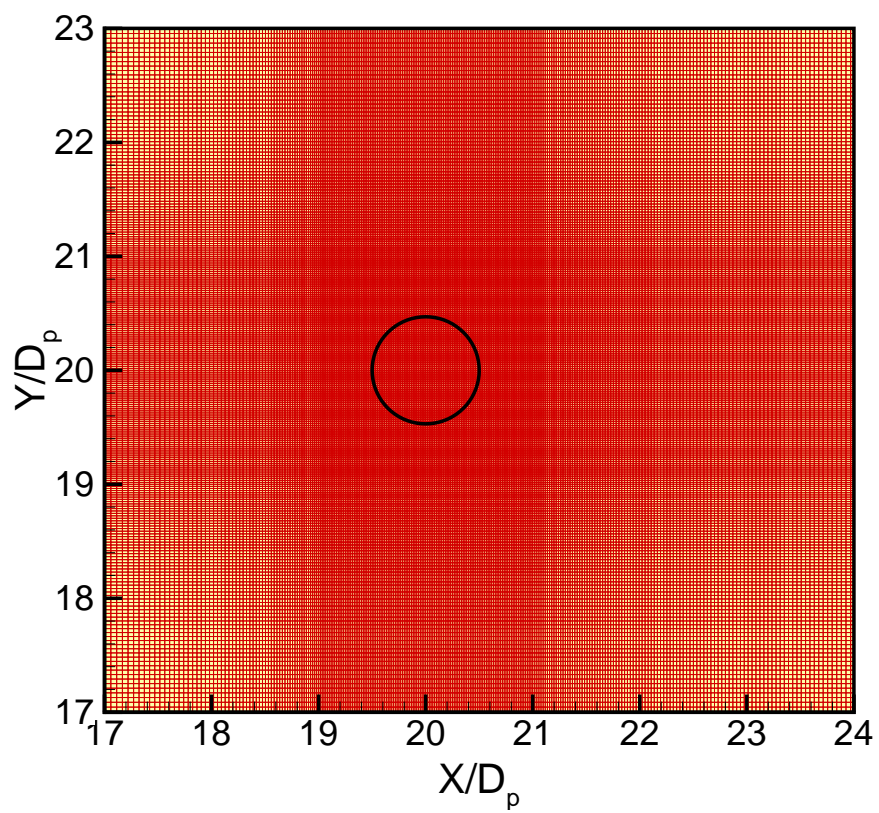


Figure A.2: Medium grid used in the HLE simulations. Close up of cylinder surface

Appendix B – DEM Numerical Algorithm

The goal is to advance the flow solution from t^n to t^{n+1} , and the dispersed phase solution from $t^{n+1/2}$ to $t^{n+3/2}$. Given proper specification of initial conditions, the solution proceeds as follows:

1. Set the predictor Velocities

The old time level solution for the fluid and particle velocities are projected using an explicit Euler advancement.

$$\mathbf{u}_p^{n+1/2} = \mathbf{u}_p^{n+3/2} \quad (\text{B.1})$$

$$\mathbf{u}_f^n = \mathbf{u}_f^{n+1} \quad (\text{B.2})$$

For increased accuracy, second order Adams-Bashforth predictors may also be used.

2. Project the dispersed phase solution to t^{n+1}

Use the old time level solution to project to the dispersed phase solution to t^{n+1} . The system of ODE's for dispersed phase motion (equation 3.7) is solved explicitly using several inner timesteps. During this sub-cycle, the particle motion is advanced as follows:

- Calculate the total force acting on the particle at t^n using equation 3.8

and the known pressure and velocity fields.

$$\sum \mathbf{F}_p^n = \mathbf{F}_G^n + \mathbf{F}_P^n + \mathbf{F}_D^n + \mathbf{F}_L^n + \mathbf{F}_{AM}^n + \mathbf{F}_{coll}^n \quad (\text{B.3})$$

- Advance the particle position & velocity

$$\mathbf{a}_p = \sum_{\text{forces}} / m_p \quad (\text{B.4})$$

$$\mathbf{u}_p = \mathbf{u}_p + \mathbf{a}_p \cdot \Delta t_p \quad (\text{B.5})$$

$$\mathbf{x}_p = \mathbf{x}_p + \mathbf{u}_p \Delta t_p \quad (\text{B.6})$$

where Δt_p is the dispersed phase inner timestep.

3. Compute projected values for Θ_p^{n+1} , and \mathbf{f}_{DEM}^{n+1}

With an approximation for discrete phase position and velocity at $t^{n+3/2}$, the volume fraction, Θ_p^{n+1} and momentum coupling force, \mathbf{f}_{DEM}^{n+1} are calculated using equations 3.4 and 3.24. The fluid density and volume fraction at t^{n+1} may be set:

$$\Theta_p^{n+1} = \frac{1}{2} (\Theta_p^{n+3/2} + \Theta_p^{n+1/2}) \quad (\text{B.7})$$

$$\rho^{n+1} = \rho_f \Theta_f^{n+1} \quad (\text{B.8})$$

4. Compute the dispersed position at $t^{n+3/2}$

The following steps (4-10) may be completed iteratively, in order to obtain better convergence between the fluid phase and dispersed phase solutions. In

this step, advance the particles from $t^{n+1/2}$ to $t^{n+3/2}$. Use the fluid velocity pressure and velocity at t^{n+1} , which is the average flow field over the particle integration time, $t^{n+1/2} \rightarrow t^{n+3/2}$, to determine particle forces. Solve for the new particle positions, $\mathbf{x}_p^{n+3/2}$ in the same manner as in step #2, and project the particle volume fraction and two way coupling force as in step #3.

5. **Advance the velocity to \mathbf{u}^* using a semi implicit first step of the fractional step algorithm**

The first step of the fractional step algorithm implicitly advances the fluid velocity to t^{n+1} . An explicit representation of the interphase force, \mathbf{f}_{DEM} , is used at t^{n+1} . This velocity field may not satisfy continuity, and is denoted \mathbf{u}^* .

$$\begin{aligned} \frac{\rho^{n+1}u_i^* - \rho^n u_i^n}{\Delta t} + \frac{1}{V_{cv}} \sum_{faces\ of\ cv} [u_{i,f}^n + u_{i,f}^*] g_N^{n+1/2} = \\ \frac{1}{V_{cv}} \sum_{faces\ of\ cv} \mu_f \left(\frac{\partial u_{i,f}^*}{\partial x_j} + \frac{\partial u_{i,f}^n}{\partial x_j} \right) + \mathbf{f}_{DEM}^{n+1} \end{aligned} \quad (\text{B.9})$$

where, subscript f denotes a face based value, and $g_N = \rho u_{f,N}$ denotes the face based *normal* momentum flux. The face based velocities are obtained by taking the arithmetic mean of the two control volumes belonging to the face of interest. The derivatives in the viscous terms are discretized using a Crank-Nicholson scheme.

6. **Remove the old pressure gradient from $\mathbf{u}_i^* \rightarrow \mathbf{u}_i^{**}$**

$$\frac{(\rho_f \mathbf{u}_i^{**}) - (\rho_f \mathbf{u}_i^*)}{\Delta t} = \frac{\partial p^n}{\partial x_i} \quad (\text{B.10})$$

7. **Solve the pressure Poisson equation for p^{n+1}**

A Poisson equation for pressure is obtained by taking the divergence of the face normal velocity component.

$$\frac{1}{V_{cv}} \sum_{\text{faces of } cv} \frac{\partial p^{n+1}}{\partial x_N} A_f \Delta t = \frac{1}{V_{cv}} \sum_{\text{faces of } cv} \rho_f^{n+1} u_{i,f}^{**} A_f + \frac{\partial \rho_f}{\partial t} \quad (\text{B.11})$$

The time derivative of fluid density is gotten from the continuity equation:

$$\frac{\partial \rho}{\partial t} = - \frac{1}{V_{cv}} \sum_{\text{faces of } cv} \rho_f^{n+1} u_{i,f}^{n+1} A_f \quad (\text{B.12})$$

This equation is solved iteratively, and multigrid techniques based on the *hypr* library [61] are used to speed convergence.

8. **Update the velocity field at the cv faces to the new continuity-satisfying field**

The new velocity field which satisfies continuity at t^{n+1} is gotten from:

$$\rho_f^{n+1} u_i^{n+1} = \Delta t \frac{\partial p^{n+1}}{\partial x_i} + g_N^n \quad (\text{B.13})$$

9. **Reconstruct the pressure gradient**

The pressure gradient is reconstructed at the cv centers from the face normal

gradients by the following summation over the faces:

$$\frac{\partial p}{\partial x_i} \Big|_{cv} = \frac{\sum_{\text{faces of } cv} \frac{\partial p}{\partial N} \cdot i |N_{i,f} A_f|}{\sum_{\text{faces of } cv} |N_{i,f} A_f|} \quad (\text{B.14})$$

10. Update the particle position

Remove any particles that left the domain during the timestep. Rearrange the particle partitions for efficient computations, and memory usage.

Appendix C – HLE Numerical Algorithm

The semi-discretization of the governing equations in each time-step is given below.

1. Advance the immersed objects

Starting with a solution at t^n and $t^{n-1/2}$, the centroids of material volumes ($X_{i,M}$) representing immersed objects are first advanced explicitly.

$$X_{i,M}^{n+1/2} = X_{i,P}^{n-1/2} + \mathcal{R}_{ij} \left(X_{j,M}^{n-1/2} - X_{j,P}^{n-1/2} \right) + U_{i,M}^n \Delta t, \quad (\text{C.1})$$

where $X_{i,M}$ is the position vector of the material volume center, $X_{i,P}$ is the position vector of the immersed object centroid, $U_{i,M}$ is the translation velocity, $\Omega_{i,M}$ is the angular velocity, and Δt is the time-step. Here \mathcal{R}_{ij} is the rotation matrix evaluated using particle locations at $t^{n-1/2}$. The details of the particle update and the rotation matrix are given in Appendix E.

2. Evaluate fluid properties in the entire domain

Knowing the new positions of the material volumes and particle centroid, an indicator function (color function) $\Theta^{n+1/2}$ is evaluated at the *cv*-center of the fixed background grid. We use a discrete delta-function [62] to compute the color function. The color function is unity inside the particle region and vanishes outside with smooth variation near the boundary. This thus allows identification of the particle on the background mesh. Details of the

interpolation between the material volume centers and the cv center are given in Appendix D. The density and the viscosity are then calculated over the entire domain as:

$$\rho_{cv}^{n+1/2} = \rho_P \Theta_{cv}^{n+1/2} + \rho_F (1 - \Theta_{cv}^{n+1/2}) \quad (\text{C.2})$$

$$\mu_{cv}^{n+1/2} = \mu_P \Theta_{cv}^{n+1/2} + \mu_F (1 - \Theta_{cv}^{n+1/2}) \quad (\text{C.3})$$

where ρ_P is the density of the immersed particle and ρ_F is the density of the surrounding fluid. Likewise μ_P is dynamic viscosity of the fictitious fluid inside the particle region, and μ_F is the dynamic viscosity of the surrounding fluid. For particles with specified motion (microvalves) μ_P is assumed equal to the fluid viscosity (μ_F). For bubbles, appropriate viscosity of the air bubble is specified.

3. Advance the momentum equations using the fractional step algorithm

Using the fractional step method [63], first obtain a predicted velocity field over the entire domain. We advance the velocity field from t^n to t^{n+1} . The predicted velocity fields may not satisfy the continuity or the rigidity constraints. These are enforced later.

$$\frac{u_{i,cv}^* - u_{i,cv}^n}{\Delta t} + \frac{1}{V_{cv}} \sum_{\text{faces of } cv} u_{i,\text{face}}^{*n+1/2} u_N^n A_{\text{face}} = \frac{1}{\rho_{cv}^{n+1/2}} \left(\frac{1}{V_{cv}} \sum_{\text{faces of } cv} \tau_{ij,\text{face}}^{*n+1/2} N_{j,\text{face}} A_{\text{face}} \right) + g_i \quad (\text{C.4})$$

where g_i is the gravitational acceleration, V_{cv} is the volume of the cv , A_{face} is the area of the face of a control volume, $N_{j,\text{face}}$ is the face-normal vector and

$$\begin{aligned} u_{i,\text{face}}^{*n+1/2} &= \frac{1}{2} (u_{i,\text{face}}^n + u_{i,\text{face}}^*); \\ \tau_{ij,\text{face}}^{*n+1/2} &= \mu_{cv}^{n+1/2} \left[\frac{1}{2} \left(\frac{\partial u_i^n}{\partial x_j} + \frac{\partial u_i^*}{\partial x_j} \right) + \left(\frac{\partial u_j^n}{\partial x_i} \right) \right]_{\text{face}} \end{aligned}$$

In the above expressions, the velocities at the ‘face’ are obtained by using arithmetic averages of the neighboring cvs attached to the face. For the viscous terms, the velocity gradients in the direction of the momentum component are handled implicitly using the Crank-Nicholson scheme. A centered discretization scheme is used for spatial gradients. Evaluation of the pressure gradients at the cv centers is explained below.

4. Solve the variable coefficient Poisson equation for pressure:

$$\frac{1}{\Delta t} \sum_{\text{faces of cv}} u_N^* A_{\text{face}} = \sum_{\text{faces of cv}} \frac{1}{\rho_{\text{face}}^{n+1/2}} A_{\text{face}} \frac{\delta p^{n+1/2}}{\delta N}, \quad (\text{C.5})$$

where ρ_{face} is obtained using arithmetic averages of density in the neighboring cvs . The face-normal velocity u_N^* and the face-normal pressure gradient are obtained as:

$$\begin{aligned} u_N^* &= \frac{1}{2} (u_{i,\text{nbr}}^* + u_{i,\text{cv}}^*) N_{i,\text{face}} \\ \frac{\delta p^{n+1/2}}{\delta N} &= \frac{p_{\text{nbr}}^{n+1/2} - p_{\text{cv}}^{n+1/2}}{|\mathbf{s}_{\text{cv,nbr}}|} \end{aligned}$$

where nbr represents neighboring cv associated with the $face$ of the cv , and $|\mathbf{s}_{cv,\text{nbr}}|$ is the distance between the two cvs . The variable-coefficient pressure equation is solved using a Bi-Conjugate gradient algorithm [64].

5. Reconstruct the pressure gradient at the cv centers

Use the density and face-area weighting first proposed by Ham & Young [65]

$$\frac{1}{\rho_{cv}^{n+1/2}} \frac{\delta p^{n+1/2}}{\delta x_i} = \frac{\sum_{\text{faces of } cv} \frac{1}{\rho_{\text{face}}^{n+1/2}} \frac{\delta p^{n+1/2}}{\delta N} \cdot \vec{i} |N_{i,\text{face}} A_{\text{face}}|}{\sum_{\text{faces of } cv} |N_{i,\text{face}} A_{\text{face}}|} \quad (\text{C.6})$$

6. Update the cv center and face-normal velocities to satisfy the incompressibility constraint

$$\widehat{u}_{i,cv} = u_{i,cv}^* - \Delta t \frac{\delta p_{cv}^{n+1/2}}{\delta x_i} \quad (\text{C.7})$$

$$\widehat{u}_N = u_N^* - \Delta t \frac{\delta p^{n+1/2}}{\delta N} \quad (\text{C.8})$$

The face-normal velocity field \widehat{u}_N will satisfy the incompressibility constraint, however, the cv -based velocity may not satisfy the rigid-body constraint inside the particle region. Note that in the absence of any rigid body, $\rho = \rho_F$ throughout the domain, and the algorithm reduces to the standard fractional step scheme for single-phase, incompressible flow. The above velocity field will then be denoted as $u_{i,cv}^{n+1}$. In the presence of rigid bodies, the following steps are performed to enforce the rigidity constraint within the particle

domain.

7. Solve for the translational and rotational fields

First interpolate the velocity field $\widehat{u}_{i,cv}$ from the grid cvs to the material volume centroids to obtain $\widehat{U}_{i,M}$ using the kernel interpolation outlined in the Appendix D. Solve for the translational and rotational velocity fields

$$\mathcal{M}_P \mathbf{U}_P^T = \sum_{M=1}^N V_M \rho_M \mathbf{U}_M \quad (\text{C.9})$$

$$\mathcal{I}_P \boldsymbol{\Omega}_P = \sum_{M=1}^N \rho_M V_M (\mathbf{r} \times \mathbf{U}_M), \quad (\text{C.10})$$

where subscripts P and M denote the particle and the material volume centroids respectively, V_M is the volume and ρ_M the density of each material volume, $\mathcal{M}_P = \sum_{M=1}^N \rho_M V_M$ is the total mass of the particle, \mathcal{I}_P is the moment of inertia of the particle about the coordinate axes fixed to the particle centroid, and \mathbf{r} is the position vector of a point within the particle region with respect to the particle centroid.. The moment of inertia is given as

$$\mathcal{I}_P = \sum_{M=1}^N \rho_M V_M [(\mathbf{r} \cdot \mathbf{r}) \mathbf{I} - \mathbf{r} \otimes \mathbf{r}], \quad (\text{C.11})$$

where \mathbf{I} represents the identity matrix. The rigid body motion is then obtained as:

$$\mathbf{U}_M^{RBM} = \mathbf{U}_M^T + \boldsymbol{\Omega}_P \times (\mathbf{X}_M - \mathbf{X}_P). \quad (\text{C.12})$$

8. **Compute the rigid-body constraint force and correct the velocity field to satisfy this constraint within the particle region.**

$$\mathbf{F}_{i,M}^{n+1} = -\frac{(U_{i,M} - U_{i,M}^{RBM,n+1})}{\Delta t}. \quad (\text{C.13})$$

The force on the grid control volumes ($f_{i,cv}$) is obtained from $\mathbf{F}_{i,M}$ by using the interpolation scheme discussed in Appendix D. The velocity field inside the particle region is then modified as:

$$u_{i,cv}^{n+1} = \widehat{u}_{i,cv} + \Delta t f_{i,cv}^{n+1}. \quad (\text{C.14})$$

Appendix D – Interphase Interpolations

Any property defined at the material volumes within the particle can be projected onto the background grid by using interpolation functions. Use of simple linear interpolations may give rise to unphysical values within the particle domain (e.g. volume fractions greater than unity) [66] and may give rise to numerical oscillations in the particle velocity. In order to overcome this, a smooth approximation of the quantity can be constructed from the material volumes using interpolation kernels typically used in particle methods [67]:

$$\Phi^\Delta(\mathbf{x}) = \int \Phi(\mathbf{y})\xi^\Delta(\mathbf{x} - \mathbf{y})d\mathbf{y} \quad (\text{D.1})$$

where Δ denotes grid resolution. The interpolation operator can be discretized using the material volume centroids as the quadrature points to give

$$\Phi^\Delta(\mathbf{x}) = \sum_{M=1}^N V_M \Phi(\mathbf{X}_M) \xi^\Delta(\mathbf{x} - \mathbf{X}_M) \quad (\text{D.2})$$

where \mathbf{X}_M and V_M denote the coordinates and volume of the material volumes respectively and the summation is over all material volumes for a particle. For example, in order to compute particle volume fraction, $\Phi(\mathbf{X}_M)$ will be unity at all material points. This gives unity volume fraction within the particle domain and zero outside the particle. In order to conserve the total volume of the particle as

well as the total force/torque exerted by the particle on the fluid, the interpolation kernel should at least satisfy

$$\sum_{M=1}^N V_M \xi^\Delta(\mathbf{x} - \mathbf{X}_M) = 1 \quad (\text{D.3})$$

$$\sum_{M=1}^N V_M (\mathbf{x} - \mathbf{X}_M) \xi^\Delta(\mathbf{x} - \mathbf{X}_M) = 0 \quad (\text{D.4})$$

Several kernels with second-order accuracy include Gaussian, quartic splines etc. A kernel with compact support requiring only the immediate neighbors of a control volume has been designed and used in immersed boundary methods [62]. For uniform meshes with resolution Δ it utilizes only three points in one dimension and gives the sharpest representation of the particle onto the background mesh:

$$\xi^\Delta(\mathbf{x} - \mathbf{X}_M) = \frac{1}{\Delta^3} \delta\left(\frac{x - X_M}{\Delta}\right) \delta\left(\frac{y - Y_M}{\Delta}\right) \delta\left(\frac{z - Z_M}{\Delta}\right), \quad (\text{D.5})$$

where

$$\delta(r) = \begin{cases} \frac{1}{6}(5 - 3|r| - \sqrt{-3(1 - |r|)^2 + 1}), & 0.5 \leq |r| \leq 1.5, r = \frac{(x-x_0)}{\Delta} \\ \frac{1}{3}(1 + \sqrt{-3r^2 + 1}), & |r| \leq 0.5 \\ 0, & \text{otherwise.} \end{cases} \quad (\text{D.6})$$

The same interpolation kernel can be used to interpolate an Eulerian quantity defined at the grid centroids to the material volume centroids. The interpolation kernel is second order accurate for smoothly varying fields [68]. The effect of these interpolations is that the surface of the particle is smoothed over the scale

proportional to the kernel length. Note that in order to reduce the spreading of the interfacial region, it is necessary to use compact support as well as finer background grids and material volumes.

Appendix E – Updating the Particle Position

The rigid body motion (RBM) of a particle can be decomposed into translational (\mathbf{U}^T) and rotational (\mathbf{U}^R) components. The total velocity field at each point within the particle is given as

$$\mathbf{U}^{RBM} = \mathbf{U}^T + \boldsymbol{\Omega} \times \mathbf{r} \quad (\text{E.1})$$

where \mathbf{U}^T is the translational velocity, $\boldsymbol{\Omega}$ the angular velocity, and \mathbf{r} the position vector of the material volume centroid with respect to the particle centroid. All the material volumes have the same translational velocity as the particle centroid ($\mathbf{U}^T = \mathbf{U}_P$).

Given a velocity field and the positions (\mathbf{X}_M^0) of the material volume centroids and the particle centroid (\mathbf{X}_P) at $t = t_0$, the new positions (\mathbf{X}_M^t) at $t = t_0 + \Delta t$ are obtained by linear superposition of the rotational and translational components of the velocity. The axis of rotation passing through the rigid body centroid \mathbf{X}_P is given as $\hat{\sigma} = \boldsymbol{\Omega}/|\boldsymbol{\Omega}|$. The new coordinates due to rotation around $\hat{\sigma}$ are given as

$$\mathbf{X}' = \mathcal{R}(\mathbf{X}_M^0 - \mathbf{X}_P) + \mathbf{X}_P \quad (\text{E.2})$$

where the rotation matrix is

$$\mathcal{R} = \begin{bmatrix} t\hat{\sigma}_x\hat{\sigma}_x + c & t\hat{\sigma}_x\hat{\sigma}_y - s\hat{\sigma}_z & t\hat{\sigma}_x\hat{\sigma}_z + s\hat{\sigma}_y \\ t\hat{\sigma}_x\hat{\sigma}_y + s\hat{\sigma}_z & t\hat{\sigma}_y\hat{\sigma}_y + c & t\hat{\sigma}_y\hat{\sigma}_z - s\hat{\sigma}_x \\ t\hat{\sigma}_x\hat{\sigma}_z - s\hat{\sigma}_y & t\hat{\sigma}_y\hat{\sigma}_z + s\hat{\sigma}_x & t\hat{\sigma}_z\hat{\sigma}_z + c \end{bmatrix}. \quad (\text{E.3})$$

Here $c = \cos(\alpha)$, $s = \sin(\alpha)$, $t = 1 - \cos(\alpha)$, and $\alpha = |\boldsymbol{\Omega}|dt$. The material volume centroids are all uniformly translated to give the final positions,

$$\mathbf{X}_M^t = \mathbf{X}' + \mathbf{U}^T dt. \quad (\text{E.4})$$

Bibliography

- [1] Mitts, C., Talley, D., and Poulikakos, D., 1996, “A fundamental study of supercritical droplet deformation and breakup through a miscible fluid analog,” *AIAA, ASME, SAE, and ASEE, Joint Propulsion Conference and Exhibit, 32nd, Lake Buena Vista, FL*.
- [2] Apte, S., Mahesh, K., and Lundgren, T., 2007, “Accounting for finite-size effects in simulations of disperse particle-laden flows,” *International Journal of Multiphase Flow*.
- [3] Prosperetti, A. and Zhang, D., 1995, “Finite-particle-size effects in disperse two-phase flows,” *Theoretical and Computational Fluid Dynamics*, **7**(6), pp. 429–440.
- [4] FERRANTE, A. and ELGHOBASHI, S., 2007, “On the effects of microbubbles on Taylor–Green vortex flow,” *Journal of Fluid Mechanics*, **572**, pp. 145–177.
- [5] Joseph, D., Lundgren, T., Jackson, R., and Saville, D., 1990, “Ensemble averaged and mixture theory equations for incompressible fluid-particle suspensions,” *Int. J. Multiphase Flow*, **16**(1), pp. 35–42.
- [6] Mittal, R. and Iaccarino, G., “IMMERSED BOUNDARY METHODS,” .
- [7] Glowinski, R., Pan, T., Hesla, T., Joseph, D., and Periaux, J., 2001, “A fictitious domain approach to the direct numerical simulation of incompressible viscous flow past moving rigid bodies: application to particulate flow,” *Journal of Computational Physics*, **169**(2), pp. 363–426.
- [8] Apte, S., Martin, M., and Patankar, N., 2009, “A numerical method for fully resolved simulation (FRS) of rigid particle–flow interactions in complex flows,” *Journal of Computational Physics*, **228**(8), pp. 2712–2738.
- [9] Tryggvason, G., Bunner, B., Esmaeeli, A., Juric, D., Al-Rawahi, N., Tauber, W., Han, J., Nas, S., and Jan, Y., 2001, “A front-tracking method for the computations of multiphase flow,” *Journal of Computational Physics*, **169**(2), pp. 708–759.

- [10] Hsiao, C. and Chahine, G., 2002, *Prediction of vortex cavitation inception using coupled spherical and non-spherical models and UnRANS computations.*
- [11] Darmana, D., Deen, N., and Kuipers, J., 2005, “Detailed modeling of hydrodynamics, mass transfer and chemical reactions in a bubble column using a discrete bubble model,” *Chemical Engineering Science*, **60**(12), pp. 3383–3404.
- [12] Sridhar, G. and Katz, J., 1999, “Effect of entrained bubbles on the structure of vortex rings,” *Journal of Fluid Mechanics*, **397**, pp. 171–202.
- [13] Oweis, G., van der Hout, I., Iyer, C., Tryggvason, G., and Ceccio, S., 2005, “Capture and inception of bubbles near line vortices,” *Physics of Fluids*, **17**, p. 022105.
- [14] van der Hoef, M., van Sint Annaland, M., Deen, N., and Kuipers, J., 2008, “Numerical Simulation of Dense Gas-Solid Fluidized Beds: A Multiscale Modeling Strategy,” *ANNUAL REVIEW OF FLUID MECHANICS*, **40**, p. 47.
- [15] Crowe, C., Troutt, T., and Chung, J., 1996, “Numerical Models for Two-Phase Turbulent Flows,” *Annual Reviews in Fluid Mechanics*, **28**(1), pp. 11–43.
- [16] Manninen, M., Taivassalo, V., and Kallio, S., 1996, *On the mixture model for multiphase flow*, Technical Research Centre of Finland.
- [17] Senocak, I. and Shyy, W., 2004, “Interfacial dynamics-based modelling of turbulent cavitating flows, Part-1: Model development and steady-state computations,” *International Journal for Numerical Methods in Fluids*, **44**, pp. 975–995.
- [18] Druzhinin, O. and Elghobashi, S., 1998, “Direct numerical simulations of bubble-laden turbulent flows using the two-fluid formulation,” *Physics of Fluids*, **10**, p. 685.
- [19] Ishimoto, J., Oike, M., and Kamijo, K., 2001, “Numerical analysis of two-phase pipe flow of liquid helium using multi-fluid model.” *Journal of Fluids Engineering*(Transactions of the ASME), **123**(4), pp. 811–818.
- [20] Hu, G. and Celik, I., 2008, “Eulerian–Lagrangian based large-eddy simulation of a partially aerated flat bubble column,” *Chemical Engineering Science*, **63**(1), pp. 253–271.

- [21] Maxey, M. and Riley, J., 1983, “Equation of motion for a small rigid sphere in a nonuniform flow,” *Physics of Fluids*, **26**, p. 883.
- [22] Mittal, R., Dong, H., Bozkurttas, M., Najjar, F., Vargas, A., and von Loebbecke, A., 2008, “A versatile sharp interface immersed boundary method for incompressible flows with complex boundaries,” *Journal of Computational Physics*, **227**(10), pp. 4825–4852.
- [23] Cristallo, A. and Verzicco, R., 2006, “Combined Immersed Boundary/Large-Eddy-Simulations of Incompressible Three Dimensional Complex Flows,” *Flow, Turbulence and Combustion*, **77**(1), pp. 3–26.
- [24] Van Nierop, E., Luther, S., Bluemink, J., Magnaudet, J., Prosperetti, A., and Lohse, D., 2007, “Drag and lift forces on bubbles in a rotating flow,” *Journal of Fluid Mechanics*, **571**, pp. 439–454.
- [25] Sridhar, G. and Katz, J., 1995, “Drag and lift forces on microscopic bubbles entrained by a vortex,” *Physics of Fluids*, **7**, p. 389.
- [26] Mazzitelli, I., Lohse, D., and Toschi, F., 2002, “The effect of microbubbles on developed turbulence,” *Physics of Fluids*, **15**, p. L5.
- [27] Climent, E., Simonnet, M., and Magnaudet, J., 2007, “Preferential accumulation of bubbles in Couette-Taylor flow patterns,” *Physics of Fluids*, **19**, p. 083301.
- [28] Ferrante, A. and Elghobashi, S., 2003, “On the physical mechanisms of two-way coupling in particle-laden isotropic turbulence,” *Physics of Fluids*, **15**, p. 315.
- [29] Apte, S., Mahesh, K., Moin, P., and Oefelein, J., 2003, “Large-eddy simulation of swirling particle-laden flows in a coaxial-jet combustor,” *International Journal of Multiphase Flow*, **29**(8), pp. 1311–1331.
- [30] Walther, J. and Koumoutsakos, P., 2001, “Three-dimensional vortex methods for particle-laden flows with two-way coupling,” *Journal of Computational Physics*, **167**(1), pp. 39–71.
- [31] Zhang, D. and Prosperetti, A., 1997, “Momentum and energy equations for disperse two-phase flows and their closure for dilute suspensions,” *International Journal of Multiphase Flow*, **23**(3), pp. 425–453.

- [32] Schiller, L. and Naumann, A., 1935, “A drag coefficient correlation,” *Vdi Zeitung*, **77**, pp. 318–320.
- [33] Darmana, D., Deen, N., and Kuipers, J., 2006, “Parallelization of an Euler–Lagrange model using mixed domain decomposition and a mirror domain technique: Application to dispersed gas–liquid two-phase flow,” *Journal of Computational Physics*, **220**(1), pp. 216–248.
- [34] Patankar, N. and Joseph, D., 2001, “Modeling and numerical simulation of particulate flows by the Eulerian–Lagrangian approach,” *International Journal of Multiphase Flow*, **27**(10), pp. 1659–1684.
- [35] Strack, P. and Cundall, P., 1979, “A discrete numerical model for granular assemblies,” *Geotechnique*, **29**, pp. 1–8.
- [36] Tsuji, Y., Kawaguchi, T., and Tanaka, T., 1993, “Discrete particle simulation of two-dimensional fluidized bed,” *Powder technology*, **77**(1), pp. 79–87.
- [37] Patankar, N., Singh, P., Joseph, D., Glowinski, R., and Pan, T., 2000, “A new formulation of the distributed Lagrange multiplier/fictitious domain method for particulate flows,” *International Journal of Multiphase Flow*, **26**(9), pp. 1509–1524.
- [38] Kim, D. and Choi, H., 2000, “A second-order time-accurate finite volume method for unsteady incompressible flow on hybrid unstructured grids,” *Journal of Computational Physics*, **162**(2), pp. 411–428.
- [39] Mahesh, K., Constantinescu, G., Apte, S., Iaccarino, G., Ham, F., and Moin, P., 2006, “Large-eddy simulation of reacting turbulent flows in complex geometries,” *Journal of Applied Mechanics*, **73**, p. 374.
- [40] Shu, C., Liu, N., and Chew, Y., 2007, “A novel immersed boundary velocity correction–lattice Boltzmann method and its application to simulate flow past a circular cylinder,” *Journal of Computational Physics*, **226**(2), pp. 1607–1622.
- [41] Henderson, R., 1995, “Details of the drag curve near the onset of vortex shedding,” *Physics of Fluids*, **7**, p. 2102.
- [42] Marella, S., Krishnan, S., Liu, H., and Udaykumar, H., 2005, “Sharp interface Cartesian grid method I: An easily implemented technique for 3D moving

- boundary computations,” *Journal of Computational Physics*, **210**(1), pp. 1–31.
- [43] Mittal, R. and Balachandar, S., 1995, “Effect of three-dimensionality on the lift and drag of nominally two-dimensional cylinders,” *Physics of Fluids*, **7**, p. 1841.
- [44] Kravchenko, A., Moin, P., and Shariff, K., 1999, “B-spline method and zonal grids for simulations of complex turbulent flows,” *Journal of Computational Physics*, **151**(2), pp. 757–789.
- [45] Mahesh, K., Constantinescu, G., and Moin, P., 2004, “A numerical method for large-eddy simulation in complex geometries,” *Journal of Computational Physics*, **197**(1), pp. 215–240.
- [46] Kunz, P. and Kroo, I., 2001, “Analysis and design of airfoils for use at ultra-low Reynolds numbers,” *Fixed and Flapping Wing Aerodynamics for Micro Air Vehicle Applications*, p. 35.
- [47] Dütsch, H., Durst, F., Becker, S., and Lienhart, H., 1998, “Low-Reynolds-number flow around an oscillating circular cylinder at low Keulegan–Carpenter numbers,” *Journal of Fluid Mechanics*, **360**, pp. 249–271.
- [48] Kim, D. and Choi, H., 2006, “Immersed boundary method for flow around an arbitrarily moving body,” *Journal of Computational Physics*, **212**(2), pp. 662–680.
- [49] Ten Cate, A., Nieuwstad, C., Derksen, J., and Van den Akker, H., 2002, “Particle imaging velocimetry experiments and lattice-Boltzmann simulations on a single sphere settling under gravity,” *Physics of Fluids*, **14**, p. 4012.
- [50] Feng, Z. and Michaelides, E., 2005, “Proteus: a direct forcing method in the simulations of particulate flows,” *Journal of Computational Physics*, **202**(1), pp. 20–51.
- [51] Mordant, N. and Pinton, J., 2000, “Velocity measurement of a settling sphere,” *The European Physical Journal B*, **18**(2), pp. 343–352.
- [52] Duineveld, P., 1995, “The rise velocity and shape of bubbles in pure water at high Reynolds number,” *Journal of Fluid Mechanics Digital Archive*, **292**, pp. 325–332.

- [53] Hua, J., Stene, J., and Lin, P., 2007, “Numerical simulation of 3D bubbles rising in viscous liquids using a front tracking method,” *Journal of Computational Physics*.
- [54] Frank, X., Funfschilling, D., Midoux, N., and Li, H., 2005, “Bubbles in a viscous liquid: lattice Boltzmann simulation and experimental validation,” *Journal of Fluid Mechanics*, **546**, pp. 113–122.
- [55] Clift, R., Grace, J., and Weber, M., 1978, *Bubbles, drops, and particles*, Academic Press San Diego, Calif.
- [56] Lundgren, T., 1972, “Slow flow through stationary random beds and suspensions of spheres,” *Journal of Fluid Mechanics*, **51**(02), pp. 273–299.
- [57] James, S. and Madnia, C., 1996, “Direct numerical simulation of a laminar vortex ring,” *Physics of Fluids*, **8**, p. 2400.
- [58] Glezer, A., 1988, “The formation of vortex rings,” *Physics of Fluids*, **31**, p. 3532.
- [59] Didden, N., 1979, “On the formation of vortex rings: Rolling-up and production of circulation,” *Zeitschrift für Angewandte Mathematik und Physik (ZAMP)*, **30**(1), pp. 101–116.
- [60] Auton, T., 2006, “The lift force on a spherical body in a rotational flow,” *Journal of Fluid Mechanics Digital Archive*, **183**, pp. 199–218.
- [61] Team, L. L. N. L. C., “Scalable linear solvers, hypre 2.0.0,” <https://computation.llnl.gov/casc/hypre/software.html>.
- [62] Roma, A., Peskin, C., and Berger, M., 1999, “An adaptive version of the immersed boundary method,” *Journal of Computational Physics*, **153**(2), pp. 509–534.
- [63] Ferziger, J. and Peric, M., *Computational Methods for Fluid Dynamics. 2002*, Springer.
- [64] Van der Vorst, H., 2003, *Iterative Krylov methods for large linear systems*, Cambridge University Press.
- [65] Ham, F., Young, Y., and CA, S. U., 2003, “A Cartesian adaptive level set method for two-phase flows,” .

- [66] Sharma, N. and Patankar, N., 2005, “A fast computation technique for the direct numerical simulation of rigid particulate flows,” *Journal of Computational Physics*, **205**(2), pp. 439–457.
- [67] Hieber, S. and Koumoutsakos, P., 2005, “A Lagrangian particle level set method,” *Journal of Computational Physics*, **210**(1), pp. 342–367.
- [68] Peskin, C., 2003, “The immersed boundary method,” *Acta Numerica*, **11**, pp. 479–517.

